Università
Ca'Foscari
Venezia

Corso di Dottorato di ricerca in
Scienza e Gestione dei Cambiamenti Climatici
ciclo XXXIII

Tesi di Ricerca

Impacts of the representation of orographic drag on the climate of an atmospheric model

SSD: FIS/06

Coordinatore del Dottorato
Prof. Enrica De Cian

Supervisori
Dr. Silvio Gualdi
Dr. Stefano Tibaldi

Dottorando
Guido Davoli
Matricola 956386

Impacts of the representation of orographic drag on the climate of an atmospheric model

Guido Davoli

Abstract

Many current state-of-the-art climate models show well-known and long-standing biases in representing the atmospheric circulation of Northern Hemisphere midlatitudes. In particular, models typically underestimate atmospheric blocking frequency, have problems in representing the observed properties of the storm tracks and simulate an excessively zonal atmospheric circulation, in particular over the European and North Atlantic sectors. Since their introduction in numerical models, it is known that orographic drag parameterizations play a key role in improving midlatitude circulation. However, they are still considered a potential source of errors, due to the uncertainties which affect some poorly constrained physical parameters.

In this work, I studied the effects of a new version of the parameterizations of both orographic form drag and gravity-wave drag in the NCAR Community Atmosphere Model. I designed a set of experiments to study their impacts, their interactions, and to test the model response to adjustments of two fundamentals, but unconstrained, parameters of the schemes. I have found that the two parameterizations improve the representation of blocking frequency, storm tracks structure, cold and heat waves over Europe, and their beneficial effects are modulated by the precise values of the parameters. These findings underline the importance of orographic parameterizations to improve climate models adequacy to represent reality, but also the need for a better characterization and for a unified representation of drag processes in future climate models.

Contents

Chapter 1

Introduction

In this chapter, some fundamental features of the atmospheric circulation at mid-latitudes are presented. A focus is placed on the atmosphere of the Northern Hemisphere (NH) during winter, and common problems in modeling this system are discussed. The representation of unresolved orography constitutes a source of errors in climate models, and there is increasing evidence of the importance of its role in the modeling of many relevant dynamical processes. Therefore, an overview of the historical and recent developement of unresolved orography parameterizations is given, and the motivations behind this work are presented.

1.1 Some general features of mid-latitude atmospheric circulation and variability

1.1.1 Jet Streams and storm tracks

Midlatitudes circulation is characterized by the presence of regions of westerly, high-speed winds called jet streams. The fundamental reason for the existence of westerly jet streams is the ultimate driver of the whole atmospheric circulation, that is the differential solar heating between equator and poles. However, we can distinguish between two different mechanisms giving rise to westerly jet streams. First, the buoyancy-driven Hadley circulation cause the poleward transport of westerly momentum, forming the so called subtropical jet at the northern flank of the Hadley cell. Secondly, mid-latitude transient eddies generated by baroclinic instability also transport momentum and heat polewards, forming the so called eddy-driven jet. While the subtropical jet is stronger near the tropopause, the eddy driven jet extends also at lower levels, inserting some barotropic character in the atmospheric flow (Vallis, 2017). These two mechanism continuously interact, and in many situations it is not possible to distinguish clearly between these two sources of westerly momentum. The only region of the Northern Hemisphere where a clear separation can occur is over the North Atlantic in winter. Here, the subtropical jet is usually located at the latitudes of North Africa, while the eddy-driven jet can be displaced northward, in particular during the positive phase of the North Atlantic Oscillation (NAO, Fig. 1.1), which is the dominant variability pattern in the extratropical atmosphere during winter (Hurrell et al., 2003).

The transient eddies giving rise to the eddy-driven jet identify with the mid-latitudes cyclones and anticyclones. Cyclones, steered by the mean flow, form and travel preferentially over certain regions called storm tracks. Storm tracks are located over the Pacific and Atlantic oceanic basins, where they guide cyclones northeastward toward the west coasts of North America and Europe, determining the local weather conditions (Wallace, Lim, and Blackmon, 1988). Jet streams and storm tracks constitute a coupled system, in which the mean flow steers eddies which, in turn, reinforce and concentrate the mean westerly flow itself (Chang, Lee, and Swanson, 2002).

The coupled nature of jet streams and storm tracks determines that their modeling in General Circulation Models (GCMs) can suffer from related problems. A long standing bias of

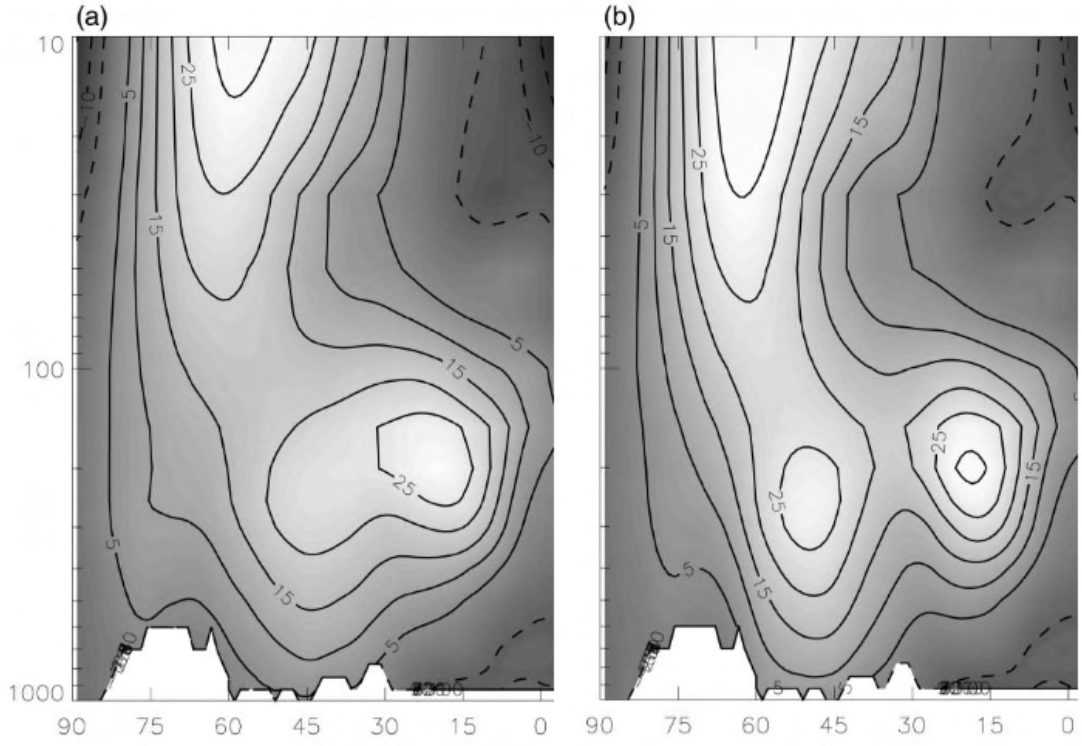

FIGURE 1.1: Climatological mean of the zonal mean zonal wind over the Atlantic sector [60W-0W] during negative (a) and positive (b) phases of the North Atlantic Oscillation. Image adapted from Ambaum, Hoskins, and Stephenson, 2001.

many climate models consists in the wrong latitudinal positioning of both jet streams and storm tracks, and in their modeled intensity. This is particularly true in the North Atlantic region.

On average, models participating to the 6th phase of the Coupled Model Intercomparison Project (CMIP6, Eyring et al., 2016) show lower-than-observed cyclogenesis rates over the whole NH; over the North Atlantic, the storm track and the jet stream are too zonal and equatorward, excessively penetrating over western Europe; over the North Pacific, the jet stream is displaced equatorward, while there is less consensus among models on the storm track position mean bias (Priestley et al., 2020, Harvey et al., 2020).

Even if reduced in amplitude, the biases observed in state-of-the-art climate models have the same character as in previous phases of CMIP projects (Delcambre et al., 2013, Ulbrich, Leckebusch, and Pinto, 2009, Zappa, Shaffrey, and Hodges, 2013, Eichler, Gaggini, and Pan, 2013, Colle et al., 2013).

A unique feature of the North Atlantic eddy-driven jet is the three-modality of the distribution of its latitudinal position in winter (Woollings, Hannachi, and Hoskins, 2010). This variability, which greatly influences European climate, is hardly reproduced by models. Both CMIP3 (Hannachi, Barnes, and Woollings, 2013), CMIP5 (Iqbal, Leung, and Hannachi, 2018) and CMIP6 (Oudar, Cattiaux, and Douville, 2020) models have problems in simulating the observed trimodality, preferring the central position and therefore producing narrow and excessively peaked modeled distributions. However, the complexity of the winter North Atlantic jet variability can not be fully captured by the jet latitude framework, which accounts for zonal-mean variation only and does not capture the effect of atmospheric blocking (Madonna et al., 2017).

1.1.2 Atmospheric blocking

The usual westerly flow at mid-latitudes can be altered by the presence of long-lasting, quasi-stationary anticyclonic anomalies called "blocks". These anomalous weather patterns usually develops at the exit regions of the jet streams, deviating the westerly flow and altering the path of migratory cyclones. Therefore, atmospheric blocking can cause prolonged weather anomalies over and near the regions where they develop, like heat waves in summer and cold spells in winter (Kautz, Martius, and Pfahl, 2021).

Forecasting blocking onset with Numerical Weather Prediction (NWP) models has been recognized as particularly challenging since the early 90's (Tibaldi and Molteni, 1990), but climate models still struggle in reproducing the observed climatological blocking frequency. Many generations of climate models have negative biases, in particular over the North Atlantic - European sector during winter, where blocking frequency underestimation can be as high as 50% (D'Andrea et al., 1998; Dunn-Sigouin and Son, 2013; Masato, Hoskins, and Woollings, 2013; Davini and D'Andrea, 2016; Davini and D'Andrea, 2020; Schiemann et al., 2020).

Negative biases in simulated winter Euro-Atlantic blocking frequency are associated with problems in reproducing the variability of the North Atlantic jet latitude and its trimodal distribution (Anstey et al., 2013; Davini and Cagnazzo, 2014) and in simulating the correct North Atlantic storm track tilt and intensity (Zappa et al., 2013).

The underestimation of blocking events frequency is connected with models' systematic errors over the same regions, in particular westerly wind and stationary waves pattern biases (Vial and Osborn, 2012). In fact, it has been shown that the models' mean bias is a crucial source of error in modeling climatological blocking frequency (Scaife et al., 2010).

The low frequency variability over the North Atlantic sector, associated with the eddy-driven jet stream latitudinal position and with the occurrence of blocking, can be also described in term of weather regimes (Franzke, Woollings, and Martius, 2011; Hannachi et al., 2017; Madonna et al., 2017). However, particularly at coarse resolution, models have problems in capturing the observed regimes and in reproducing their statistics (Dawson, Palmer, and Corti, 2012; Strommen et al., 2012).

1.1.3 Sudden Stratospheric Warmings

During winter, the reduced solar radiation reaching polar regions determines the formation of a strong meridional temperature gradient in the stratosphere. These conditions causes the onset of the polar night jet, a structure of strong westerly winds constituting the meridional edge of the stratospheric polar vortex. In the Northern Hemisphere, it forms at latitudes of around 60°N. Here, under favorable conditions, tropospheric planetary waves formed by land-sea contrast and topography can propagate into the stratosphere, altering the polar vortex and disrupting it in a period of days. These events are called Sudden Stratospheric Warmings (SSWs), since they are associated with temperature increases of tens of degrees over the pole (Butler et al., 2017). They are relatively rare (approximately 6 events per decade, Charlton and Polvani, 2007) but they can cause anomalous surface weather in the following weeks (Baldwin and Dunkerton, 2001; Mitchell et al., 2013 Kidston et al., 2015). Several studies have highlighted the two-way connection between blocking and polar stratospheric variability: blocks can influence the vertical propagation of tropospheric disturbances into the stratosphere, and blocking events frequency and duration can be altered by previous SSWs (Martius, Polvani, and Davies, 2009; Castanheira and Barriopedro, 2010; Nishii, Nakamura, and Orsolini, 2011; Woollings et al., 2010; Davini and Cagnazzo, 2014).

State-of-the-art climate models show a wide range of simulated SSWs frequency, with the majority of models underestimating it (Charlton et al., 2007; Wu and Reichler, 2020; Hall et al., 2021). In general, it is found that an underestimation of SSWs frequency is more common in

low-top (below approximately 1 hPa) models and in models with stronger-than-observed polar vortex (Cagnazzo and Manzini, 2009; Charlton-Perez et al., 2013).

1.1.4 Sources of uncertainty in modeling Northern Hemisphere mid-latitudes circulation

In the previous paragraphs, we described some of the main characteristics of the atmospheric circulation at mid-latitudes. The properties and the variability of jet streams and storm tracks, and the frequency and the location of atmospheric blocking and sudden stratospheric warmings events can have great impacts on the economies and the daily lives of people in some the most populated regions of our planet. Reproducing their properties is fundamental in order to have reliable global and regional climate change projections. However, as we mentioned, climate models show biases and errors. Comparing different model generations, a number of factors were identified as beneficial in order to achieve more realistic simulations. Increased atmospheric horizontal resolution (Jung et al., 2012, Schiemann et al., 2020, Priestley et al., 2020), improved physical parameterizations of convection (Jung et al., 2010) and orographic drag (Pithan et al., 2016), improving air-sea coupling (Woollings et al., 2009) and Gulf Stream position (O'Reilly, Minobe, and Kuwano-Yoshida, 2016), reduced North-Atlantic SSTs bias (Scaife et al., 2011) or higher resolution orography (Berckmans et al., 2013) are all elements contributing to the increased realism of the current climate modelss in reproducing mid-latitude atmospheric circulation. In particular, there is increasing evidence of the importance of the representation of unresolved orography in order to obtain a realistic mid-latitude circulation (Sandu et al., 2019). A recent intercomparison project proposed by the Working Group for Numerical Experimentation (WGNE) has shown that there is a large spread in how different modeling groups represent subgrid orographic stress through physical parameterizations (Sandu, Bechtold, and Beljaars, 2016), and it has been shown that, by using specific schemes, some of the long standing circulation biases discussed before can be reduced (Pithan et al., 2016). In this work, we will study how the introduction of two new physical parameterization schemes of unresolved ororgraphic drag influence the climate of the Community Atmosphere Model (CAM), the atmospheric component of the Community Earth System Model (CESM). A detailed outllok of the motivation and of the goals of the thesis is given in section 1.3; before that, an overview of the historical developement of orographic drag parameterizations and of the most relevant findings is given in the next section.

1.2 The role of orographic drag parameterizations in improving climate simulations

The first attempts to take into account the effects of unresolved orography in NWP models date back to the 80's. Wallace, Tibaldi, and Simmons, 1983 introduced an "envelope orography" in the ECMWF model, increasing the model resolved, grid scale orography by an amount proportional to the sub-grid variance of the unresolved orography in each grid cell. The introduction of this enhanced orography led to the reduction of the model systematic westerly wind and temperature biases and to a better simulation of planetary waves. It was also shown that it was the small-scales end of the unresolved topographic spectrum which was responsible of the increased simulated mountain torque and for the consequent reduction of westerly winds (Tibaldi, 1986). A similar strategy was used by Mesinger and Janjic, 1986 with the introduction of the so-called shilouette orography. In both cases, the enhanced resolved orography increases the occurrence the effects of blocked flow in mountaneous regions, anticipating the successive developement of low-level flow blocking parameterizations, but do not take into account the generation of gravity wave drag by unresolved orography. Moreover, the evenlope orography

can negatively interfere with near-surface data assimilation and give excessive precipitations (Lott and Miller, 1997).

The firsts physical parameterizations of orographic gravity wave drag were published by Boer et al., 1984, Palmer, Shutts, and Swinbank, 1986, and McFarlane, 1987, exploiting two-dimensional linear theory and the saturation hypothesis of Lindzen, 1981 to simulate wave dissipation and momentum deposition. The implementation of this first generation schemes in NWP models succesfully reduced the westerly wind and temperature biases, demonstrating the usefulness and the necessity of taking into account this phenomenon.

During the same years, theoretical and numerical studies on the dynamics of the low-level wave breaking associated with observed downslope windstorms were performed (Bacmeister and Pierrehumbert, 1988) and then their effects were included in models through parameterizations (Kim and Arakawa, 1995; Kim, 1996). Successive parameterizations also taken into account other low-level orographic effects such as upstream flow blocking, effectively providing a dynamical substitute of envelope orography, and orography anisotropy (Lott and Miller, 1997; Gregory, Shutts, and Mitchell, 1998; Scinocca and McFarlane, 2000) improving models sea level pressure, tropospheric circulation and generally improving models simulations and forecasts. Kim and Arakawa, 1995 and Kim, Eckermann, and Chun, 2003 provide reviews of different orographic gravity wave drag parameterization schemes.

Other than generating gravity waves, small-scale orography produces also a turbulent form drag on the atmospheric flow. The early works of Mason, 1985, Grant and Mason, 1990, Belcher, Newley, and Hunt, 1993, Wood and Mason, 1993 were fundamental in order to develop the firsts parameterization schemes of this phenomenon. A discussion on how to introduce these firts schemes in models can be found in Xu and Taylor, 1995, while the beneficial effects of the implementation of such a parameterization in the U.K. Met Office model for the first time are shown in Milton and Wilson, 1996. These schemes represented the unresolved turbulent drag using the concept of effective roughness length introduced by Fiedler and Panofsky, 1972. The improvement obtained introducing such schemes in models is not confined to the lower troposphere. As shown by Richter, Sassi, and Garcia, 2010, they can interact with resolved wind and gravity wave parameterizations modifying the vertical propagation of planetary waves, improving the frequency of SSWs. An alternative strategy to the effective roughness length concept was proposed by Beljaars, Brown, and Wood, 2004: instead of increasing surface momentum fluxes through an increased surface roughness, an explicit turbulent orographic drag profile depending on the properties of subgrid orography is directly inserted into the momentum equations. This scheme has been successfully implemented in the ECMWF operational model (Jung et al., 2010).

Therefore, the design and the implementation of parameterization schemes, in order to take into account different classes of unresolved physical processes related to the interaction between atmospheric flow and unresolved orography, constituted a fundamental advance to understand atmospheric dynamics and to build more and more accurate NWP and climate models. However, despite the recognized importance of unresolved orographic drag parameterizations in increasing models fidelity, it is also clear that the representation of these processes in current models suffers from fundamental uncertainties and weaknesses, which still make them an important source of errors and uncertainties.

One of the fundamental difficulties consist in the absence of extensive and continuos observations of these processes, which makes it difficult to constrain parameterizations. In addition, these schemes need to represent a broad class of phenomena, arising from multiple flow regimes, encompassing a large and continuos spectrum of spatial scales. However, it is common to introduce, in parameterizations, artificial scale separations, which do not exist in reality (see chapter 3 for a discussion on these points). Moreover, gravity wave drag parameterizations are usually based on the analytical solution of a simple two-dimensional linear flow over idealized mountains. All these facts determined the developement of a variety of

empirical approaches by different modeling groups, resulting in the presence of tuning parameters in the schemes. Their values are poorly constrained and their physical interpretation is not always straightforward, increasing the risk of introducing compensating errors in models. A recent model intercomparison project (Zadra, 2013) showed that there is a considerable spread between state-of-the-art models in terms of representation of unresolved orographic stress. Not only the total stress can be different, but also how it is partitioned between different schemes can be substantially different among models. Sandu, Bechtold, and Beljaars, 2016 demonstrated that by modifying the total amount and the distribution of stress in the ECMWF model by an amount similar to the difference found in comparison with the U.K. Met Office model, they could cause important changes in Northern Hemisphere sea level pressure, zonal wind and temperature, both in 10-days and in seasonal model integrations. Pithan et al., 2016 showed that switching off the parameterization of low-level flow blocking in a model with a good representation of storm tracks, jet streams and blocking statistics caused a deterioration of the simulation of the same processes, with a final bias similar to the mean error found in CMIP5 models, where this parameterization is usually absent. Also, Van Niekerk, Scinocca, and Shepherd, 2017 studied the effect of changing the values of a poorly constrained drag parameter in the flow-blocking scheme of the Canadian model. They found that NH stationary waves and westerlies can be greatly influenced, underlying how this kind of parameterization can help in alleviating long-lasting models biases. The amplitude of the stationary wave response to climate change was also shown to depend on the low-level drag. Moreover, Elvidge et al., 2019 found that there are also important differences in how different modeling groups represent and build the sub-grid orographic fields used to force parameterizations. This intermodel spread in orographic fields is of primary importance in determining intermodel spread in simulated surface stress, and therefore in determining systematic circulation biases. The procedure used for building these ancillary files and model mean orography also determines the balance between resolved and unresolved stress. Williams et al., 2020 reported how a change in resolved orography smoothing lead to a reduction of the U.K. Met Office model NH polar pressure bias. The sensitivity of the operational ECMWF model to the two-fold increase of the value of a poorly constrained constant of proportionality in the Beljaars, Brown, and Wood, 2004 scheme is reported in Jung et al., 2010, where an improvement in Euro-Atlantic blocking frequency is shown.

A possible strategy to overcome the unavailability of orographic drag observations is to perform very high resolution ($\approx$ few kilometers) simulations, in order to explicitly resolve a large portion of the orographic spectrum, and to use them as a benchmark for coarse resolution simulations. The results of this kind of experiments are reported by Van Niekerk, Sandu, and Vosper, 2018, Vosper et al., 2020, Van Niekerk et al., 2020. This strategy also provide a more direct way to constrain the drag of each orographic drag scheme, avoiding the iteration of model tuning excercises which can lead to the erroneous distribution of drag between different schemes. Using this method, Vosper et al., 2020 studied the "seamlessness" of a gravity wave parameterization, showing that a common hypothesis made in these schemes to calculate the upward flux of momentum caused the scheme to simulate a parameterized gravity wave momentum flux which is almost constant with varying model resolution.However, since decreasing models grid spacing results in more gravity waves being resolved, the parameterized gravity wave drag should reduce accordingly. A possible solution to develop more scale-aware gravity wave drag and flow blocking schemes is discussed by Van Niekerk and Vosper, 2021. Anyway, the findings of Kruse et al., 2022 demonstrate how mountain waves parameterizations are still necessary in state of the art NWP models run with a horizontal resolution of a few kilometers.

1.3 Motivation and structure of the thesis

The availability of reliable NWP and climate models is fundamental in order to achieve accurate predictions, usable to inform citizens, supporting decision makers and promoting policies of adaptation to climate change. The trustworthiness of models prediction, from day-to-day weather variability to decadal climate fluctuations and longer scenario timescales, depends critically on models ability in simulating the physical processes that give rise to the observed properties of the atmosphere and of the entire Earth system. Unfortunately, climate models still have difficulties in reproducing specific features of the Northern Hemisphere mid-latitudes atmospheric circulation, like the frequency of atmospheric blocking and sudden stratospheric warming events, the properties of the storm tracks and the variability of the eddy-driven jet. These phenomena, in addition to influencing the mean climate of highly populated regions of our planet, can trigger extreme events, potentially dangerous for human health and food production, causing high economic losses. Therefore, there is the need to study the causes of, and to identify potential solutions to, the errors affecting climate models.

One of the fundamental weaknesses of numerical climate models consist in their finite spatial and temporal resolution. Real physical processes taking place on scales smaller than model resolution can not be explicitly represented and must, therefore, be parameterized. Parameterizations are algorithms developed with the aim of representing the net effects of the unresolved scales on the resolved scales, as functions of the values of resolved variables and of numerical parameters to be determined by either fundamental physical constraints or by trial-and-error optimization procedures (the so-called "tuning"). Due to their intrinsic characteristics and to the chaotic nature of the atmospheric system, errors in parameterizations affecting directly the smallest resolved scales can propagate to the larger scales, deteriorating the adequacy of the modeling of the whole atmospheric general circulation. As discussed in the previous sections, in the last decades enormous progresses have been made in parameterizing the effects of unresolved orography on climate models general circulation. However, as it has become increasingly apparent in the last years, the great potential of state-of-the-art orographic drag parameterizations risks to be obscured by fundamental uncertainties on some of the underlying physics. There is, therefore, the need to better characterize orographic drag parameterizations and their uncertainties, to study how they behave in different models and how parameterizations of different orographic processes interact with each other.

In this work, I wanted to improve the simulation of the Northern Hemisphere mid-latitudes circulation in the NCAR Community Atmosphere Model (CAM, in its version 5.3), exploiting the availability of new orographic drag parameterizations. CAM5.3 uses the McFarlane, 1987 scheme to represent mountain gravity waves, without any explicit representation of low-level flow blocking and low-level gravity wave breaking. Moreover, the scheme does not take into account information on the orientation of the real unresolved orography. The task of representing the turbulent drag due to small scale mountains is left to the Turbulent Mountain Stress parameterization (Richter, Sassi, and Garcia, 2010), which uses an enhanced roughness length.

In the context of a model update to its version 6, many parameterizations were updated and many aspect of the model were changed. Among others, two new parameterizations of both gravity waves and turbulent orographic form drag were developed for CAM. During this thesis work, these new schemes were taken from CAM6 and adapted to CAM5.3. In this way, we obtained an "hybrid model" whose only difference with respect to CAM5.3 is the presence of two additional parameterizations of orographic drag. The new form drag parameterization is the Beljaars, Brown, and Wood, 2004 scheme, while the new gravity wave code, which takes into account also subgrid orography orientation, low-level flow blocking and gravity wave breaking is very similar to the one proposed by Scinocca and McFarlane, 2000. Details on these schemes are given in chapter 3, where an overview of the model is provided.

Firstly, we studied the impact on the model mid-latitudes circulation of using the new schemes in place of the old ones. To do so, the model is run in four different configurations, with the two gravity wave and the two form drag schemes switched alternatively on and off in order to test all the possible combinations of old and new schemes. This approach allowed us to study the effects of each single scheme and their mutual interaction. With "model" we mean the atmospheric model CAM, forced with observed SST and sea ice conditions (an AMIP-like experimentation), in order to avoid to introduce in our analysis additional sources of uncertainties like the climate drift of an oceanic model. With "new model" ("old model") we mean CAM5 used with both the new (old) orographic drag parameterizations.

Secondly, we analyzed the sensitivity of the new model to the values of two fundamental parameters of the new orographic schemes. As discussed in the previous sections, these two parameters are only weakly constrained by theoretical arguments and model tuning excercises, but they have the potential to greatly influence the simulated extratropical circulation. Therefore, we run different set of experiments in which the uncertain parameters are perturbed around their "standard" value, one at a time. These experiments allowed us to better understand the role of each single parameterization and their mutual interaction.

Finally, after the evaluation of the result obtained in the previous sections, some specific model configurations (that is, precise values for the new schemes' parameters) are chosen. More specifically, we considered particularly interesting the configurations in which both the two parameters are simultaneously decreased or increased. These two configurations and the new model run with standard parameters constitute a physically interesting ensemble of orographic drag settings, representing our uncertainty on the simulation of these processes. These ensemble members, together with the old model results, were compared with reanalysis data. In particular, we used the diagnostic tools presented in chapter 4 to quantify the impact of the new parameterizations on the representation of atmospheric blocking, storm tracks, jet stream and SSWs. Moreover, we implemented a simple framework to describe the connection between atmospheric blocking and extreme temperature events over Europe, and we checked how orographic parameters influence this link. All the experiments and the results are presented and discussed in chapter 5.

Chapter 2

The physics of orographic gravity wave and form drag

In this chapter, the fundamental physical properties of gravity waves are presented. Their generation, propagation and their effects on the atmospheric flow are discussed. Starting from the linearized atmospheric momentum equations and applying some reasonable approximations, the central equations and the basic features of the gravity wave drag, exploited for the design of models parameterizations, are derived. Nonlinear effects arising from different flow regimes are also mentioned. Moreover, the diverse effects of different orographic scales are discussed, and the turbulent form drag arising from the small-scale end of the topographic spectrum is presented. The key ideas for the parameterization of this phenomenon are reviewed, referring to the relevant literature.

2.1 Fundamental properties of gravity waves

When stably stratified air flows over mountains or topographic barriers, disturbances can develop and vertically travel in the atmosphere, sustained by the buoyancy force. These perturbations are called gravity waves. Following the reasoning of Gill, 1982, we illustrate here some of their fundamental properties. The calculations are based on the atmospheric governing equations (see Gill, 1982, section 4.10), but exploiting some simplifying assumptions to make the problem tractable but still physically realistic. First, we will assume that the density depends only on potential temperature and humidity, not on pressure:

$$\rho = \rho(\theta, q) \tag{2.1}$$

and that the motion is isentropic and without phase changes; therefore, for a material element

$$\frac{D\rho}{Dt} \equiv \frac{\partial \rho}{\partial \theta}\frac{D\theta}{Dt} + \frac{\partial \rho}{\partial q}\frac{Dq}{Dt} = 0. \tag{2.2}$$

This kind of fluids are called *incompressible*, since their density remains constant for isothermal pressure changes. This does not means that the density is constant everywhere in the fluid: the fluid can be stratified and density changes can happen during diabatic heating and cooling, but not if the fluid parcels moves from high pressure to low pressure or vice versa. From the above equation it follows that the continuity equation becomes

$$\rho^{-1}\frac{D\rho}{Dt} + \vec{\nabla}\cdot\vec{u} = 0 \Longrightarrow \vec{\nabla}\cdot\vec{u} = 0 \tag{2.3}$$

that is, the velocity field is *nondivergent*. This aproximation is good when particle velocities and perturbation phase speeds are small compared with the sound speed, and when the vertical

scale of motion is small compared with the atmospheric scale height $H_s \approx 8$ km, therefore a few hundreds meters in depth (Batchelor, 1967).

The mean state to be perturbed is assumed to be an equilibrium solution in hydrostatic equilibrium, of the form

$$p = p_0(z), \qquad \rho = \rho_0(z) \tag{2.4}$$

satisfying

$$\frac{dp_0}{dz} = -g\rho_0. \tag{2.5}$$

The perturbations from this mean state are defined as

$$p = p_0(z) + p', \qquad \rho = \rho_0(z) + \rho'. \tag{2.6}$$

Substituting these expressions in the atmospheric momentum equation (see Gill, 1982, section 4.10), and neglecting friction and rotation, one obtains the perturbation equations

$$\rho_0 \partial u/\partial t = -\partial p'/\partial x, \qquad \rho_0 \partial v/\partial t = -\partial p'/\partial y, \tag{2.7}$$

$$\rho_0 \partial w/\partial t = -\partial p'/\partial z - \rho' g \tag{2.8}$$

while linearizing 2.2 one has

$$\partial \rho'/\partial t + w d\rho_0/dz = 0 \tag{2.9}$$

and the nondivergence property 2.3 can be rewritten as

$$\partial u/\partial x + \partial v/\partial y + \partial w/\partial z = 0 \tag{2.10}$$

where u, v, w are the two horizontal and the vertical components of the velocity field $\vec{u}$. The term $-\rho' g$ in 2.8 represent the so called *buoyancy force*: an element with negative ρ' with respect to its surrounding environment is buoyant, experiencing an upward force, and vice versa. Equations 2.7-2.10 are the governing equations of our problem.

Eliminating u and v from 2.7, 2.10 we obtain the following relation between the horizontal divergence and the perturbation pressure:

$$\rho_0 \frac{\partial^2 w}{\partial z \partial t} = \left(\frac{\partial^2}{\partial x^2} + \frac{\partial^2}{\partial y^2} \right) p' \tag{2.11}$$

while eliminating ρ' from 2.8, 2.9 we get

$$\frac{\partial^2 w}{\partial t^2} + N^2 w = -\frac{1}{\rho_0} \frac{\partial^2 p'}{\partial z \partial t} \tag{2.12}$$

where $N(z)$ is a fundamental quantity, defined as

$$N^2 = -g \frac{1}{\rho_0} \frac{d\rho_0}{dz} \tag{2.13}$$

and known as the buoyancy or Brunt-Vaisala frequency, even if its importance was formerly noticed by Rayleigh in 1883. In presence of a purely vertical motion, that is without pressure gradient forces, the right hand side of 2.12 vanishes, and an air parcel will oscillate around its equilibrium position with frequency N, due to the restoring effect of the buoyancy force. When 2.11 and 2.12 are combined eliminating p', we obtain the following equation:

$$\frac{\partial^2}{\partial t^2} \left[\frac{\partial^2}{\partial x^2} + \frac{\partial^2}{\partial y^2} + \frac{1}{\rho_0} \frac{\partial}{\partial z} \left(\rho_0 \frac{\partial}{\partial z} \right) \right] w + N^2 \left(\frac{\partial^2}{\partial x^2} + \frac{\partial^2}{\partial y^2} \right) w = 0 \tag{2.14}$$

which can be solved analytically for special density profiles. However, we can make a final approximation, valid when the scale of the vertical variation of w is small compared to the scale of the vertical variation of ρ_0, that is the atmosphere scale height H_s:

$$\frac{1}{\rho_0}\frac{\partial}{\partial z}\left(\rho_0\frac{\partial}{\partial z}\right)w \approx \frac{\partial^2 w}{\partial z^2} \tag{2.15}$$

This approximation is called the *Boussinesq approximation*, and it is usually satisfied by atmospheric internal gravity waves. It leads to the final wave equation for the vertical velocity w:

$$\frac{\partial^2}{\partial t^2}\left[\frac{\partial^2}{\partial x^2}+\frac{\partial^2}{\partial y^2}+\frac{\partial^2}{\partial z^2}\right]w + N^2\left(\frac{\partial^2}{\partial x^2}+\frac{\partial^2}{\partial y^2}\right)w = 0. \tag{2.16}$$

Summarizing, starting from the atmospheric momentum and continuity governing equations, we obtained the equation describing the wave dynamics of small perturbations in a continuously stratified, hydrostatic, nondivergent and incompressible fluid, neglecting friction and Earth rotation effects. As will be made clear in the next paragraphs, this framework is appropriate to describe the real atmosphere on the spatial and temporal scales typical of internal gravity waves. Moreover, the analytical solutions we can find constitute an useful mathematical model capturing the basic, fundamental features of the observed waves, usable also for the developement of climate models parameterizations.

2.1.1 Constant N approximation

If the buoyancy frequency N is the same everywhere, traveling wave solutions of 2.16 have the form

$$w = w_0\cos(kx + ly + mz - \omega t) \tag{2.17}$$

where w_0 is the vertical velocity disturbance amplitude, $\vec{k} = (k, l, m)$ is the wavenumber vector and ω is the oscillation frequency; $\vec{k}$ and ω must satisfy the dispersion relation

$$\omega^2 = \frac{(k^2+l^2)N^2}{(k^2+l^2+m^2)}. \tag{2.18}$$

Since $m^2 \geqslant 0$, the vertical velocity wave oscillation frequency is always equal or smaller than the buoyancy frequency N. Buoyancy force can not support oscillations at frequencies larger than the Brunt-Vaisala frequency. Precisely, the exact magnitude of the oscillation frequency depends on the angle ϕ between the wave vector $\vec{k}$ and the vertical direction. In fact, expressing k, l, m in spherical coordinates, the dispersion relation becomes simply (Gill, 1982)

$$\omega = N\cos\phi. \tag{2.19}$$

Since, by definition, the wave vector $\vec{k}$ is perpendicular to wavefronts, that is surfaces of constant phase, the angle ϕ is the angle between the vertical and the direction of oscillation of the air parcel. The reduction in ω comes from the projection of gravity along the tilted trajectory, and so the apparent reduction in stratification (Durran, 1990).

From 2.7-2.10 and 2.18, we can derive the following relations for pressure, density and horizontal velocity perturbations associated with the wave 2.17:

$$p' = -\frac{\omega m\rho_0}{(k^2+l^2)^{-1}}w_0\cos(kx + ly + mz - \omega t) \tag{2.20}$$

$$\rho' = -\frac{N^2\rho_0}{\omega g} w_0 \sin(kx + ly + mz - \omega t) \tag{2.21}$$

$$\frac{\partial p'}{\partial z} = -\frac{m^2}{k^2 + l^2 + m^2} g\rho' \tag{2.22}$$

$$u = -\frac{km}{k^2 + l^2} w_0 \cos(kx + ly + mz - \omega t) = \frac{k}{\omega\rho_0} p' \tag{2.23}$$

$$v = -\frac{lm}{k^2 + l^2} w_0 \cos(kx + ly + mz - \omega t) = \frac{l}{\omega\rho_0} p' \tag{2.24}$$

To illustrate graphically the properties of a gravity wave we can, without loss of generality, consider the $x - z$ plane only, dropping the ly terms in the above equations (this is equivalent to choose a frame of reference with the x axis parallel to the wave vector). The relation between particle motion, wave phase propagation, and density and pressure perturbations is shown in Fig. 2.1. At a given time $t*$, the angle between phase lines, that is lines were the wave have constant properties, and the x axis is $-k/m$ (because $kx + mz = const.$ on phase lines). Choosing $k < 0$, $m < 0$, Fig. 2.1 shows as solids lines the phase lines where u and w reach their maximum and minimum values (wave crests). Open arrows indicate the velocity perturbation vectors. In correspondence of these velocity extremes, positive and negative pressure anomalies develops; since $k < 0$, from 2.23 positive u corresponds to negative p' perturbations and vice versa. Pressure gradient is perpendicular to wave crests. Dashed lines indicated phase lines where velocity and pressure perturbations are zero. Density perturbations are out of phase with respect to w, u, and p' by 90°, therefore dashed lines also represents phase lines where density perturbations reach their maximum or minimum values, labeled as "Least Buoyant Fluid" (that is, heavier than its surroundings) and "Most Buoyant Fluid" (lighter than its surrounding). In fact, extremes in buoyancy are obtained when velocity is zero, that is when air parcels reaches, during their oscillation, the furthest positions from their equilibrium point. In regions where the wave flow goes down (shaded area) the fluid gains buoyancy, while it loses buoyancy where it moves upward. Consider now the time evolution of the wave. Since the fluid moves toward the bottom-right of the figure in the shaded region, gaining buoyancy, while the opposite happens in the non-shaded areas, the Most Buoyant Fluid phase line must moves toward the shaded area, to the bottom-left, and the whole wave will coherently follows this motion. The thick black arrows indicates the direction of phase propagation, that is perpendicular to the oscillation of air parcels.

With an appropriate combination of equations 2.7-2.10 and 2.13, we can write down the energy equation for internal gravity waves (Gill, 1982):

$$\frac{\partial}{\partial t}\left[\frac{1}{2}\rho_0(u^2 + v^2 + w^2) + \frac{1}{2}\frac{g^2\rho'^2}{\rho_0 N^2}\right] + \frac{\partial}{\partial x}(p'u) + \frac{\partial}{\partial y}(p'v) + \frac{\partial}{\partial z}(p'w) = 0 \tag{2.25}$$

where the term in square brackets on the left hand side is simply the wave perturbations total (kinetic + potential) energy E per unit volume:

$$E = \frac{1}{2}\rho_0(u^2 + v^2 + w^2) + \frac{1}{2}\frac{g^2\rho'^2}{\rho_0 N^2} \tag{2.26}$$

which, for the wave 2.17, can be rewritten as

$$E = \frac{1}{2}\rho_0\left(\frac{w_0}{\cos\phi}\right)^2. \tag{2.27}$$

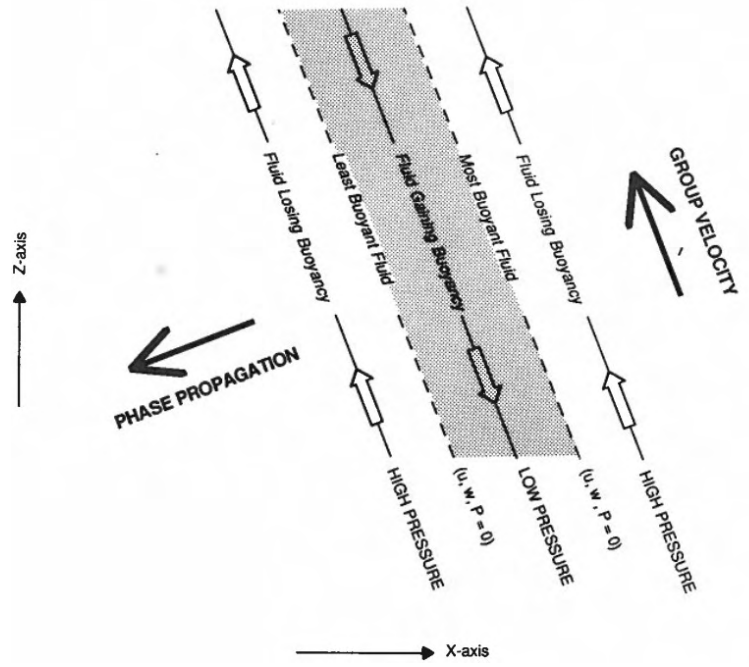

FIGURE 2.1: Pressure, density, velocity perturbations, and phase and group velocity vectors, during the propagation of a gravity wave. Image from (Durran, 1990).

Consequently, eq. 2.25 can be simply rewritten with the following compact notation:

$$\frac{\partial E}{\partial t} + \vec{\nabla}\vec{F'} = 0 \tag{2.28}$$

where the quantity

$$\vec{F'} = p'\vec{u} \tag{2.29}$$

with $\vec{u} = (u, v, w)$ is the energy flux density vector (i.e. the energy flux vector per unit volume) (Gill, 1982). When integrated over a large volume, eq. 2.28 tells us that the rate of change of perturbations energy over the volume is balanced by an equivalent flux of energy across the volume's sides. Therefore, the wave transports energy in the direction of the energy flux vector $\vec{F'}$ (if, for example, the wave transports energy outside the volume, we have a corresponding positive divergence of the energy flux vector in that volume). From the definition of group velocity $\vec{c_g} = (\partial\omega/\partial k, \partial\omega/\partial l)$, it can be shown that

$$\vec{F'} = E\vec{c_g} \tag{2.30}$$

that is the direction of energy propagation coincides with the direction of the group velocity, which is generally true for many types of waves. From Fig. 2.1 we can notice that in regions where $\vec{u}$ (open arrows) point upward there are positive pressure perturbations, while where $\vec{u}$ points downward p' is negative. This means that the group velocity and energy propagation vectors are directed perpendicularly to the phase speed, parallel to the air parcels oscillation and, in the particular case considered here, $\vec{F'}$ and $\vec{c_g}$ always point toward the top-left of Fig. 2.1. In situations where vertical propagation of energy is involved, the vertical component of

$\vec{F}'$, F'_z, is important. For the simple wave considered in this paragraph, eq. 2.17, it is given by

$$F'_z = -\frac{1}{2}\frac{\omega m \rho_0 w_0^2}{k^2 + l^2}. \tag{2.31}$$

The energy flux is therefore upward ($F'_z > 0$) when $\omega/m < 0$, downward otherwise.

2.1.2 Gravity waves forced by an idealized horizontal boundary; N and U constant

So far we considered free gravity waves, produced by an initial perturbation and then traveling on an equilibrium mean state. To describe some fundamental properties of mountain waves, this section is focused on waves forced by the flow over an idealized surface topography h. For simplicity, we will consider only the vertical axis z and one horizontal axis x, oriented perpendicularly to an infinite series of periodic, sinusoidal ridges . This assumption is appropriate if ridges extend indefinitely in the direction perpendicular to the x axis. U is the constant, mean air velocity with respect to the ground in the x direction (is the x component of $\vec{u}$) and N is the buoyancy frequency, also supposed constant. Even if this is a particularly simple and idealized situation, this framework can capture the fundamental properties of mountain waves providing an important guidance for the development of physical parameterizations.

So, if we consider the frame of reference fixed with respect to the mean motion of the air, the topography is seen with a phase velocity $-U$, so is given by

$$h = h_0 \sin[k(x + Ut)]. \tag{2.32}$$

Air at $z = 0$ must follow the surface, therefore its vertical velocity is

$$w \approx U\frac{\partial h}{\partial x} = w_0 \cos(kx - \omega t) \qquad \text{at z=0} \tag{2.33}$$

where $w_0 = Ukh_0$ and $\omega = -Uk$. It follows that, when N is constant, the solution of the wave equation 2.16 with the above boundary condition is

$$w = w_0 \cos(kx + mz - \omega t). \tag{2.34}$$

From the dispersion relation 2.18,

$$m^2 = k^2(N^2 - \omega^2)/\omega^2 = (N/U)^2 - k^2. \tag{2.35}$$

Requiring $k > 0$, the choice of the sign of m is determined considering that, since the energy source of the waves is at the lower boundary (mountains) the wave must be transport energy upward (Gill, 1982). The same conclusion can be reached requiring that waves at an arbitrary high level transport energy away from the mountains (Durran, 1990). Since $\omega = -Uk < 0$, the positive m is chose, in order to have the vertical energy flux 2.31 pointing upward. Consequently, this energy flux is given by

$$F'_z = -\frac{1}{2}\omega m \rho_0 w_0^2/k^2 = \frac{1}{2}k\rho_0 h_0^2 U^2 (N^2 - U^2k^2)^{1/2} \tag{2.36}$$

that correspond to the rate at which energy is supplied to the atmosphere from the surface. However, the solution 2.34 is valid, since eq. 2.35 has real solutions, only when $\omega^2 < N^2$, or $Uk < N$, that is when the intrinsic wave frequency is less than the Brunt-Vaisala frequency. When this is not the case, wave propagation can not be supported by buoyancy, and the solution is

$$w = w_0 \exp(-\gamma z)\cos(kx - \omega t) \tag{2.37}$$

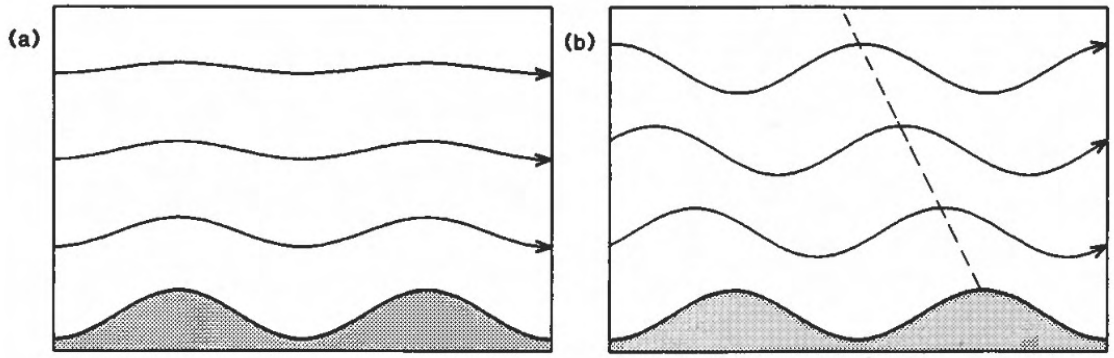

FIGURE 2.2: (a): $kU > N$ (b) $kU < N$. Image from (Durran, 1990).

where $\gamma = (k^2 - (N/U)^2)$ is a real number. This solution exponentially decreases with height, and give rise to evanescent waves.

Summarizing, in an ideal situation where air of constant horizontal velocity U and uniform stratification N flows perpendicularly to an infinite series of sinusoidal ridges, the generation and vertical propagation of gravity waves depends critically on the value of the wave intrinsic frequency kU:

- $kU > N$, "short wavelength" regime: the wave frequency is too elevated to be supported by buoyancy force, therefore air parcels oscillation follows the shape of the underlying terrain, but the amplitude of such oscillations decreases rapidly with height (Fig. 2.2a), without a net energy transport. Calculations show that pressure perturbations are negative on hills and positive in valleys, so there is no net force acting between the atmosphere and the topography.

- $kU < N$, "long wavelength" regime: gravity waves propagates vertically without loss of amplitude. The relations between density, pressure and air parcel motions is of the type shown in Fig. 2.1, but since the wave travels on the mean state, air parcel trajectories follows the lines shown in Fig. 2.2b. Lines of constant phase (dashed line) tilt upstream with height, forming an angle given by $\cos\phi = kU/N$. At surface, energy is continually supplied to the atmosphere at the rate 2.36, propagating upward. This means that at some upper level there must be energy absorption, allowing for an energy transfer from the ground to some remote region, through gravity waves radiation and propagation. Calculation show that in this case, at surface, high pressure is found where particle velocity is upward (that is on the windward side of mountains) and vice versa, so there is a net force exerted by the wind on mountains. This mean that, from the point of view of the atmosphere, topography exert a drag on the atmosphere, due to the generation of gravity waves. The magnitude of the drag force per unit area is equal to the rate τ per unit area at which horizontal momentum is vertically transferred by waves (Gill, 1982):

$$\tau = -\rho_0 \overline{uw} = F_z'/U = \frac{1}{2} k \rho_0 h_0^2 U^2 \left[\left(\frac{N}{U} \right)^2 - k^2 \right]^{1/2} \tag{2.38}$$

where the overbar denotes an average over a wavelength. In the case $kU \ll N$, that is $(N/U)^2 \gg k^2$, the previous expression become (Smith, 1979)

$$\tau = \frac{1}{2} k \rho_0 h_0^2 N U \tag{2.39}$$

which is the common expression for the gridbox-averaged stress used in gravity wave drag parameterizations.

The wavelenght $\lambda_c = 2\pi/k_c$, corresponding to wavenumber $k_c = N/U$ which divides the two types of solution, is equal to the horizontal distance traveled by a particle in one buoyancy period (complete vertical oscillation). Moreover, it corresponds to the horizontal size of the idealized mountain forcing the wave. Using typical values for midlatitudes near-surface wind ($10ms^{-1}$) and N ($10^{-2}s^{-1}$), a value of approximately 6000 m is found (Lauritzen et al., 2015). This is usually considered as the smallest wavelenght of the topographic spectrum able to excite gravity waves when subgrid orography files used to force GWD parameterizations are built. Additional sources of surface momentum flux, including orography on scales smaller than approximately 6 km, can be taken into account by Planetary Boundary Layer (PBL) schemes and Turbulent Orographic Form Drag (TOFD) parameterizations (see Section 2.2 and Chapter 3 for a deeper discussion on how these processes are represented in the CAM model used in this study).

The vertical flux of horizontal momentum 2.39, carried upward by gravity waves, is constant if the waves can propagate stably, and the traveling wave will not exert a net drag force on the mean flow. On the contrary, as can be derived from the horizontal momentum equation for a two-dimensional, inviscid Bussinesq flow (Durran, 2003), a decelerative forcing is exterted on the atmosphere at those levels where the gravity wave flux shows a vertical gradient, that is when the wave experience a dissipation. As shown by Eliassen and Palm, 1961, mountain waves are dissipated at the "critical levels" where $u = 0$. Moreover, other instabilities can cause dissipation: if wave amplitude becomes large with respect to its vertical wavelength, flow streamlines can overturn causing wave breaking and momentum deposition. This condition is favoured by a decrease in atmospheric density, increased static stability and decreasing horizontal wind speed, conditions occurring in the lower stratosphere. Diagnosing vertical gradients in the horizontal momentum flux vertical profile, caused by wave instabilities, is the typical method exploited in gravity wave drag parameterizations to apply drag forces on the atmosphere.

2.1.3 Isolated mountains, vertical variations in N and U, nonlinear effects

The solution found in the previous section are exact only in the limit of a flow across an infinite series of two-dimensional sinusoidal ridges with constant wind speed and stability. More general and realistic situations can be studied (Durran, 2003). For example, an isolated 2-D mountain profile can be expressed in terms of Fourier series and, if N and U are constant, each Fourier component of the resulting wave is given by the solution found for infinite series of sinusoidal ridges. The relative importance of the different Fourier modes in the resulting wave is determined by the Fourier transform of the mountain. When N and U are constant, the generated waves are nearly hydrostatic and mostly above the mountain.

If vertical variations in N and U are allowed, the flow over the isolated ridge can give rise to the so called trapped lee waves downstream of the mountain. However, the amplitude of this wave is finite near the topography and decays exponentially with height when stability decreases and wind speed increases.

Nonlinear effects significantly influence the structure of mountain waves when realistic wind speed and stability profiles are considered or when the the mountain height is comparable to the wave vertical wavelength. In this cases trapped lee waves amplitude is increased and wave breaking and overturning can occur also at low levels, enhancing surface wind speeds.

The diversity of the flow regimes arising from the flow over a three-dimensional mountain can be successfully described in terms of the inverse Froude number $Fr = Nh/U$ (Miranda and James, 1992, Olafsson and Bougeault, 1996), which can be thought as a dimensionless mountain height. This framework is exploited in physical parameterizations schemes (Scinocca and

McFarlane, 2000) to incorporate in models the variety of drag states arising from unresolved orography.

For values of the inverse Froude number well below 1, the dominant physical process that balances the surface transfer of horizontal momentum from the atmosphere to the solid Earth is the vertical transport of horizontal momentum by gravity waves. In this regime, air can flow over the mountains and the physics of orographic drag can be well described in term of vertical propagation of linear waves. When $Fr \approx 1$, low-level wave instabilities can cause wave breaking close to the topography and high-drag states associated with downslope windstorms (Lilly and Zipser, 1972). If $Fr \gg 1$, the strong stability and/or the height of the obstacle forces the air to flow around it, and an even smaller fraction of the vertical momentum flux escapes in form of gravity waves.

2.2 Turbulent orographic form drag

Small-scale topographic obstacles, not able to excite vertically-propagating gravity waves, are expected to produce a turbulent orographic form drag (TOFD) on the atmosphere. This drag force arises from pressure asymmetries between the upstream and the downstream slope of the turbulent flow over hills (Belcher, Newley, and Hunt, 1993).

One of the first fundamental steps toward the inclusion of TOFD in Numerical Weather Prediction (NWP) and climate models came from Mason, 1985, where a formula for the representation of the pressure drag due to small scale orographic features is derived, showing a good agreement with previous numerical works. The author proposed to describe form drag in terms of a roughness length associated with a logarithmic velocity profile. The validity of this approach was supported by the observations of Grant and Mason, 1990, and further theoretical developement were presented by Wood and Mason, 1993. A review of different strategies to include early TOFD parameterizations in models can be found in Xu and Taylor, 1995, while Milton and Wilson, 1996 showed the beneficial effects of the first implementation of a TOFD scheme in the U.K Met Office global NWP model. The effects of stratification and hills shape on form drag, and on the relative importance of form drag and gravity wave drag were studied, using both analytical and numerical models, by Belcher and Wood, 1996.

These works have laid the basis for the exploitation of the concept of an effective roughness length, enhanced with respect to the gridbox-mean vegetative one, to represent unresolved effects of the turbulent flow over small scale orography in climate models. The Turbulent Mountain Stress parameterization implemented in CAM5.3, presented in section 3.6.1, is based in these ideas.

A further advancement for TOFD parameterizations was proposed in Wood, Brown, and Hewer, 2001, where an alternative method to effective roughness length is proposed. Instead of prescribing a roughness length to increase turbulent surface fluxes, an explicit orographic drag profile is calculated and put into momentum equations. This new approach has many advantages. Firstly, the new method can better represent the the dependence of the form drag on wind direction due to orographic anisotropy, while the effective roughness length approach simply represent the overall roughness of the orography within a grid box. Secondly, representing the additional drag explicitly in momentum equations is consistent with what is done with GWD parameterizations, making the working principles of the two classes of schemes more similar and allowing for a future unification of these to kind of schemes. These result are exploited by Beljaars, Brown, and Wood, 2004, who describe the implementation of such a scheme in the ECMWF global NWP model. This scheme, studied in this work, is described in section 3.6.2.

Chapter 3

The Model

3.1 The Community Earth System Model

The Community Earth System Model (CESM) is a global, fully coupled climate model. It is designed to represent the evolution and the mutual interaction of different Earth system components: atmosphere, ocean, sea ice, land surface, land ice and rivers. The CESM model is continuously developed at the National Center for Atmospheric Research (NCAR) in Boulder, Colorado, USA, and by the worldwide community of users. Thanks to its flexibility, CESM and its components can be configured in a variety of ways, allowing the investigation of many aspect of the Earth climate system. CESM can be used to study the past climate, to realize climate projection for the next decades or near-future climate forecast. Each of the aforementioned components represented in CESM are self-sufficient models; the communication between them is ensured and mediated by a coupling software. The present work concerns the atmospheric model, the Community Atmosphere Model (CAM). Therefore, in the following we provide a detailed description of CAM, in its version 5.3.

3.2 The Community Atmosphere Model

CAM, like virtually all modern atmospheric General Circulation Models (GCMs), can be conceptually and practically divided in two main parts: the dynamical core and the suite of physical parameterizations.
The goal of the dynamical core is to advance in time the state of the simulated atmosphere, solving the discretized atmospheric primitive equations. For obvious practical reasons, this can be only done at a finite horizontal and vertical resolution: as discussed in the following sections, the version of CAM used here has a horizontal resolution of half a degree, and 46 vertical levels from the surface up to the stratosphere. In order to take into account small-scale physical processes (smaller than the model grid resolution), parameterizations are used. Their aim is to calculate the effects of the so-called "subgrid" or "unresolved" processes on the "large scale" atmospheric state received from the dynamical core. Therefore, the calculation of local effects of subgrid physics on the model's prognostics variables is performed at each gridpoint; then, the atmospheric state is updated globally and sent back to the dynamical core to advance the simulation further in time.

This sharp separation between resolved and unresolved scales has began to vanish in higher resolution models. In fact, the continuous development of computing technologies has made possible to run state of the art NWP models at resolution of a few kilometers. At these resolutions some processes, like moist convection, which were totally unresolved at coarser resolution, are partially resolved. This fact could limit the benefits provided by present and future high resolution models, since the same process, which is neither well resolved or fully subgrid-scale, can be "double counted", that is (poorly) represented by both resolved dynamics and

parameterizations. This regime has been defined "grey zone" (Kealy, 2019; Vosper, Brown, and Webster, 2016).

3.3 The Spectral Element Dynamical Core

Using CAM, the user can choose to use distinct dynamical cores, based on different numerical and mathematical techniques for the integration of the equations of motion. In this work we always run CAM using the Spectral Element (SE) dynamical core. We report here a general overview of its functioning, based on the information contained in Neale et al., 2012, Dennis et al., 2012 Lauritzen et al., 2018 and Lauritzen and Williamson, 2019, where the interested reader can find more details.

The vertical dimension of the model atmosphere is mathematically described using a hybrid σ-pressure vertical coordinate system. This kind of vertical coordinate system is terrain-following near the surface, while levels close the model top virtually coincide with pressure surfaces. Practically, in order to define and solve the system of primitive equations in terms of a generalized terrain-following vertical coordinate η, it is necessary to specify only a few basic properties of this coordinate. Namely, indicating the surface pressure with p_s, the following properties are required:

- $\eta(p, p_s)$ is a monotonic function of p.
- $\eta(p_s, p_s) = 1$
- $\eta(0, p_s) = 0$
- $\eta(p_t, p_s) = \eta_t$, where p_t is the pressure at model top.

The fourth requirement means that the model top is a pressure surface, simplifying the treatment of boundary conditions; in the case $p_t = 0$, the last two requirements coincide, and the whole coordinate system correspond to the one proposed by Simmons and Strüfing, 1981. The system is closed specifying a null vertical velocity at surface and at the model top.

Arranging the primitive equation in a convenient form, it is not necessary to explicitly define $\eta(p, p_s)$; it is sufficient to specify the function $p(\eta, p_s)$, defining η implicitly. In fact, the only quantities needed to solve the system are p and $\partial p/\partial p_s$ at gridpoints. Consequently, η is defined implicitly through

$$p(\eta, x, y) = A(\eta)p_0 + B(\eta)p_s(x, y) \tag{3.1}$$

where we made explicit the dependence of p and p_s on two generic spatial coordinates x and y, and $p_0 = 10^3$ hPa is a reference surface pressure. This gives

$$\frac{\partial p}{\partial p_s} = B(\eta). \tag{3.2}$$

When the whole set of primitive equations, casted is this convenient form, is discretized in order to be solved numerically, the model atmosphere is vertically subdivided in *nlev* vertical levels η_k (in our model version, *nlev*= 46, so $1 \leq k \leq 46$). The set of η_k levels can be specified defining the numerical coefficients A_k and B_k such that $\eta_k \equiv A_k + B_k$. The numbers A_k and B_k unambiguously define model levels, their shapes and altitudes; in practice, in the 46-levels model used in this work, B_k go from nearly 1 to 0 decreasing monotonically from the surface up to model top; A_k are 0 at the surface, they grows until nearly 200 hPa, then they decrease to approximately 0.00038 toward the model top (consequently, the model top is placed at 0.38 hPa).

This vertical coordinate system is used as a fixed, Eulerian reference during the model run; these are the levels "seen" by the parameterizations and which the model output refer to. However, the system of equations solved by the dynamical core is formulated in Lagrangian form: that is, η_k surfaces are treated as floating material surfaces, whose evolution is determined integrating the equations themselves, starting each time from the surfaces defined implicitly through 3.1. To avoid excessive distortion or intersection of these surfaces, a conservative vertical remapping to the reference Eulerian surfaces is performed every $se\_rsplit \times se\_qsplit$ dynamic time steps (the meaning of these model parameters will be clarified later); then the integration is continued from the reference η_k surfaces. The structure and vertical spacing of the 46 Eulerian levels is shown in Fig. 3.1.

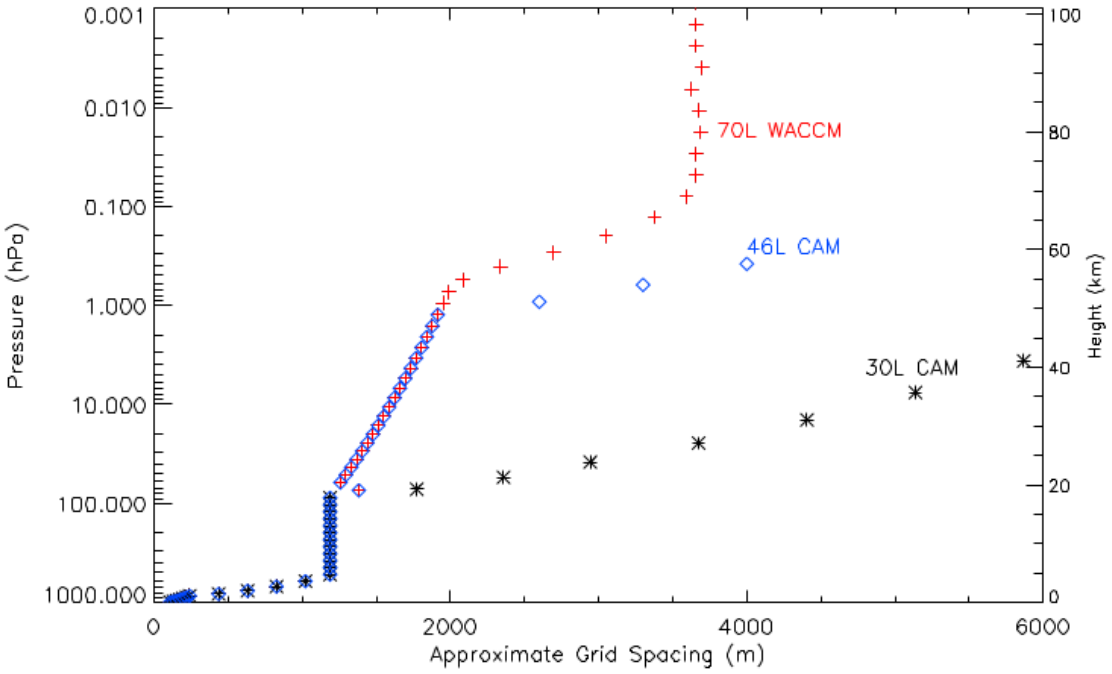

FIGURE 3.1: The structure and spacing of CAM5 vertical levels. In this work, CAM5 is used in its 46-levels version, indicated by blue diamonds ("46L CAM"). Image downloaded from the CESM website (https://www.cesm.ucar.edu/working_groups/Atmosphere/development/vertlev/index_L46.html).

The vertical discretization methods described above are, actually, common to all dynamical cores implemented in CAM. What really distinguish the SE core is the method used to integrate the dynamical equations, namely a continuous Galerkin spectral finite-element method. The horizontal discretization in the SE core is based on the cubed-sphere geometry, introduced by Sadourny, 1972. The surface of the Earth (and of each η_k surface) is divided in a set of quadrilateral, non-overlapping, quasi-regular elements, obtained mapping on the sphere an inscribed cube trough an equal-angle gnomonic projection (Rančić, Purser, and Mesinger, 1996). Each face on the cube is subdivided in $n_e \times n_e$ equal and regular squares so, after the mapping, the sphere is tiled with $6n_e^2$ elements. In Figure 3.2 an example of cubed-sphere grid is shown, with $n_e = 4$.

Each element can be described by two coordinates $x^1, x^2 \in [-\pi/4, \pi/4]$, equal to the gnomonic projection angles. Also, each element can be uniquely remapped back to the cube surface through the gnomonic projection and, combining this last transformation with a translation and a scaling, it can be mapped to a reference square S with coordinates $\xi^1, \xi^2 \in [-1, 1]$.

FIGURE 3.2: The cubed-sphere grid geometry with $n_e = 4$. Image from (Neale et al., 2012).

The SE approach exploit the fact that, on this reference square, we can find the so called Gauss-Lobatto-Legendre (GLL) quadrature points (or "nodes"), and that definite integrals over this domain can be approximated using a Gaussian quadrature rule. GLL nodes are the roots of a suitable basis of orthogonal polynomials: the SE core uses the Legendre polynomials $P_n(x)$ up to a degree $d = 3$. This allows to find $n_p = d + 1 = 4$ GLL points along each dimension of the reference square and, thanks to the mapping described above, $n_p \times n_p$ GLL nodes inside each element. The GLL nodes are not equally spaced inside elements: their positions in the $n_p = 4$ confguration is shown in Figure 3.3. Four of them are well inside the element; eight are on the element's sides and the last four are on the element's vertices. This means that many GLL points (the ones on sides and vertices) are redundant: although they belong to different elements, they represents, in fact, the same physical point, as can be appreciated from Figure 3.3. The consequence of this fact will be illustrated soon. Anyway, the location of GLL nodes over the sphere define the gridpoints: the solution of primitive equations is obtained at GLL points, physical parameterizations are coupled to dynamics and effectively calculated at GLL points, and model output refers to GLL points. Thus, choosing the number of elements in each cubed-sphere face and the number of GLL nodes inside each element (that is, the $n_e - n_p$ pair) effectively determine the model horizontal resolution. In this work the model is run with $n_e = 60$ and $n_p = 4$ (to so called "ne60np4" configuration). So, at the equator, the Earth surface is divided in 4 cubed-sphere faces, each one with 60-elements sides; single elements are divided by GLL nodes in 3 longitudinal sectors of similar size; therefore the model resolution, nearly constant over the planet, is approximately $360°/4/60/3 = 0.5°$. However, the scales of motion effectively resolved by the model are not determined by the distance between GLL points, but rather by the degree d of the polynomial basis P_n in each element. In fact, as illustrated in the following paragraphs, the orthogonal basis functions P_n are used to construct a spectrally truncated solution of the primitive equations inside each element. Therefore, quadrature nodes

(that is, model gridpoints) may be thought as irregularly spaced samples of that underlying spectrally truncated state (Herrington et al., 2019).

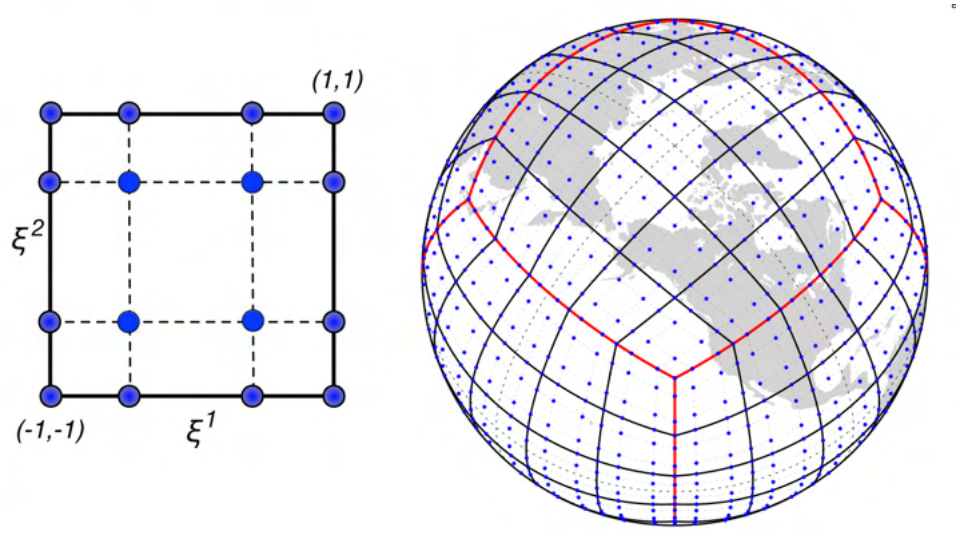

FIGURE 3.3: The CAM SE grid. The surface of the Earth is divided in 6 faces (red segments) tiled, in turn, into $n_e \times n_e$ elements (black lines; $n_e = 5$ in this case). Each element contains $n_p \times n_p$ Gauss-Lobatto-Legendre points, which are the actual gridpoints (blue points, $n_p = 4$). Image from Lauritzen et al., 2018.

The SE algorithm can be outlined as follows. At any GLL point ξ_i a weight w_i can be calculated (its value is defined exactly in terms of $P_n(\xi_i)$) and then, as anticipated before, a definite integral over an element E can be approximated using a Gaussian quadrature rule as

$$\int_E f(x^1,x^2)g(x^1,x^2)dx^1dx^2 \approx \sum_{k=0}^{d}\sum_{l=0}^{d} w_k w_l f(\xi_k^1,\xi_l^2)g(\xi_k^1,\xi_l^2)J_E(\xi_k^1,\xi_l^2) =< fg >_E \tag{3.3}$$

where J_E is the Jacobian associated with the mapping from the element E, with spatial coordinates x^1, x^2 to the reference square S, with spatial coordinates ξ^1, ξ^2. It is important to note that f and g are evaluated at GLL nodes. The above relation holds exactly if fg is a polynomial of degree $2d-1$ or less. From now on we will indicate the operation of estimation of an integral of two functions f and g over an element E through Gaussian quadrature on the reference square as $< fg >_E$, like in 3.3.

The atmospheric primitive equations can be written as an ordinary differential equation for a generic prognostic variable X and a right-hand-side (RHS) term as

$$\frac{\partial X}{\partial t} = RHS. \tag{3.4}$$

The SE method is used to solve this equation in integral form, over the global domain, finding the unique $\partial X/\partial t$ satisfying

$$\sum_{i=1}^{6n_e^2} < \phi_j \frac{\partial X}{\partial t} >_{E_i} = \sum_{i=1}^{6n_e^2} < \phi_j RHS >_{E_i} \tag{3.5}$$

where ϕ_j is a suitable set of basis functions, and the sum is taken over all the $6n_e^2$ elements over the sphere. Therefore, finding the global solution means firstly to solve the problem locally on each element, and secondly to construct a global, smooth and continue 2D function joining

the local solutions. This is accomplished proceeding as follows. First of all, using eq. 3.3, it can be seen that in solving eq. 3.5 we deal with values of ϕ_j, $\partial X/\partial t$ and RHS at GLL points only. Using Lagrange polynomials as basis functions ϕ_j, and using Lagrange polynomial expansion to express RHS and $\partial X/\partial t$ at GLL points, eq. 3.4 becomes, on each element, a system of equations solvable for the unknowns values of $\partial X/\partial t$ at each GLL node. Then, the global solution of eq. 3.5 is obtained joining all elements' solutions. However, as previously mentioned, the same physical location on the global grid can be shared by more than one GLL point, belonging to different elements. This means that more than one solutions, possibly different, are calculated for that points. A global, continuous, unique solution is obtained following a procedure known as Direct Stiffness Summation, which assign unique values to those grid points where multiple GLL nodes from different elements are present, calculating an appropriate weighted average of the distinct solutions.

Other than beneficial mathematical properties (like local conservation of energy, mass and two-dimensional potential vorticity), an advantageous feature of the SE dynamical core is that it can be efficiently implemented on a parallel computer, due to the nature of the method used. The local solutions on each element can be calculated separately and at the same time on different processors; inter-processor communication is needed only to construct the global solution. Moreover, thanks to its quasi-uniform resolution, the SE core is characterized by high scalability and it does not require polar filters.

All tracers, including specific humidity, liquid water and ice are advected solving the discretized continuity primitive equation. The maximum stable timestep to solve this equation is limited by the maximum horizontal wind speed ($\approx 140 ms^{-1}$), while for all the other primitive equations the limit is set by the maximum gravity wave speed ($\approx 340 ms^{-1}$). Therefore, the continuity equations for specific humidity and the other tracers are solved with a longer time step with respect to the other dynamical primitive equations (namely, the momentum, thermodynamic, and dry air continuity equations). So, tracers advection is performed every *se_qsplit* dynamic time steps only.

In order to dissipate energy near the grid scale, to damp the propagation of spurious grid-scale modes and to smooth the global solution at element boundaries, a fourth-order horizontal hyper-viscosity term is explicitly added to the momentum and temperature equations. The hyper-viscosity term for the momentum equation can be written as

$$\frac{\partial \vec{u}}{\partial t} = -\nu \nabla^4 \vec{u} = -\nu \nabla^2 (\nabla^2 \vec{u}). \tag{3.6}$$

where ∇^2 is the Laplacian operator. Using vector identities, we can write

$$-\nu \nabla^2 \vec{u} = -\nu_{div} \nabla (\nabla \vec{u}) - \nu_{vor} \nabla \times (\nabla \times \vec{u}) \tag{3.7}$$

so it is possible to damp differently divergent ad rotational modes. Levels thickness, temperature and tracers are dumped independently using the coefficients ν_p, ν_T, ν_q and an analogous fourth order operator. Details on the appropriate values for this coefficients for different horizontal atmospheric resolution are given in Lauritzen et al., 2018. Hyper-viscosity is sub-cycled with respect to dynamics for computational stability; this is controlled by the *se_hypervis_subcycle* parameter.

Summarizing, the temporal sub-cycling in a complete CAM dynamic cycle can be outlined as follows:

```
do n=1,se_nsplit

     do n=1,se_qsplit

          Solve the continuity equation for tracers
          on floating lagrangian levels

          do n=1,se_rsplit

               Advance the primitive equations of motion
               in floating Lagrangian levels

               do n=1,se_hypervis_subcycle

                    Apply hyperviscosity operators

               end do

          end do

     end do

     Vertical rempapping from floating Lagrangian levels
     to Eulerian levels

end do
```

At the end of each complete dynamic cycle, the atmospheric state is passed to the parameterizations package, that calculates the effects of sub-grid physics on model's prognostics variables. The global atmospheric state is therefore updated, and sent back to the dynamical core to advance the simulation further in time. More details on physical parameterizations and physics-dynamics coupling will be given in the next sections.

The exact lengths of the time steps used to solve the equations, vertically remap levels and apply hyperviscosity are determined in terms of the physics time step, as follows:

$$\Delta t_{remap} = \frac{\Delta t_{phys}}{se\_nsplit} \tag{3.8}$$

$$\Delta t_{tracer} = \frac{\Delta t_{phys}}{se\_nsplit \times se\_qsplit} \tag{3.9}$$

$$\Delta t_{dyn} = \frac{\Delta t_{phys}}{se\_nsplit \times se\_qsplit \times se\_rsplit} \tag{3.10}$$

$$\Delta t_{hyper} = \frac{\Delta t_{phys}}{se\_nsplit \times se\_qsplit \times se\_rsplit \times se\_hypervis\_subcycle} \tag{3.11}$$

where Δt_{phys} is the time step used to compute physical parameterization tendencies. The values of the sub-cycling parameters and of timesteps used in this work are reported in Table 3.2.

3.4 Physics-dynamics coupling

Physical parameterizations are calculated at each "model column" or "physics column". A model or physics column is a set of vertically-aligned points, one for each η_k level; therefore, the total number of columns is equal to the number of gridpoints on each η_k level. Thus, each time a dynamical core cycle is completed, the atmospheric state at model's grid points is passed to the physics package which, in turn, progressively creates an instance of each physical parameterization on each model column. Since there is no communication between adjacent columns, sub-grid physics calculations can be massively parallelized.

The output of a single physical parameterization is the value of the tendency $T_X = \Delta X / \Delta t_{phys}$ of each model prognostic variable X, due to the parameterized physical process, on each η_k level of the considered model column. Δt_{phys} is the physics timestep mentioned in the previous paragraph. Once all physics tendencies were calculated, a net tendency at each gridpoint is obtained and the global atmospheric state is updated and sent to the dynamical core to continue the simulation. However, CAM offers three ways to update the atmospheric state, that is to effectively couple physics and dynamics. The physics-dynamics coupling is controlled by the internal parameter $ftype$, as follows:

- $ftype = 1$: in this case, the entire physics forcing $T_X \Delta t_{phys}$ is added to the atmospheric state before the beginning of a new dynamical cycle. This approach guarantees a closed mass budget for tracers and physical consistency, since the physics forcing is applied to the dynamical state it was calculated for; however, especially if Δt_{phys} is large, this sudden update of the dynamical variables can cause the appearance of spurious gravity waves, detectable as grid-scale noise in model instantaneous output fields. This is the option used in this work.

- $ftype = 0$: to overcome the spurious gravity waves problem, the physics forcing can be divided in *se_nsplit* equal chunks and applied gradually during the dynamics cycle. In particular, in this way, after the computation of physics tendencies, only a forcing $T_X \Delta t_{remap}$ is applied to the atmospheric state; then the dynamics is advanced by Δt_{remap} seconds, a physics forcing $T_X \Delta t_{remap}$ is applied again and so on, until the end of the dynamics cycle. This method effectively removes the problems of spurious gravity waves, but introduces energy and tracer mass conservation errors, due to the fact that the physics forcing is applied to a dynamical state that is different from the state the forcing is calculated for. This can cause hydrological cycle biases in long climate simulations.

- $ftype = 2$: this is a hybrid approach where tracers variables uses the $ftype = 1$ coupling while all other variables use the $ftype = 0$ approach.

More information of physics-dynamics coupling in the CAM SE dynamical core can be found in Lauritzen et al., 2018.

3.5 Lower boundary conditions: topography

Before introducing physical parameterizations, we will spend some words on the model lower boundary conditions, that is Earth topography. In fact, especially for gravity wave drag and form drag parameterizations, the treatment of model orography is fundamental. The content of this section is mainly based on Lauritzen et al., 2015, where the software used to generate CAM orographic input files, *NCAR-Topo*, is described.

The complexity and the fine structure of the real topography cannot be explicitly captured by a finite resolution model. In practice, the information that is known by the dynamical core at every grid point is the mean elevation of the real orography in each gridbox: in the case

TABLE 3.1: SE Dynamical Core and Physics-Dynamics coupling parameters used in this work

Parameter	Description	Value
ne	Number of elements along cubed sphere edges	60
np	Square root of the number of GLL points inside each element	4
se_nsplit	Vertical remapping subcycling	2
se_qsplit	Tracers advection subcycling	4
se_rsplit	Dynamics subcycling	4
se_hypervis_subcycle	Horizontal diffusion subcycling	2
Δt_{phys}	Physics timestep	1800 s
Δt_{remap}	Vertical remapping timestep	900 s
Δt_{tracer}	Tracers advection timestep	225 s
Δt_{dyn}	Dynamics timestep	56,25 s
Δt_{hyper}	Horizontal diffusion timestep	28,125 s
ftype	Physics-Dynamics coupling algorithm	1

of the CAM SE dynamical core, the mean elevation in a representative area around each GLL point (since they are not equally spaced, this area can vary). We will refer to this quantity as "mean orography". The difference between the real Earth topography and the mean orography is the so-called sub-grid orography (SGO). Its effect on the atmospheric flow needs to be accounted for through physical parameterizations. Usually, global climate models have two kind of schemes parameterizng effects of SGO on the large scale, resolved flow, referring to two different classes of physical phenomena: gravity wave drag (GWD) schemes and turbulent orographic form drag (TOFD) schemes. The complexity and the physical realism of such schemes varies from model to model. In any case, these schemes are conceptually distinguished by the different SGO lenghtscales responsible for the two different physical effects. According to linear theory, gravity waves are excited, and their vertical propagation is supported by buoyancy force, only when the local atmospheric Brunt-Väisälä frequency N is larger than their intrinsic frequency. In this case, a drag force is exerted on the atmosphere at the altitude where the gravity wave dissipates (see Chapter 2). In case of orographic waves (that is, waves forced by a surface obstacle at rest with respect to Earth) the intrinsic frequency is determined by the wind speed and by the mountain horizontal size. On the other hand, when obstacles are too small to permit gravity waves generation and propagation, a turbulent form drag is expected to occur in close proximity to the topographic small-scale barrier. Therefore, the horizontal scale separating GWD and TOFD phenomena is flow dependent. Using typical midlatitude values of low level wind (10 ms^{-1}) and N (10^{-2} s^{-1}), it can be shown that gravity waves can be forced by obstacle with horizontal dimension greater that approximately 6000 m (see Chapter 2). This is the value used by *NCAR-Topo* to generate SGO information to force GWD and TOFD schemes. This is one of the main conceptual weaknesses behind these parameterizations, since there is no such sharp and costant scale separation in nature.

Starting from a very high resolution observational datatset of the Earth surface elevation, the *NCAR-Topo* software produces the appropriate mean orography for any grid supported by CAM, and the corresponding SGO information usable by the appropriate CAM parameterizations. The high resolution topographic datasets supported by *NCAR-Topo* are the digital elevetion models GTOPO30, a 30 arcsec global dataset from the Unites States Geological Survey, and GMTED2010 (see Lauritzen et al., 2015 and references therein for details on the datasets). The first step is to map these "raw" high resolution data to a quasi-uniform, approximately 3

km resolution cubed sphere grid. In particular, what is calculated is the mean elevation inside each cubed sphere element (not on GLL points!), the SGO variance inside each element, and the elements land fraction. Using a 3 km grid and a "$2\Delta x$ criterion", we can say that the mean orography on this grid captures orographic variability down to wavelenghts of 6 km, that is the portion of the orographic spectrum able to excite gravity waves. The difference between the mean orography on 3 km cells and the high resolution elevation data constitutes the higher frequency part of the unresolved topographic spectrum, which give rise to the turbulent form drag effects discussed above. Therefore, we will refer to the SGO variance calculated on this grid as $\mathrm{Var}^{3km}_{TOFD}$.

Then, the quantities calculated on the 3 km grid are mapped on the desired model grid. In case of the CAM SE cubed sphere grid, representative areas around each GLL gridpoint are defined, and average values of mean orography, $\mathrm{Var}^{3km}_{TOFD}$ and land fraction are calculated considering the overlap between the target areas and the 3 km elements. The mapping of $\mathrm{Var}^{3km}_{TOFD}$ on the final grid produces $\mathrm{Var}^{final}_{TOFD}$; the quantity that is actually provided to the TOFD scheme is

$$\mathrm{SGH30} = \sqrt{\mathrm{Var}^{final}_{TOFD}}. \tag{3.12}$$

The variance $\mathrm{Var}^{final}_{GWD}$ of the difference between the final grid mean orography and the 3 km resolution mean orography constitutes the forcing for the GWD scheme, since it represents the part of the orographic spectrum able to excite gravity waves (wavelenghts > 6 km) but that is still not resolved by the model. The quantity provided to the GWD scheme is

$$\mathrm{SGH} = \sqrt{\mathrm{Var}^{final}_{GWD}}. \tag{3.13}$$

The surface geopotential is simply $g\bar{h}^{final}$ where g is the gravitational acceleration and $\bar{h}^{final}$ is the mean orography on the final grid. However, in case of a dynamical core with terrain-following vertical coordinate, the mapping procedure described above, without any other filtering, can produce a model mean orography that cause spurious noise in simulations. This is the case of the CAM SE dynamical core. Moreover, the orographic scales credibly resolved by a numerical model (in terms of excited mountain waves) are at least four/six times the model grid spacing (Davies and Brown, 2001). To overcome this problem, the surface geopotential on the final grid is further smoothed through multiple application of the CAM SE Laplacian operator together with a bound-preserving limiter. This procedure removes from the mean orography the highest wavenumbers, reducing the spurious noise problem; however, it breaks down the conceptual decomposition between grid-box averages and deviation from that mean. In particular, the definition of SGH becomes problematic. If SGH is calculated from the non-smoothed orography, while the dynamical core uses the smoothed one, SGH does not represent anymore the orographic variability between 6 km and the "grid scale", since the smoothing further canceled a portion of the spectrum (above the grid scale initially considered to compute SGH). On the other hand, if SGH were recomputed from the smoothed mean topography, its properties would not be suitable for GWD parameterizations: the mean of the deviations from the smoothed orography would not be zero, and non-zero deviations could arise far from the location of the real topographic forcing. The need for additional smoothing of the grid-box mean orography and the subsequent loss of accuracy in the definition of SGH, used to force GWD schemes, is another fundamental weakness of the representation of topographic effects in GCMs (Elvidge et al., 2019). The importance of the topographic smoothing has also been shown by Williams et al., 2020 in the context of an investigation about the drag-related errors in the UK Met Office model.

From our point of view, SGH30 and SGH are the two most important topographic quantities stored in the model's ancillary files. SGH30 and SGH are used to force, respectively, both

the TOFD schemes, and both the GWD schemes (see next sections) studied in this work. However, the newer GWD scheme, the so called "Ridge Scheme", require more information than SGH alone to work properly. In fact, as explained in Section 3.6.4, the calculation of the surface momentum flux and the characterization of different flow regimes are achieved exploiting additional topographic information, archived in supplementary files specifically created.These information is generated by an algorithm whose functioning is briefly illustrated in the following.

The input quantity for the algorithm is h'_{3km}, that is the difference between the mean orography on the 3km cubed sphere grid and the final grid mean orography (the quantity used to calculate $\mathrm{Var}_{GWD}^{final}$). Each cell of the final grid used by the dynamical core (for the SE dycore, each representative area around each GLL point) can therefore be thought as formed by 3km pixels, each one containing the value of the deviation of the 3km orography on that pixel from the dycore cell mean orography. Starting from this information, the algorithm identifies a "skeleton topography", that is the basic structure of the most prominent features of the real (but unresolved on the model grid) topography, on the 3km grid.

Then, 16 equally-spaced orientation angles in the range $[0° - 360°]$ are defined and, starting from the "skeleton topography", in each cell of the final grid a number of properties of the subgrid orography are determined:

- HWDTH: the horizontal width of the unresolved ridges, with respect to the direction perpendicular to each orientation
- CLNGT: the length of the unresolved ridges, along each orientation
- MXDIS: the silouhette of h'_{3km} is calculated along each direction; then, MXDIS is given by the difference between the maximum and the minimum shilouette height along each orientation
- ANIXY: anisotropy of the unresolved orography as seen from each direction

Finally, the physical area of each gridbox (GBXAR) is stored in the topographic files.

3.6 The physical parameterizations suite

3.6.1 The Turbulent Mountain Stress parameterization scheme

The aim of the Turbulent Mountain Stress (TMS) parameterization scheme is to represent the turbulent surface orographic form drag due to unresolved orography. This is done calculating a surface stress τ_{TMS} (that is, a surface vertical momentum flux) using an effective roughness length estimated from the standard deviation of unresolved orography, in particular from the scales below the threshold for gravity wave generation (in our case, *SGH30*). The concept of effective roughness length was introduced first by Fiedler and Panofsky, 1972, who defined it as the roughness length that, given a near-surface wind, a homogeneous terrain would have in order to produce the correct space-average downward flux of momentum at the surface. In fact it is, by definition, a well-suited concept to be used in NWP/climate models, since it provides a quite straightforward method to take into account the surface drag which is "lost" due to the finite resolution of models grids and models mean orographies.

This stress is added to the vegetative surface stress (which, in turn, is estimated by the surface fluxes module of the land model, taking into account vegetation cover and canopy height[1]) inside the PBL/vertical diffusion scheme, to form the total surface stress and thus to give rise to the total turbulent surface momentum flux. Since this flux, as all the other surface fluxes (of heat, moisture and tracers), is deposited into the lowest model layer, the TMS scheme directly affects the lowest model level only. The TMS scheme indirectly affects upper levels through vertical diffusion.

The TMS surface stress is given by

$$\tau_{TMS} = \rho C_d |\vec{V}| \vec{V} \tag{3.14}$$

where ρ is air density, $\vec{V}$ is the lower-level horizontal wind vector, and C_d is a drag coefficient calculated as

$$C_d = \frac{f(R_i) k^2}{ln^2[(z + z_0)/z_0]}. \tag{3.15}$$

Here, $k = 0.4$ is the von Kàrmàn constant, z is the model mean altitude and z_0 is an effective roughness length representing the effects of unresolved orography. It is given by

$$z_0 = \min(0.1\sigma, 100) \tag{3.16}$$

where σ (measured in meters) is the standard deviation of unresolved orography on scale smaller than 6 km (*SGH30*). In the drag coefficient formula, $f(R_i)$ is a function of the Richardson number $R_i = gT_z/(T|\vec{V}_z|^2)$:

- $f(R_i) = 1$ if $R_i < 0$;
- $f(R_i) = 0$ if $R_i > 1$;
- $f(R_i) = 1 - R_i$ if $0 < R_i < 1$.

The TMS surface stress is calculated only over land and only where the topographic altitude above sea level is greater than zero.

[1] https://www.cesm.ucar.edu/models/cesm2/land/CLM4_Tech_Note.pdf

3.6.2 The Beljaars et al., 2004 form drag parameterization scheme

Despite the number of beneficial effects obtained introducing the effective roughness length concept in NWP and climate models (see for example Milton and Wilson, 1996), alternative and more sophisticated schemes have been proposed over the years. In particular, the Beljaars, Brown, and Wood, 2004 parameterization was demostrated to effectively reduce model biases when introduced in the ECMFW IFS model (Jung et al., 2010), replacing the "effective roughness length" scheme.

Starting from a very high resolution ($\approx 100m$) topography dataset for the USA, the authors empirically represented the observed topographic slope spectrum by a piecewise power law of the form:

$$F_o(k) = a_1 k^{n_1} \qquad \text{for } 0.0002 < \mathrm{k} < 0.003\ m^{-1} \tag{3.17}$$

$$F_o(k) = a_2 k^{n_2} \qquad \text{for } 0.003 < \mathrm{k} < 0.012\ m^{-1} \tag{3.18}$$

where k is the wavenumber, and a_1, a_2, n_1, n_2 are numerical coefficient. n_1, n_2 are determined fitting the power laws with the observed spectra, while a_1 and a_2 can be ultimately determined from the variance of the subgrid orography on the scales relevant for turbulent orographic form drag phenomenon, a quantity which can be derived from standard global topographic datasets and constructed for any model (in our case, it is *SGH30*).

Then, exploiting the results obtained by Wood and Mason, 1993 and Wood, Brown, and Hewer, 2001, the authors derived an expression for the vertical profile of the pressure drag caused by the flow over orography.

Using theoretical arguments and numerical simulations, Wood and Mason, 1993 studied the pressure drag force caused by neutral, turbulent flow over topography, considering both two- and three-dimensional flows over idealized, isolated hills with different surface slopes. They finally derived an analytical expression for the pressure force that is valid over a wide range of slopes and in both two and three dimensions, as demonstrated by numerical simulations in different configurations. After some simplifications (justified by the a posteriori evidence of their adequateness, through numerical, single-column simulations), the formula of Wood and Mason, 1993 for the orographic surface stress τ_{OS} is adopted by Beljaars, Brown, and Wood, 2004 in the form

$$\frac{|\tau_{os}|}{\rho} = 2\alpha\beta C_{md}\overline{\theta^2}|\vec{U}(c_m\lambda)|^2 \tag{3.19}$$

where α, β, C_{md}, c_m are numerical coefficients, $\lambda = 2\pi/k$ is the horizontal wavelength of the topography, and $\overline{\theta^2}$ is the variance of the slope of the topography. Since this last parameter can be derived from the topographic spectrum as

$$\overline{\theta^2} = \int_{k_0}^{\infty} k^2 F_o(k) dk \tag{3.20}$$

the surface stress can be rewritten as

$$\frac{|\tau_{os}|}{\rho} = 2\alpha\beta C_{md} \int_{k_0}^{\infty} k^2 F_o(k) |\vec{U}(2\pi c_m/k)|^2 dk. \tag{3.21}$$

Analyzing the previous expression, we can see that the total stress is given by a superposition of contributions from different orographic scales k. Moreover, each scale has a different wind forcing level: forcing by small (large) scales, that is high (low) k, is produced by low (high) level winds.

Then, Beljaars, Brown, and Wood, 2004 applied the idea of Wood, Brown, and Hewer, 2001: instead of converting the drag force into an effective roughness length, they directly prescribed

a vertical drag profile of the form

$$\vec{\tau}_o(z) = \vec{\tau}_{os} e^{-z/l_w} \tag{3.22}$$

where $l_w = 2/k$ is the vertical decay scale. Thus, using the previous results, the vertical stress divergence can be written as

$$\frac{\partial}{\partial z}\left(\frac{\vec{\tau}_o}{\rho}\right) = -2\alpha\beta C_{md} \int_{k_0}^{\infty} F_o(k) |\vec{U}(2\pi c_m/k)| \vec{U}(2\pi c_m/k) e^{-z/l_w} dk. \tag{3.23}$$

Since $l_w = 2/k$, also the vertical decay scale depends on wave number: the flux divergence caused by larger (smaller) scales covers a deeper (shallower) layer.

Recalling equations 3.17, 3.18 for the topographic spectrum, and after some further simplifications needed to fit the previous formula in a climate model parameterization avoiding a computational burden, Beljaars, Brown, and Wood, 2004 demonstrated that eq. 3.23 can be approximated as:

$$\frac{\partial}{\partial z}\left(\frac{\vec{\tau}_o}{\rho}\right) = -\alpha\beta C_{md} C_{corr} |\vec{U}(z)| \vec{U}(z) 2.109 e^{-(z/1500)^{1.5}} a_2 z^{-1/2} \tag{3.24}$$

where $C_{corr} = 0.6$ is a correction factor, $\alpha = 12$, $\beta = 1$, $C_{md} = 0.005$. Written in this form, the entire parameterization depends on a single parameter, namely the variance of unresolved orography (*SGH30*), contained in a_2.

When implemented in the model, the formula is vertically discretized, with z equal to the height of each model level. Analogously to what happens for the TMS scheme, this vertical profile of stress divergence is consistently included inside the PBL/vertical diffusion scheme, together with the the vegetative surface stress. Unlike the TMS parameterization, the direct effect of this scheme are not limited to the lowest model level, since the net effect of the drag profile 3.24 is to generate a wind tendency profile due to subgrid orographic form drag involving a number of vertical levels. The precise shape of the wind tendency profile directly depends on the drag profile 3.24, which in turn is given by the local orographic properties as we explained. The total surface stress τ_{BLJ} is diagnosed vertically integrating the vertical stress divergence profile 3.24.

3.6.3 The McFarlane, 1987 Gravity Wave Drag parameterization scheme

CAM5 gravity wave drag parameterization is based on the scheme proposed by McFarlane, 1987. This parameterization make use of linear theory to describe the evolution of steady, monochromatic, two-dimensional mountain waves; the momentum flux divergence associated with wave breaking is quantified exploiting a wave saturation hypothesis (Lindzen, 1981). In particular, the height Z of the unresolved orographic perturbations is assumed to be of the form

$$Z = h \cos \mu x \tag{3.25}$$

where μ and h are the orographic perturbation wavenumber and amplitude, and x is the horizontal dimension coordinate, assumed positive in the direction of the wind. It is further assumed that the orographic horizontal scales involved, represented by the wavelenght $2\pi/\mu$, are small enough to discard the effects the Coriolis force, but also sufficiently large to consider the flow in hydrostatic balance. This imply

$$\frac{f}{U} \ll \mu \ll \frac{N}{U} \tag{3.26}$$

where f and N are the local Coriolis and the mean flow Brunt-Vaisala frequencies, while U is the mean horizontal wind. The dynamics of linear gravity waves under the above assumptions is described by the inviscid, adiabatic, steady state form of the anelastic equations. Expressing horizontal and vertical velocities and potential temperature in terms of a streamline displacement function $\psi(x, Z)$, and applying suitable boundary conditions (the streamline displacement must be equal to the sinusoidal orography at $Z = 0$), the following equation for the streamline displacement function is obtained:

$$\frac{\partial}{\partial Z}\left[\frac{\overline{U}^2}{\overline{\rho}}\frac{\partial}{\partial Z}(\overline{\rho}\psi)\right] + N^2\psi = 0 \tag{3.27}$$

where overbars denote mean quantites, assumed to depend on the height Z only. Assuming that the vertical variations of the mean quantities happens on lenght scales larger than those characterizing the vertical variations of the streamline displacement functions, a WBK approach can be adopted to solve eq. 3.27, expressing ψ as

$$\psi(Z, x) = A(Z)\cos\left[\mu x + \int_0^Z \phi(Z')dZ'\right] \tag{3.28}$$

where A and ϕ are the wave amplitude and phase. The solution is

$$\phi(Z) = N(Z)/\overline{U}(Z) \tag{3.29}$$

$$A(Z) = h\left[\frac{\overline{\rho}(0)N(0)\overline{U}(0)}{\overline{\rho}(Z)N(Z)\overline{U}(Z)}\right]^{1/2}. \tag{3.30}$$

The average vertical momentum flux carried by the wave is generally defined as

$$\tau = \frac{1}{L}\int_{-L/2}^{L/2}\overline{\rho}uwdx \tag{3.31}$$

where L is equal or larger than an horizontal wavelength. Using the solution 3.29, 3.30 it can be shown that

$$\tau \approx -\frac{\mu h^2}{2}\overline{\rho}(0)N(0)\overline{U}(0). \tag{3.32}$$

The previous expression is, as expected, independent of height (Eliassen and Palm, 1961) but, due to the previous assumptions, it fails when nonlinear, dissipation and saturation effects become important. In particular, eq. 3.32 is no longer valid at critical levels, where $\overline{U}(Z) = 0$, since the amplitude 3.30 tends to infinity. However, nonlinear effects can became non-negligible even far away from critical levels, namely when convective overturning triggers wave instability. Mathematically, the location of these regions can be found checking where the linear theory predicts a negative vertical gradient of the potential temperature (mean flow plus wave), that is an unstable vertical stratification. It can be shown that the approximate condition for convective instability can be stated as

$$-F(Z)\sin(\mu x + \phi(Z)) \gtrsim 1 \tag{3.33}$$

where

$$F(Z) = \frac{N(Z)}{\overline{U}(Z)}h\left[\frac{\overline{\rho}(0)N(0)\overline{U}(0)}{\overline{\rho}(Z)N(Z)\overline{U}(Z)}\right]^{1/2} = \frac{N(Z)}{\overline{U}(Z)}A(Z) \tag{3.34}$$

is the local Froude number. Eq. 3.33 implies that convective overturning instability can happen at altitudes where F is greater than 1. In such conditions, wave energy would be dissipated by

turbulence. The Lindzen, 1981 saturation hypothesis applied here establishes that the effect of turbulence is to dissipate and vertically diffuse an amount of heat and momentum sufficient to limit the wave amplitude below the critical threshold for convective overturning. This can be translated into equations modifying the form of the streamline displacement function with an exponential damping term:

$$\psi = \psi_1 \exp\left[-\int_0^Z D(Z')dZ'\right] \tag{3.35}$$

where ψ_1 is given by the solution 3.28; consequently, the wave momentum flux can be rewritten as

$$\tau = \tau(0) \exp\left[-2\int_0^Z D(Z')dZ'\right] \tag{3.36}$$

where $\tau(0)$ is given by eq 3.32. The saturation hypothesis implies that $D(Z)$ is such that the magnitude of the vertical gradient of the streamline displacement function, $|\partial\psi/\partial Z|$, does not exceed unity, a condition which can be expressed as

$$F(Z) \exp\left[-\int_0^Z D(Z')dZ'\right] \lesssim 1. \tag{3.37}$$

The left-hand side of the previous equation represent an effective Froude number.

The authors demonstrated that the saturation hypothesis is met if

- $D(Z) = 0$ where convective instability does not occur (that is where the local Froude numer is less than unity, or where F exceed unity but the wave amplitude has been reduced enough by wave breaking in lower levels to keep the effective Froude number less than 1, satisfying 3.37)
- $D(Z) = \frac{1}{F}\frac{dF}{dZ}$ where convective instability occurs.

Consequently, in wave saturation regions the wave momentum flux decreases with height according to

$$\tau = \tau(0)/F^2 = -\frac{1}{2}(\overline{\rho}\mu\overline{U}^3/N) \tag{3.38}$$

while it is constant where dissipation does not occur. In general, the wave momentum flux can be rewritten as

$$\tau = \tau(0)\frac{A^2\overline{\rho}N\overline{U}}{A^2(0)\overline{\rho}(0)N(0)\overline{U}(0)} \tag{3.39}$$

where A(Z) keeps the right-hand side of the equation constant with height, except in saturation regions where

$$A(Z) = \overline{U}/N. \tag{3.40}$$

In this way, waves are also completely dissipated at critical levels. From the previous equations it follows that the mean wind tendency is given by

$$\frac{\partial U}{\partial t} = -\frac{1}{\overline{\rho}}\frac{\partial \tau}{\partial Z} = -\frac{\mu}{2}\frac{\overline{U}^3}{N}\max[d(\ln F^2)/dZ, 0] \tag{3.41}$$

Implementation in the model

The surface vertical momentum flux, or stress, is parameterized as

$$\tau_g = |\rho\overline{u'w'}|_0 = \frac{k}{2}h_0^2\rho_0 N_0 \overline{u}_0 \tag{3.42}$$

where k is the wave horizontal wavenumber, h_0 is the streamline displacement at the source level, and ρ_0, N_0 and $\overline{u}_0$ are the density, Brunt-Vaisala frequency and the mean wind also at the source level. The surface streamline displacement is estimated using the subgrid standard deviation of the unresolved orography σ, in our case the quantity SGH defined in eq. 3.13. σ quantifies the height variations from the mean orography of the mountains sufficiently large to excite vertically propagating gravity waves. To avoid wave saturation at the source level in regions of large unresolved orography standard deviation, h_0 is limited following the saturation criterion proposed in McFarlane, 1987:

$$h_0 = \min\left[(2\sigma)^2, F_c\frac{\overline{u}_0}{N_0}\right] \tag{3.43}$$

where F_c is the critical Froude number. Coherently, 2σ also determines the height of the source level, that is the depth to which the typical unresolved mountain penetrates into the atmosphere, from which gravity waves are launched and only above which wind tendencies are applied. The underlying idea is that it is the part of the flow intercepted by the unresolved orography that determines the properties of the gravity wave; therefore, all the source level quantities ρ_0, N_0, u_0, v_0 are defined as a density-weighted mean from the model bottom to the last level intercepted by the unresolved orography:

$$\chi_0 = \int_0^{2\sigma} \chi\rho dz, \qquad \chi \in \{\rho, N, u, v\}. \tag{3.44}$$

u_0, v_0 are the source level wind vector components; they determine the orientation of the parameterization coordinate system and the magnitude of the parameterization mean source wind $\overline{u}_0 = \sqrt{u_0^2 + v_0^2}$. The source wind unit vectors are $(x_0, y_0) = (u_0, v_0)/\overline{u}_0$. The surface vertical momentum flux 3.42 is set to zero when the mean wind at the source level is consedered too slow ($\overline{u}_0 < 2ms^{-1}$) or the subgrid orographic standard deviation too small ($2\sigma < 10m$) to excite gravity waves.

The vertical profile of the vertical momentum flux is determined scanning all the model levels from the source level, where the momentum flux 3.42 is known, up to the model top. Following again McFarlane, 1987, and thus the saturation hypothesis of Lindzen, 1981, the vertical momentum flux at each level k is limited by the saturation value τ^*:

$$\tau_k \leq \tau^* = F_c^2\frac{k}{2}\rho_k\frac{\overline{u}_k^3}{N_k} \tag{3.45}$$

that depends on local density, mean wind and Brunt-Vaisala frequency. τ^* is set to zero at critical levels (where $\overline{u}_k = 0$). Therefore, during the levels vertical scanning, the vertical momentum flux at a given level is assumed to be equal to the value at the level below, unless it is greater than the new value of the local saturation stress or a critical level is found. In this case the vertical momentum flux is set equal to τ^*, and the algorithm proceeds to level above. The physical meaning of this procedure is to produce a vertical momentum flux that is constant when the wave does not cross critical levels or does not experience dissipation processes, while it decreases with height in regions of wave breaking/saturation. The whole stress profile is multiplied by an efficiency factor *effgw_oro*, crudely representing the effect of temporal and spatial intermittency of wave breaking inside the model gridbox.

The second part of the code determines the wind tendency, the aim of which is to reproduce the drag force acting on the flow in regions of vertical momentum flux deposition due to wave dissipation, that is where the stress profile decrease with height. In fact, the stress profile is now scanned from the model top down to the source level, and the wind tendency is determined

differencing the stress profile:

$$\frac{\partial \overline{u}_k}{\partial t} = g\frac{\delta^k \tau}{\delta^k p} \tag{3.46}$$

where $\delta^k X$ means the difference between X at level K and at the level below. However, the wind tendency is limited in particular cases. For numerical stability, the wind tendency can not be greater than $\overline{u}_k / 2\Delta t_{phys}$ (see Section 3.3 for details on the physics timestep) to avoid a sudden sign reversal of the wind and the creation of a critical level; moreover, to limit wind tendencies within a physical plausible range, a limiter of $400ms^{-}1$ is used. When these limiters are activated, to ensure stress conservation the actual stress divergence in the considered layer is re-calculated, and the stress divergence excess is pushed in the level below. The precise vector momentum forcing by orographic gravity waves on the model wind vector $\vec{V}_k$ is obtained projecting back the wind tendency 3.46 on the source wind unit vectors x_0, y_0: the wave drag force on the atmosphere is always parallel to the incident source level flow. Finally, the wave energy loss due to turbulent wave dissipation is translated into a frictional heating term, added to the thermodynamic equation. A graphical illustration of the working principles of the gravity wave parameterization is given in Fig. 3.4

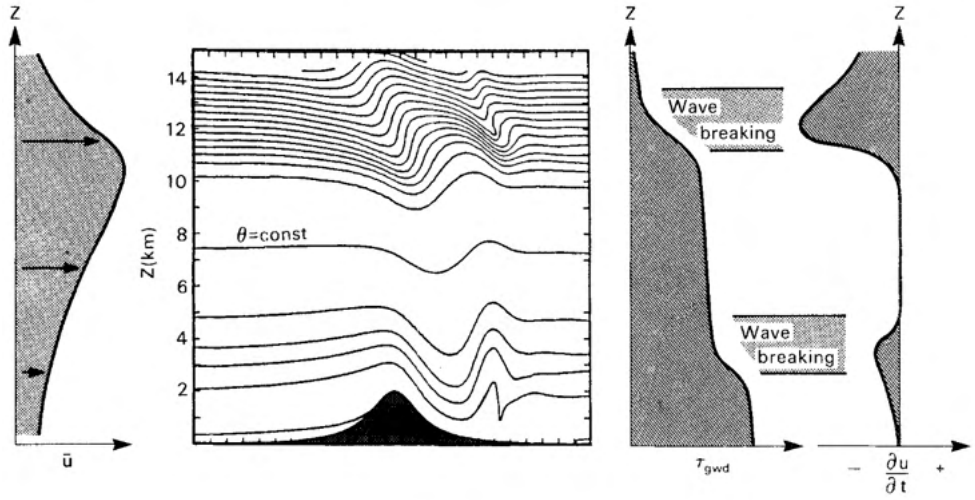

FIGURE 3.4: A schematic of the general functioning of the Gravity Wave scheme. Image from Miller, Palmer, and Swinbank, 1989.

Summarizing, the whole scheme contains three parameters whose values are not known a priori but must be fixed: the wave horizontal wavenumber k, the critical Froude number F_c and the efficiency factor *effgw_oro* modulating the stress profile. They can all be seen as tuning parameters. In linear theory, when gravity waves are produced by an infinite series of sinusoidal ridges, their horizontal wavenumber k coincides with the wavenumber of the sinusoidal topography forcing the waves (Durran, 2003, McFarlane, 1987). Therefore, k can be reasonably thought as the typical wavenumber of the unresolved topography forcing the GWD scheme, and the value of the corresponding wavelenght $\lambda = 2\pi/k$ should be greater than 6000 m (the minimum horizontal scale typically able to excite vertically propagating gravity waves, see Chapter 2) and smaller than model resolution. The value of k hard-coded in the model is $k = 2\pi/\lambda = 2\pi/10^5 m^{-1}$. Consistently with McFarlane, 1987 theory, the critical Froude number for convective instability and saturation in case of a linear, monochromatic wave is close to unity, so in the model is $F_c = 1$ by defalut. Real terrain complexity, wave superposition and nonlinearity, and other sources of instability other than convective overturning could cause gravity waves to break at smaller amplitudes, thus the critical Froude number could be

TABLE 3.2: values of the parameters of the GWD McFarlane, 1987 scheme used in this work

Parameter	Description	Value
k	Gravity wave horizontal wavenumber	$2\pi/10^5 m^{-1}$
F_c	Critical Froude number	1
effgw_oro	Vertical momentum flux efficiency factor	0.0625

smaller and flow-dependent. F_c can be modified by the user via model namelist; however, we have not explored this possibility in the present work. The efficiency parameter *effgw_oro* is probably the most problematic parameter, since theory and observations does not provide us a range of physically reasonable values for it and, in principle, it could depend on model resolution. Its value can be determined carrying out tuning experiment and diagnosing the effects of the scheme on the general circulation and its interaction with other parameterizations. The default value of our CAM5 version is 0.0625. The values of the parameters used in this work are summarized in Table 3.2. Other than the uncertain values of the parameters the scheme depends on, this parameterization suffers from some structural deficiencies, alleviated in more modern algorithms, arising from the simplified treatment of flow dynamics over complex terrain. In particular, as said before, the final wind tendency is always parallel to the incident source level wind vector. From a theoretical perspective, this means that the model treats subgrid orography as a series of circular mountains with typical altitude 2σ, without considering their orientation. This scheme only excites gravity waves with wave crests perpendicular to the incoming flow (so not necessarily parallel to the unresolved mountains, as for real gravity waves) and therefore produces a drag always parallel and opposite to the upstream wind. The other main weakness, strictly connected with the former, consist in the fact that, being the scheme two-dimensional (only height and the horizontal incoming wind direction are considered), flow blocking effect ar not taken into account. The scheme suppose that, except for very low wind velocity when gravity wave production is suppressed, all the incoming flow from the ground up to mountain top is able to pass over the mountain radiating gravity waves, coherently with the linear solution of a 2-D problem. In other words, the scheme assumes that the quantity that represent the average unresolved mountain height, 2σ, is the effective amplitude of the waves, because that is the effective obstacle height seen by the flow. In reality, when 3-D flows encounters 3-D mountains, it could be that near-surface air flows around the obstacle, rather than over it, because its kinetic energy is not sufficient to overtake the mountain potential energy barrier. This fact can limit gravity waves amplitude, while generating low-level flow drag. Nevertheless, this scheme does not produce any wind tendency below the source level, defined exactly as the representative mountain height 2σ.

3.6.4 The new GWD parameterization (the "Ridge Scheme")

As described in Section 3.5, the ancillary topographic files contains more information on unresolved orography other than subgrid orographic variance only. The logic used to describe unresolved orography is coherent with the design of the parameterization scheme which use these additional information, that is the new gravity wave drag and low-level flow blocking scheme. The simplistic method used in the old schemes to force gravity waves was to consider the subgrid orographic variance only, without any information on the orientation of unresolved orography, implying that the drag force acting on the flow is always parallel to the incoming wind. This is not true in the real atmosphere: in fact, the drag force should be perpendicular to the orientation of the real topographic obstacles, and the component of the wind perpendicular

to the obstacle orientation is the only effective forcing for the waves. Therefore, in each grid cell, unresolved orography is described in term of "ridges", along 16 fixed orientation. Coherently with this idea, the new scheme is designed to repeat, in each physics column, the calculation of the unresolved drag effects for each ridge orientation, and then adding up all the partial tendencies and stresses to form the final parameterized forcing due to all orientations. In the following, we describe the procedure used for a single ridge, and repeated for all orientations.

The first key quantity used by the scheme is the streamline displacement at the surface. Conceptually, it represents the average height of unresolved obstacles, that is the top of unresolved mountains. It is set to equal to the quantity *MXDIS* (for the ridge taken into account) described in Section 3.5. Then, the model level whose interfaces contains the altitude *MXDIS* is defined as the source level for mountain waves.

The gridbox-mean variables used by the scheme are the air density, the zonal and meridional component of the wind and the Brunt-Vaisala frequency. Their values are averaged between the lowest model level and the source level. We refer to these quantities as source level quantities. The source level wind vector is then projected along the direction perpendicular to the ridge orientation. Thus, the source level air density, Brunt-Vaisala frequency and the magnitude of the wind component along the on-ridge direction are the key variables used to force the scheme.

At the beginning of the parameterization, some theoretical quantities are calculated, in order to distinguish between different flow regimes.

The m^2 wavenumber 2.35 is calculated, using source level quantities. In linear theory, its role is to measure the relative magnitude of the mountain wave intrinsic frequency and the Brunt-Vaisala frequency: when the former is the greatest, the atmosphere can not support the vertical propagation of the waves, which decades exponentially with height. In the opposite case, propagation without loss of amplitude is possible.

Another fundamental quantity is the inverse Froude number Fr, which quantify the density stratification and can be also taught as the nondimensional amplitude of the orographic forcing. The identification of the different flow regimes depending on the value of the local Fr in the present scheme follows closely the prescriptions of Scinocca and McFarlane, 2000 which, in turn, based their assumption on the numerical works of Stein, 1992, Miranda and James, 1992, and Olafsson and Bougeault, 1996. Theoretical arguments suggest that, up to a critical value Fr_c, the dominant physical process that balances the surface transfer of horizontal momentum from the atmosphere to the solid Earth is the vertical transport of horizontal momentum by gravity waves. In case of greater Fr, other mechanisms (low-level wave instability and flow blocking) come into play and only a fraction of the total surface horizontal momentum flux is vertically transported away from the surface by gravity waves, while the remaining is redistributed in the first vertical wavelength above the topography. Similarly to Scinocca and McFarlane, 2000, by default $Fr_c = 0.7$, but its value can by changed via model namelist. Theoretical arguments suggests that, in case of monochromatic, linear waves, its value should be close to one (McFarlane, 1987); however, as noted in Section 3.6.3, flow nonlinearities and irregularities in obstacles shape can results in lower values of Fr_c. A theoretical justification for the use of low inverse critical Froude number values is suggested by Scinocca and Sutherland, 2010, through the "self-acceleration" mechanism.

As anticipated, the different dynamical regimes taken into account by this scheme are the propagation of gravity waves, the low-level breaking of gravity waves and the flow blocking. Gravity waves are forced only by the part of the flow which has enough energy to pass over the topographic barrier, while the effects of blocked flow dynamics are due to the part of the flow which goes around, rather than over, the mountains. The relative "strength" of the different dynamical processes depends on the local Fr, while the value of the critical Fr_c modulates the height of the "diversion layer", that is the level below which the flow goes around the mountain or is blocked and above which the flow goes over the mountain forcing gravity waves.

The height of the flow diversion layer is determined at each timestep and at each gridpoint based on the resolved properties of the flow. If $m^2_{src} > 0$, that is if vertical propagation of gravity waves is possible, the altitude of the top of the flow diversion layer (TLB), which coincides with the bottom of the region from which linear waves propagates (BWV), is determined by

$$TLB = BWV = MXDIS - Fr_c \frac{|U_{src}|}{N_{src}} \tag{3.47}$$

where the subscript src indicates the source level quantities and Fr_c is the critical inverse Froude number, which has the role of modulating the relative thickness of the two layers. If,instead, $m^2_{src} < 0$, there is no propagation of gravity waves and the flow diversion layer arrives up to the mountain top.

If the vertical propagation of gravity waves is possible, the surface streamline displacement H_{dspwv} for linear waves is set equal to the thickness of the linear wave region: the idea is that the amplitude of waves is less than the total unresolved mountain height if there is a flow diversion layer. Moreover, the orographic stress due to the residual wave field (escaping gravity waves) is calculated as

$$\tau_{oro} = K_{wvrdg} H^2_{dspwv} \rho_{src} N_{src} U_{src} \tag{3.48}$$

while $\tau_{oro} = 0$ elsewhere.

Also, a "linear theory" stress is calculated as

$$\tau_{lin} = K_{wvrdg} MXDIS^2 \rho_{src} N_{src} U_{src} \tag{3.49}$$

that is considering the total unresolved mountain height, instead of a fraction of it due to the presence of the flow diversion layer, while $\tau_{lin} = 0$ elsewhere. τ_{lin} is the stress calculated from linear theory and we use it because the amplification factor due to low level wave breaking is relative to the result of linear theory (Scinocca and McFarlane, 2000).

Then the code calculates the drag due to low level wave breaking following Scinocca and McFarlane, 2000:

$$\beta_{max} = C_{BetaMaxSM} * ANIXY \tag{3.50}$$

where $C_{BetaMaxSM} = 2$; then, depending on the ratio Fr_x between the local and the critical inverse Froude numbers, the DownSlope Wind amplification factor (DWS_{amp}) is given by

$$DWS_{amp} = 2\beta_{max}(Fr_x - 1) \qquad \textbf{if 1<Frx<1.5} \tag{3.51}$$

$$DWS_{amp} = (1 + \beta_{max} - (1/1.5)^2) \left(\frac{3 - Fr_x}{1.5} \right)^2 + Fr_x^{-2} - 1 \qquad \textbf{if 1.5<=Frx<3} \tag{3.52}$$

$$DWS_{amp} = 0 \qquad \textbf{elsewhere} \tag{3.53}$$

.

where $Fr_x = (MXDIS * N_{src})/(U_{src} * Fr_c)$. Then, if DWS_{amp}>0, the stress due to downslope windstorm (wave breaking) is given by

$$\tau_{dws} = (1 + DWS_{amp})\tau_{lin} - \tau_{oro} \tag{3.54}$$

while $\tau_{dws} = 0$ where there is no amplification (wave breaking does not happens).

Summarizing, the stress on levels between the top of the flow diversion layer and the mountain top is given by τ_{oro} (if the vertical propagation of gravity waves is possible); the stress on levels below the flow diversion layer is, in any case, given by the sum of the stress τ_{dws} just

calculated, τ_{oro} and the stress due to flow blocking given by

$$\tau_b = \frac{1}{2} Coeff_{LB} K_{wvrdg} \rho_{src} U_{src}^2 (TLB - z) \tag{3.55}$$

where $Coeff_{LB} = rdg\_cd\_llb * ANIXY$ is a coefficient (rdg_cd_llb is an adjustable numerical factor, its standard value is 1 and it is not modified in this work), TLB is the altitude of the top of the flow diversion layer and z is the altitude of the level considered.

Therefore, the stress is maximum at the surface and decreases upward; the gradient of the stress across the flow diversion layer represents the deposition of momentum at this level due to wave breaking, and the dependence on z in the τ_b term due to the flow blocking determines a deposition of momentum in the levels below the flow diversion layer. If the vertical propagation of gravity waves is not possible, the top of the flow diversion layer coincides with unresolved mountain top.

After the calculation of the stress profile until the mountain top level, a saturation stress for the source level is defined:

$$\tau_{sat} = Fr_c^2 K_{wvrdg} \rho_{src} \frac{U_{src}^3}{N_{src}} \tag{3.56}$$

and the stress at the source level (representing the momentum flux escaping from mountains in the form of linearly propagating gravity waves) is given by $\min(\tau_{oro}, \tau_{sat})$.

Finally, the vertical stress profile above orography is calculated exactly as for the McFarlane, 1987 scheme (see section 3.6.3), except for the $effgw$ factor: here it is not a fixed number, now is given by

$$effgw = effgw\_rdg \frac{HWDTH * CLNGT}{GBXAR} \tag{3.57}$$

where effgw_rdg=1 from namelist. Then, $effgw$ is imposed to be not greater than $effgw\_rdg\_max = 1$ from namelist. That is, instead of assuming the same efficiency factor at any point, the scheme calculates an efficiency which reflects the properties of the local unresolved orography.

3.6.5 Parameterizations of other drag processes

Other parameterizations exert drag on the atmosphere. We have not studied or modified these schemes in the present work, however we briefly summarize their characteristics here.

Non-orographic gravity waves

The non-orographic sources of gravity waves taken into account in CAM5.3 are convection and frontal systems (Richter, Sassi, and Garcia, 2010).

Convective gravity waves are parameterized following Beres, Alexander, and Holton, 2004 and Beres et al., 2005. This parameterization is run whenever the deep convection scheme (Zhang and McFarlane, 1995) is active; the spectrum of the momentum flux phase speed is determined, at each grid point, by the deep convection scheme heating profile and from resolved wind. The waves are launched at the top of convection, everywhere convection is present. Convective GW momentum flux is concentrated in the tropics. As shown by Richter, Solomon, and Bacmeister, 2014a and Richter, Solomon, and Bacmeister, 2014b, this parameterization is an important ingredient to obtain a realistic simulation of the Quasi-Biennial Oscillation.

Fronts are identified using the frontogenesis function reported in Richter, Sassi, and Garcia, 2010. Wherever the frontogenesis exceed a specific threshold at the 600 hPa level, GWs are launched from that level. The momentum flux phase speed spectrum and the waves amplitude are tunable parameters of the scheme. Frontal GWs are more important in the extratropics during winter.

Land and Ocean surface stress

Land surface turbulent momentum flux is calculated by the land surface model component of CESM, and passed to CAM through the coupler. In particular, momentum and heat fluxes for vegetated and non-vegetated areas are calculated from Monin-Obukhov similarity theory applied to the surface layer. More details can be found in Oleson et al., 2010.

The stress over oceans is determined using a bulk formula:

$$\tau_o = \rho_A |\Delta\vec{v}| C_D \Delta\vec{v} \tag{3.58}$$

where ρ_A is the atmospheric density at the ocean surface, $\Delta\vec{v}$ is the velocity of the lowest model level and C_D is a transfer coefficient which, in turn, depend on stability and on surface fluxes. More deteails on the equations and on their solution can be found in Neale et al., 2012.

Vertical diffusion

The vertical, turbulent transport of heat, moisture and horizontal momentum is represented by the Bretherton and Park, 2009 scheme. The scheme diagnoses the presence of convective, stably turbulent and stable levels interfaces depending on the local value of the Richardson number R_i, and turbulence can occur only when R_i is lower than a critical value. Turbulent fluxes are represented by a downgradient diffusion term, and the related diffusivities are calculated using the diagnostic turblent kinetic energy.

The turbulent surface fluxes of momentum from land and ocean mentioned in the previous paragraph, and the TOFD stress calculated by both the TMS and Beljaars, Brown, and Wood, 2004 schemes are consistently used inside the Bretherton and Park, 2009 vertical diffusion scheme to complete the representation of the vertical fluxes of momentum at the surface and in the lowest model levels.

For simplicity, and in order to use a terminology consistent with other works (e.g. Zadra, 2013), in the following we will refer to the turbulent momentum flux over ocean and due to non-orographic land elements as "PBL stress", and the turbulent momentum flux due to unresolved orography (TMS and Beljaars, Brown, and Wood, 2004 schemes) as "TOFD stress".

Chapter 4

Diagnostic Tools

In this short chapter, the diagnostic tools used throughout the thesis are discussed. Diagnostics are objective methods used to measure or quantify specific atmospheric features or processes. In the next chapter, they will be applied both on model output and on reanalysis data, in order to asses model biases in different configurations.

4.1 Torques

The relative atmospheric angular momentum per unit mass is defined as $m_r = ua\cos\phi$, where u is the zonal wind, a is the Earth radius and ϕ is the latitude. The equation for the rate of change of m_r can be vertically integrated and zonally averaged (Swinbank, 1985; Peixoto and Oort, 1992; Brown, 2004) and can be finally written as (Zadra, 2013):

$$-\frac{\partial}{\partial t}[M_r] = [F] + [C] + [T] \tag{4.1}$$

where [ ] denotes a zonal average, and

$$M_r = a\cos\phi \int_0^{p_s} u\frac{dp}{g} \quad \text{is the integrated relative angular momentum,} \tag{4.2}$$

$$F = \frac{1}{\cos\phi}\frac{\partial}{\partial\phi}\left(\cos^2\phi \int_0^{p_s} uv\frac{dp}{g}\right) \quad \text{is the flux convergence term,} \tag{4.3}$$

$$C = fa\cos\phi \int_0^{p_s} v\frac{dp}{g} \quad \text{is the Coriolis term,} \tag{4.4}$$

$$T \quad \text{is the total surface pressure torque.} \tag{4.5}$$

In the framework of global atmospheric numerical modeling, $[T]$ can, in turn, be split into two components:

$$[T] = [R] + [P] \tag{4.6}$$

where

$$R = a\cos\phi\tau_x^{res} \quad \text{is the resolved surface pressure torque,} \tag{4.7}$$

$$P = a\cos\phi\tau_x^{phy} \quad \text{is the unresolved parameterized torque.} \tag{4.8}$$

In turn,

$$\tau_x^{res} = \frac{p_s}{a\cos\phi}\frac{\partial h}{\partial\lambda} \tag{4.9}$$

is the zonal component of the resolved stress, arising from the interaction between resolved flow and resolved orography, and τ_x^{phy} is the zonal component of the unresolved stress, given by the sum of all the parameterized stresses (see chapter 3 for a review of the parameterized stress in CAM). In the previous equations, t is time,λ is longitude, p (p_s) is pressure (surface pressure), g is the gravitational acceleration, f is the Coriolis parameter, v is the meridional wind and h is the elevation of the model resolved orography. R and P have units of Nm^{-1}, representing torques per unit area. To calculate the actual zonal mean parameterized torques (units Nm) shown in this work, each parameterized stress contributing to $[P]$ is multiplied by $a^2 \cos\phi$.

4.2 Blocking indices

The one dimensional index used in this work is the Tibaldi and Molteni, 1990 index. The index is based on the idea of Lejenas and Okland, 1983 of detecting blocks as a reversal of the latitudinal geopotential height gradient, to which an additional constrain is added to avoid the detection of "false positive" blocking patterns (like cut-off lows). At each longitude, two geopotential height gradient are calculated from daily mean data:

$$GHGS = \frac{Z(\phi_0) - Z(\phi_s)}{(\phi_0 - \phi_s)} \tag{4.10}$$

$$GHGN = \frac{Z(\phi_n) - Z(\phi_0)}{(\phi_n - \phi_0)} \tag{4.11}$$

where $\phi_n = 80 + \Delta$, $\phi_0 = 60 + \Delta$, $\phi_s = 40 + \Delta$ and $\Delta = +4^\circ$, 0 or -4°. If, on a given day, both the following conditions are satisfied for at least one value of Δ:

- $GHGS > 0$
- $GHGN < -10 \ \ m/deg$

then the given longitude is considered blocked. To diagnose persistent and stationary blocks ("blocking events"), the "blocking catalogue" of "istantaneous" blocks obtained can be examined to find periods when the same longitude results blocked for some consecutive days.

Many two-dimensional extensions of the Tibaldi and Molteni, 1990 index have been proposed. Here, we adopted the "absolute method" used in Woollings, Barriopedro, and Methven, 2018 to diagnose "istantaneous" blocking in the band [25N-75N]. Now, the following meridional gradients of geopotential height are calculated at each longitude λ and latitude ϕ:

$$GHGN(\lambda,\phi) = \frac{Z(\lambda,\phi+\Delta) - Z(\lambda,\phi)}{\Delta} \tag{4.12}$$

$$GHGS(\lambda,\phi) = \frac{Z(\lambda,\phi) - Z(\lambda,\phi-\Delta)}{\Delta} \tag{4.13}$$

$$GHGS_2(\lambda,\phi) = \frac{Z(\lambda,\phi-\Delta) - Z(\lambda,\phi-2\Delta)}{\Delta} \tag{4.14}$$

and a point is considered blocked if the three following conditions are satisfied:

- $GHGS > 0$
- $GHGN < -10 \ \ m/deg$
- $GHGS_2 < -5 \ \ m/deg$

The addition of the constrain on $GHGS_2$ allows to avoid the detection of subtropical features not able to really block the westerly flow (the "Low Latitude Blocking" described by Davini et al., 2012).

4.3 Jet Latitude Index

The latitudinal variability of the North Atlantic eddy-driven, low level jet over is diagnosed used the Jet Latitude Index proposed by Woollings, Hannachi, and Hoskins, 2010. Firstly, daily mean 850 hPa zonal wind data are selected over the North Atlantic sector [0W-60W; 30N-70N]. These data are low-pass filtered using a Lanczos filter (Duchon, 1979) using a 10-day cutoff frequency and a filtering window of 30 days. The resulting field is then zonally averaged, and the distribution of the daily latitude of the maximum zonally-averaged, low-pass filtered zonal wind is constructed. The index is shown as the frequency of occurrence of the latitudes where the maximum wind speed is found.

4.4 High frequency variability and storm tracks

Extra-tropical storm track activity is often quantified using the variance of synoptic-scale fluctuation of some relevant atmospheric variable (Zappa, Shaffrey, and Hodges, 2013 and references therein). In this work we used high-pass filtered 500 hPa geopotential height daily data. The filtering is performed with a high-pass Lanczos filter (Duchon, 1979) with a cut-off frequency of 6 days and a filtering window of 30 days.

4.5 Sudden Stratospheric Warmings

Sudden Stratospheric Warming are detected using the method proposed by Charlton and Polvani, 2007. The method consider the NDJFMA 10 hPa zonal mean zonal wind at 60N as the proxy to to detect SSWs. Firstly, the days when the 10 hPa zonal mean zonal wind at 60 N become easterly are detected, and defined as the "central dates" of a SSW event. In order to avoid the detection of final warmings, a central date is discarded if the wind does not return to westerly for at least 10 consecutive days before the end of April. Moreover, if two central dates are separated by less than 20 days, they are considered as part of the same event, so the second date is discarded in order to avoid to count the same SSW twice.

4.6 Extreme temperature events: HCWI index

Heat and cold waves are detected using the Heat and Cold Wave Index (HCWI) implemented in the Copernicus European Drought Observatory [1] and based on Lavaysse, Cammalleri, and Dosio, 2018. The index detects consecutive days with extreme temperature anomalies, potentially dangerous for human health. The index uses daily maximum and daily minimum gridded temperature data. At each grid point, an "extremely cold day" ("extremely hot day") is detected if both daily minimum and daily maximum temperature are below (above) a specific daily percentile. In this work, we used the 15th percentile for cold events and the 85th percentile for hot events. The precise threshold values for each calendar day and gridpoint are calculated as percentiles of the temperature distribution on that gridpoint, observed in an 11-day window centered on that day, over a climatological baseline period (in our case, the entire 1979-2017 period). Finally, a cold (heat) wave event is diagnosed on a gridpoint if at least 3 consecutive extremely cold (hot) days are detected.

[1] https://edo.jrc.ec.europa.eu/documents/factsheets/factsheet_heatColdWaveIndex.pdf

Chapter 5

Experiments and discussion

In this chapter, the results of the model experiments are presented. These are subdivided into three groups, shown in consecutive order in the next sections.

First of all, we performed four 10-years model integrations (1/1/1993 - 31/12/2002) switching on and off the different parameterizations in order to run the model with all the four possible combinations of form and orographic GW drag parameterizations at our disposal (oldFD_oldGW; oldFD_newGWD; newFD_oldGWD; newFD_newGWD). This first set of experiments allowed us to investigate the role and the characteristics of each single scheme, and their mutual interaction.

Secondly, we run another set of experiments, over the same time period, using the new parameterizations only, but perturbing the values of some of their fundamentals parameters. These model runs allowed us to explore the sensitivity of the model climate to the values of these parameters, and to clarify their physical effects on the model atmosphere. The precise changes to the model parameters are described in the next sections.

Finally, we run a set of 39 years long experiments (1/1/1979 - 31/12/2017) using some specific parameterizations configurations. These configurations (that is, specific values for the schemes' parameters) were chosen after a physical interpretation of the results of the previous set of experiments, as will be clarified later. Using these longer model integrations, we studied the effects of the new schemes and of their parameters values on the representation of specific atmospheric phenomena.

The results and their discussion are mailny focused on Northern Hemisphere midlatitudes and on the winter season. In all the model experiments, the CAM5.3 atmospheric model is forced with observed SSTs. We used the standard CAM prescribed SSTs dataset, based on the Hadley Centre sea ice and SST dataset version 1 (HadISST1) and on the National Oceanic and Atmospheric Administration (NOAA) weekly optimum interpolation (OI) SST analysis, version 2 (Hurrel et al., 2008).

5.1 The impact of new gravity wave and form drag parameterizations

In the first set of experiments, we replaced the the old surface form drag and orographic gravity wave schemes with the new ones, initially one at a time and then simultaneously. We used the default values of the schemes' parameters, as outlined in chapter 3. Table 5.1 summarizes the characteristics of these experiments. In this section, we are going to study the impact of these schemes on model climate and their interaction.

5.1.1 Zonal mean zonal wind

We begin our analysis discussing the cross section of the DJF zonal mean zonal wind U. Fig. 5.1 shows U for ERA5 reanalysis (top left panel) and for the four possible combinations of old and new parameterizations. The four experiments' panel shows both the zonal mean zonal wind (contours) and the bias with respect to ERA5 (colours).

Experiment name	Description	Period
oldFD_oldGWD	Both old schemes are used	1/1/1993 - 31/12/2002
oldFD_newGWD	New OGWD scheme	1/1/1993 - 31/12/2002
newFD_oldGWD	New FD scheme	1/1/1993 - 31/12/2002
newFD_newGWD	Both new schemes are used	1/1/1993 - 31/12/2002

TABLE 5.1: Summary of the first set of experiments. The model is run for 10 years with different combinations of old and new FD and OGWD schemes.

When using both the old parameterizations, the model shows two different type of bias in the two hemispheres. In the Southern Hemisphere, the structure of the midlatitude jet is reproduced quite well, but the whole jet is displaced too poleward, causing an error dipole at the two sides of the jet core, from the surface up to, at least, 100 hPa. In the Northern Hemisphere, the latitudinal position of the jet is reproduced reasonably well, but the jet is too concentrated and intense, causing a westerly bias at midlatitudes from the surface up to the jet maximum.

The introduction of the new schemes produces beneficial effects. When used singularly, both schemes reduce the amplitude of the zonal mean zonal wind biases in both hemispheres, reducing the jet intensity in the Northern Hemisphere and shifting it equatorward in the Southern Hemisphere. The simultaneous reduction of the biases in both hemispheres, given their different characteristics, is an indication of the increased physical realism of the two schemes.

However, when used simultaneously, the bias in the Southern Hemisphere degrades, going back to values similar to the ones we obtain with the old schemes, while in Northern hemisphere midlatitudes the westerly bias improves even more. In addition, we observe a slightly worsening of the negative bias over Northern Hemsphere high latitudes, above approximately 600 hPa.

Fig. 5.2 shows the vertical average, from the surface up to approximately 100 hPa, of the zonal mean zonal wind (a vertical average of the wind cross sections showed in Fig. 5.1). Here we can find a confirmation of what we already said: the model with old parameterizations (blue line) shows in the SH a too poleward maximum, slightly too strong, while in the NH the latitudinal location of the maximum is captured quite well, while wind speed is exaggerated. The new parameterizations tends to move the simulations toward the observations (black line).

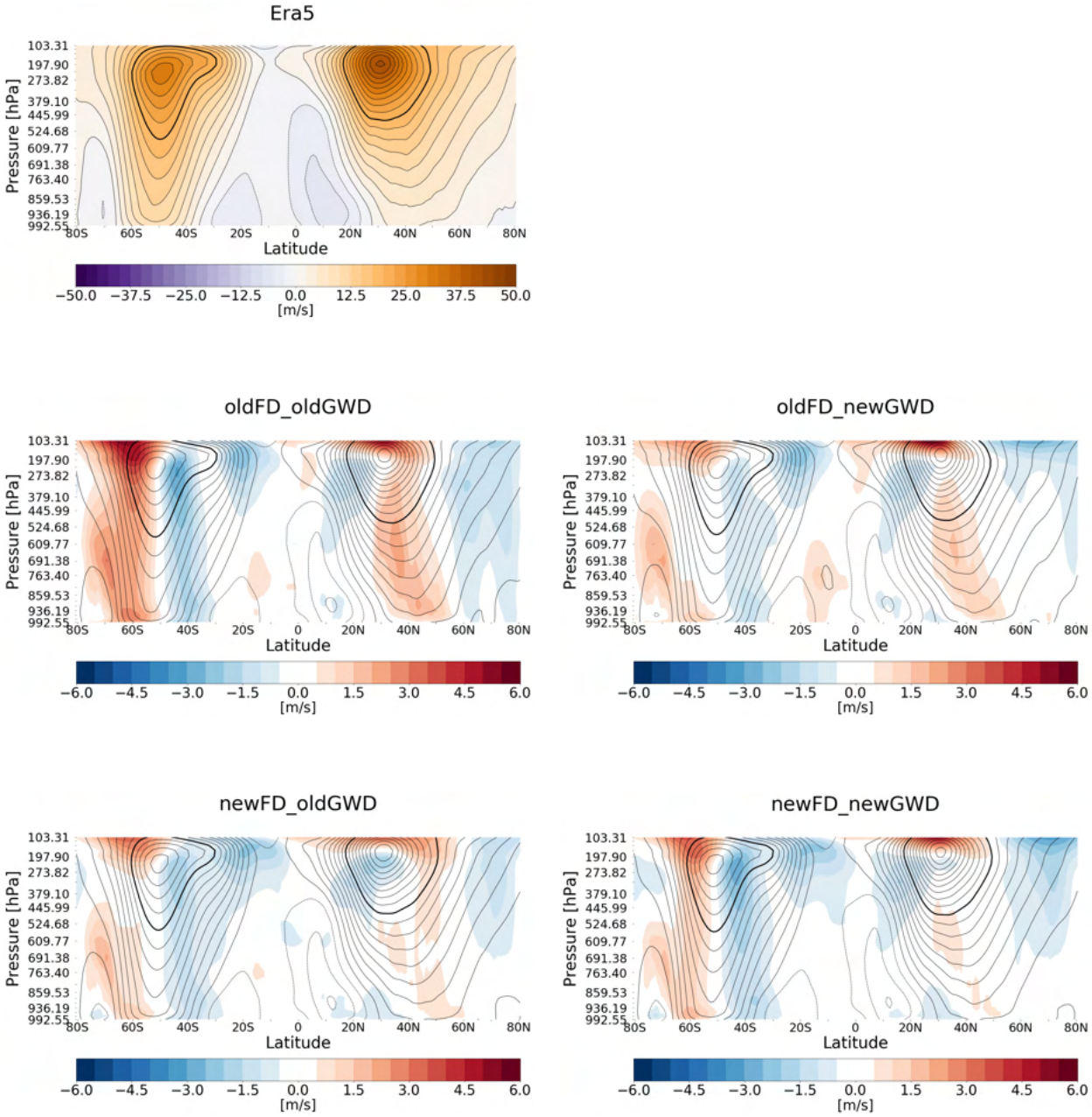

FIGURE 5.1: Cross sections of DJF zonal mean zonal wind. The top left panel displays ERA5 reanalysis data. The other panels show the results of the four model experiments. In the experiments plots, contours represent the zonal mean zonal wind, while colours indicates the bias with respect to ERA5. In all plots, the thicker contour indicates the 20 m/s level; contours are drawn every 2.5 m/s. The pressure values quoted along the vertical axis are the model levels' pressure values.

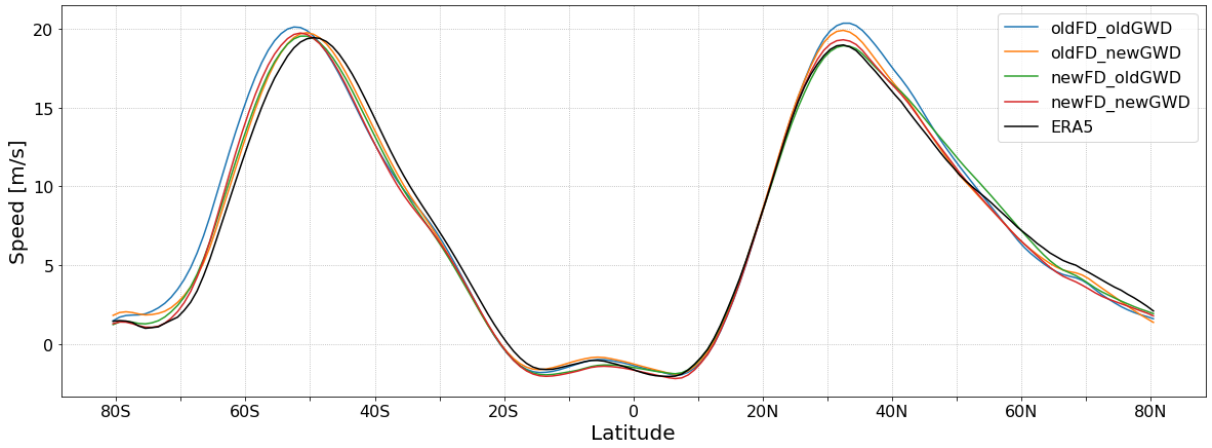

FIGURE 5.2: Zonal mean zonal wind speed, averaged from the surface up to approximately 100 hPa

Fig. 5.3 shows again the zonal mean zonal wind for reanalysis and experiments, with the same panel layout as in Fig. 5.1, but displaying the atmospheric zonal mean zonal wind pattern up to approximately 2 hPa. The most apparent bias present in all panels - that is, independently of the different combinations of parameterizations used - is a strong westerly bias located in the equatorial stratosphere between 60 and 10 hPa. Most probably, this bias is connected to the model inability to correctly simulate the Quasi Biennial Oscillation, and in particular the transition to the easterly phase. A key ingredient for the correct modeling of the QBO is the simulation of gravity waves due to convection in the equatorial regions (this parameterization is present in our model, see chapter 3). However, as shown by Richter, Solomon, and Bacmeister, 2014b and Richter, Solomon, and Bacmeister, 2014a using CAM5 model, a parameterization of this process is not sufficient to have a satisfactory representation of the QBO if it is not accompanied by an adequately high vertical resolution in the model lower stratosphere. These works showed that even in a 60-levels version of CAM5, the QBO westerly phase is too strong. In the Southern Hemisphere, the model does not reproduce the easterly circulation present in the summer stratosphere.

Looking at the Northern hemisphere extratropical stratosphere, we can appreciate some systematic effects of the new parameterizations. The new form drag scheme, when used alone, has a modest effect, however we can notice that it causes a slightly worsening of the bias, due to an acceleration of the stratospheric polar night jet (bottom left panel). On the contrary, the new gravity waves parameterization causes a strong deceleration of the polar night jet (middle right panel) which is slightly less intense when the new OGWD scheme is used in combinations with the new FD scheme (bottom right panel). On the other hand, looking at the Southern Hemisphere we can notice how both the new schemes help in (slightly) reducing the model strong westerly bias in the stratosphere; however, this effect almost vanishes, also in the troposphere, when the new OGWD scheme is used simultaneously with the new FD scheme.

We can summarize these findings saying that:

- the new schemes, on average, when used singularly or simultaneously, have beneficial effects in the troposphere;
- the new FD scheme reduces the zonal mean zonal wind biases in the troposphere, in both hemispheres, and it has a modest, negative effect on NH stratosphere, accelerating (or "decelerating less") the NH polar night jet, but has a slightly beneficial effect on the SH lower stratosphere;

- the new OGWD scheme reduces the zonal mean zonal wind biases in the troposphere, in both hemispheres. In the stratosphere, it has an excessive decelerating effect on the NH polar night jet, worsening the bias overall, while in the Southern Hemisphere lower stratosphere the (modest) decelerating effect is beneficial;
- when used simultaneously, the new FD scheme reduces the effects of the new OGWD scheme in the stratosphere. In the troposphere, the bias worsens in the Southern Hemisphere, canceling out almost all the beneficial effects we observed using the schemes independently, while the bias improves even more in NH midlatitudes.

With respect to the old one, the new OGWD scheme produces more drag in the stratosphere, where gravity waves dissipate, decelerating the NH polar night jet. Independently of the OGWD scheme used, the new FD scheme modulates the amount of high-altitude drag produced by OGWD parameterizations. Since the key input quantity for the OGWD schemes is the near surface wind, we believe that the new FD scheme is able to damp the wind near orographic features more than the old scheme, reducing on average the speed of the wind forcing the OGWD schemes. With respect to the old one, the new OGWD scheme simulates also the effects of low-level flow blocking and low-level gravity wave breaking taking into account ridges orientation, giving rise to a drag in the lower troposphere which was not represented by the old OGWD scheme, and that is difficult to disentangle from the one produced by FD schemes. In the next sections, a deeper analysis to test these hypothesis is presented.

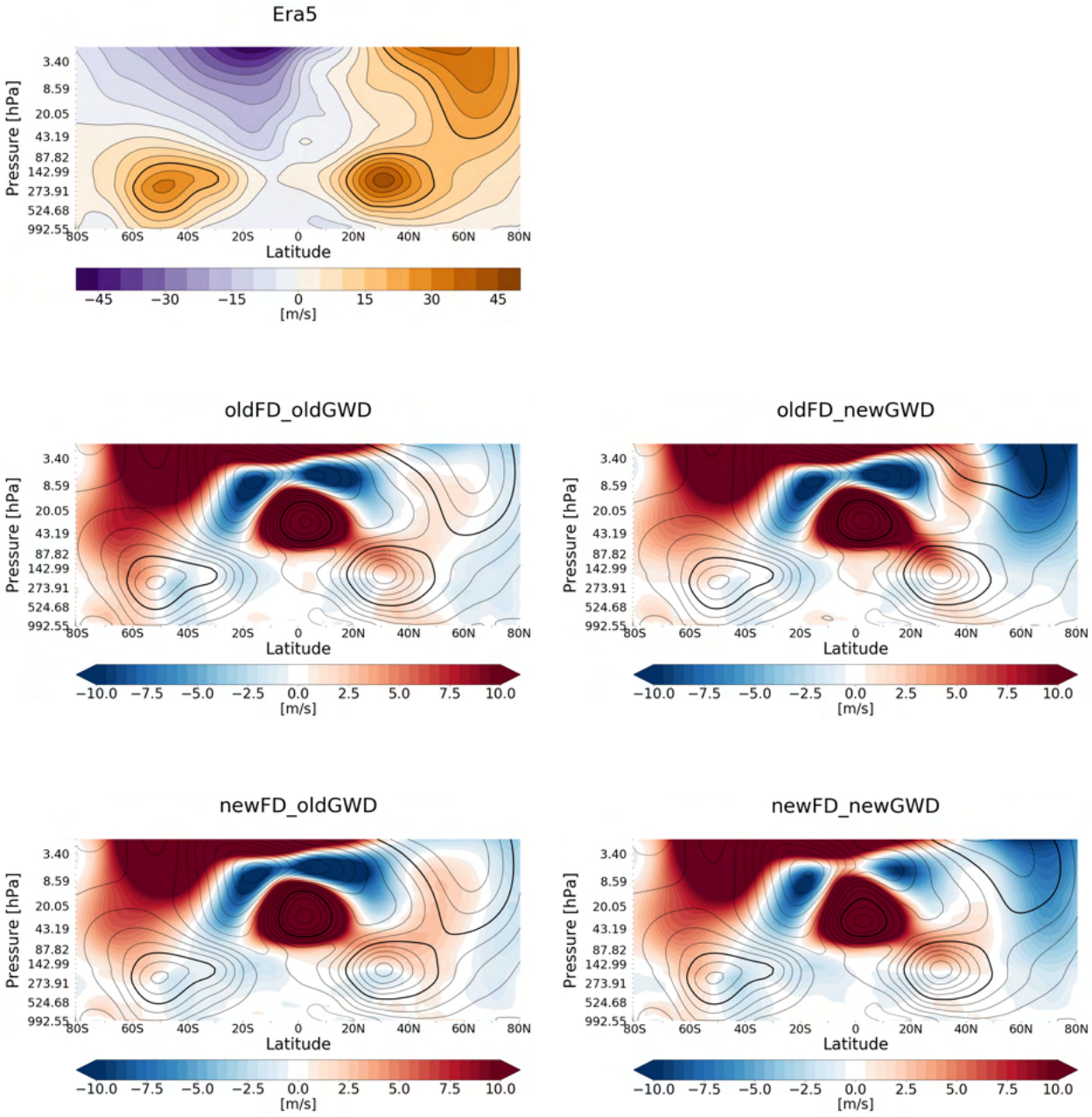

FIGURE 5.3: Cross sections of DJF zonal mean zonal wind. The top left panel displays ERA5 reanalysis data. The other panels show the results of the four model experiments. In the experiments plots, contours represent the zonal mean zonal wind, while colours indicates the bias with respect to ERA5. In all plots, the thicker contour indicates the 20 m/s level; contours are drawn every 5 m/s.

5.1.2 Gravity Wave forcing on zonal mean zonal wind

The direct effect of parameterizations on model wind can be studied looking at parameterized surface stresses and wind tendencies, and at the corresponding wind response.

We start looking at parameterized wind tendencies by orographic gravity wave schemes. Figures 5.4 and 5.6 show the zonal mean zonal wind and the zonal wind tendencies, the latter zonally averaged over land points only, produced by the orographic gravity wave schemes, for the four different model configurations, in the troposphere only (Fig. 5.4) and up to 2 hPa (Fig. 5.4). We choose to zonally average the tendencies over land points only in order to make visible the contributions from Southern Hemisphere orography, which would be nearly invisible averaging over all longitudinal points, due to the large fraction of ocean points in that hemisphere.

Figures 5.5 and 5.7 show the difference between the zonal wind tendencies produced by OGWD schemes when using the new schemes and the same quantity for the oldFD_oldGWD experiment (colours) and the response in zonal mean zonal wind between the same experiments (contours). The aim of these plots is to show how a change in parameterized OGWD tendencies produces the observed response in zonal mean zonal wind.

With respect to the old one, the new OGWD scheme produces more negative tendencies both in the troposphere (in fact, it simulates low-level flow blocking and low-level GW breaking, not taken into account by the old scheme), in the lower stratosphere and near model top (compare right and left panels in Figures 5.4 and 5.6).

The new FD scheme is able to modulate the effects of OGWD schemes, reducing their tendencies (compare top and bottom panels in Figures 5.4 and 5.6). As already mentioned, this is probably due to an increased ability, with respect to the old one, of the new FD scheme in reducing near-surface winds (at least over points with large unresolved orographic variance), the input quantity for OGWD schemes.

Looking at the wind response in the troposphere (Fig. 5.5, contours) we can appreciate how a strong, beneficial response is present even if we use the new FD scheme only (bottom left panel), that is without all the additional, strong negative tendencies produced by the new OGWD scheme. Using the same model configuration, we can see (Fig. 5.7, bottom left) how the negative tendencies produced by the old OGWD scheme are reduced almost everywhere. In the NH stratosphere, this corresponds to the already mentioned acceleration (or "less deceleration") of the zonal wind approximately north of 40N.

If we examine the same plots for the oldFD_newGWD experiment (top right panel of the same figures) we can notice that:

- under approx. 200 hPa, the response in midlatitudes is pretty similar, with a deceleration band between 15N - 55N (well co-located with the region of negative parameterized tendencies) and a poelward displacement of the SH jet;
- however, in the stratosphere the behaviour is opposite: tendencies produced by the new OGWD scheme are almost everywhere more negative with respect to the old scheme, causing a deceleration of the Polar Night Jet poleward of 50 N.

We could say that, thanks to its "low-level" part of the code, the new OGWD scheme is able to improve tropospheric circulation even if used in combination with the old FD scheme. This enhanced low-level orographic drag should be important, since similar improvements, in the troposphere, are obtained if we use the old OGWD scheme - which does not produce any low-level drag - with the new FD scheme, which produces an increased drag close to topographic features. From this point of view, the two schemes could be quite interchangeable. However, care must be taken in order to obtain a satisfactory extra-tropical stratospheric circulation: the low-level drag produced by the new FD scheme basically damps the effects of any gravity wave code, since it slows down, on average, near-surface, near-orography winds; on the other side,

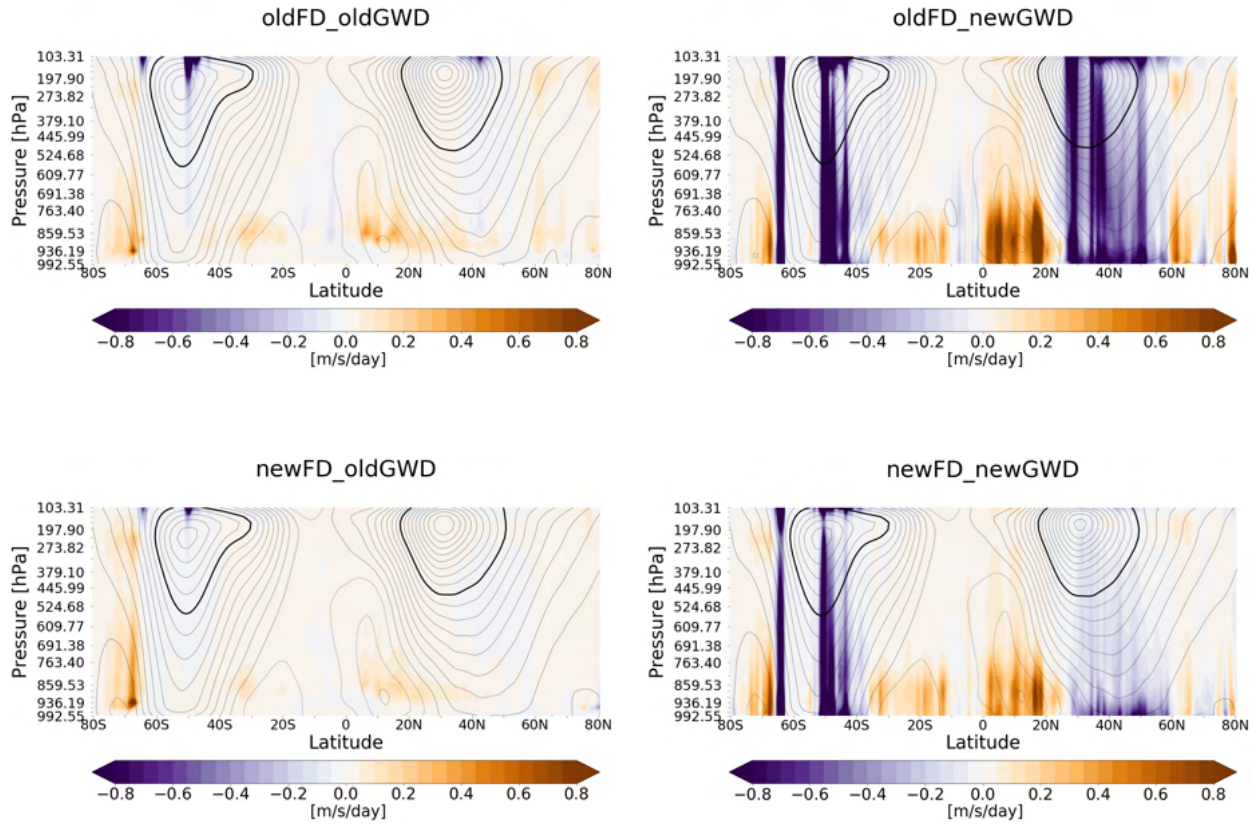

FIGURE 5.4: Cross-section of zonal mean (over land point only) zonal wind tendencies due to OGWD parameterization schemes (shading) and zonal mean zonal wind (contours, averaged over all points) for the four model experiments. In all plots, the thicker contour indicates the 20 m/s level; contours are drawn every 2.5 m/s.

the new OGWD scheme, despite only a part of the calculated surface flux of horizontal momentum escapes in form of gravity waves (a part of it is deposited near the surface, producing the low-level drag), tends to excessively slow down westerly winds producing more negative tendencies in the stratosphere with respect to the old OGWD code.

When we use the new schemes at the same time, the new GWD scheme tendencies are reduced, in particular in the Northern Hemisphere. The fact that a reduction of GWD tendecies in the troposphere caused an improvement in zonal-mean zonal wind in the NH and a deterioration of zonal mean zonal wind in the SH (see Fig. 5.1, bottom right panel) might be an indication that the low level part of the flow blocking - GWD parameterization is too strong in the NH and too weak in the SH, in particular when the code deals with ridges perpendicular to the flow. In fact, the main orographic barrier in the SH are the Andes, a steep mountain chain with a North-South orientation, almost perpendicular to the westerlies, where the flow blocking effect should be of primary importance; this part of the code could be responsible for this contrasting behaviour.

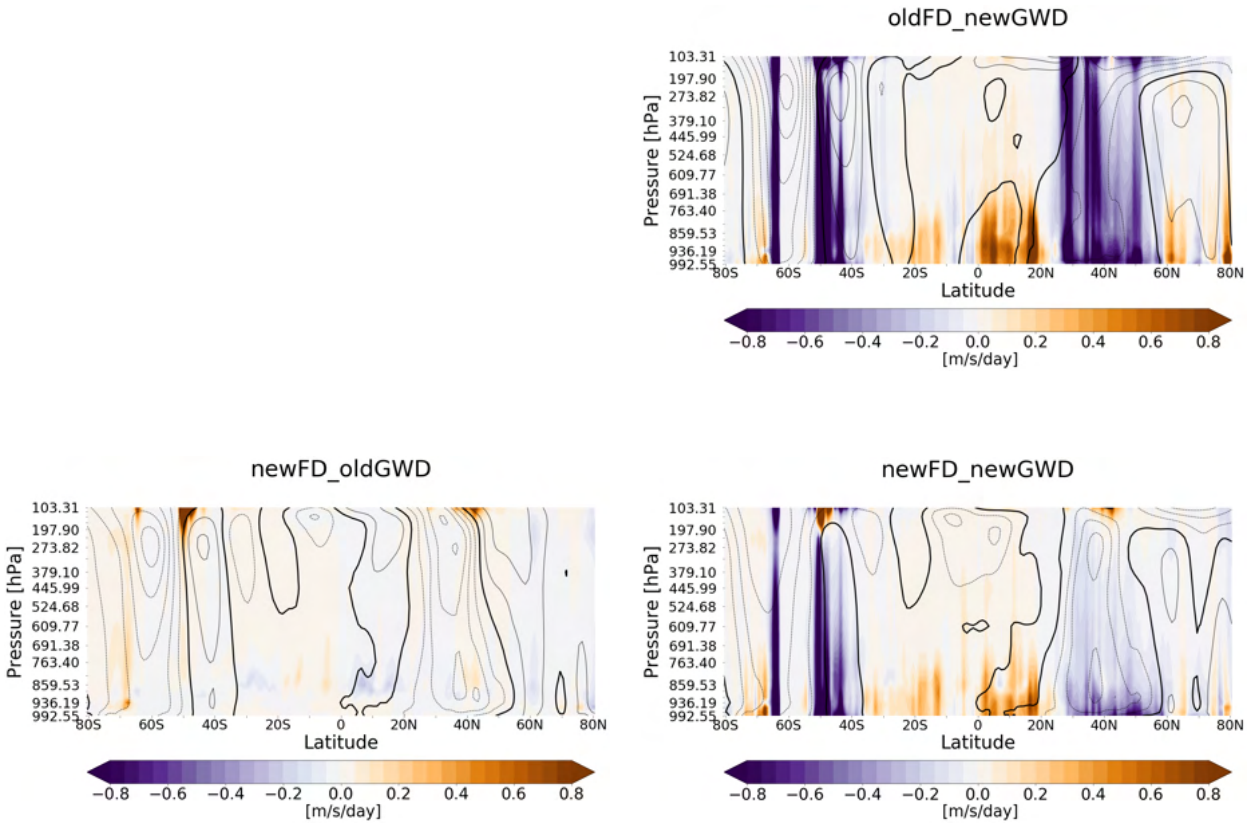

FIGURE 5.5: Difference between zonal mean (over land point only) zonal wind tendencies due to OGW parameterization schemes with respect to the oldFD_oldGWD experiment (shading) and zonal mean zonal wind response with respect to the same experiment (contours). Dotted contours represent negative values, the thicker line mark the zero level. Contours are drawn every 0.5 m/s.

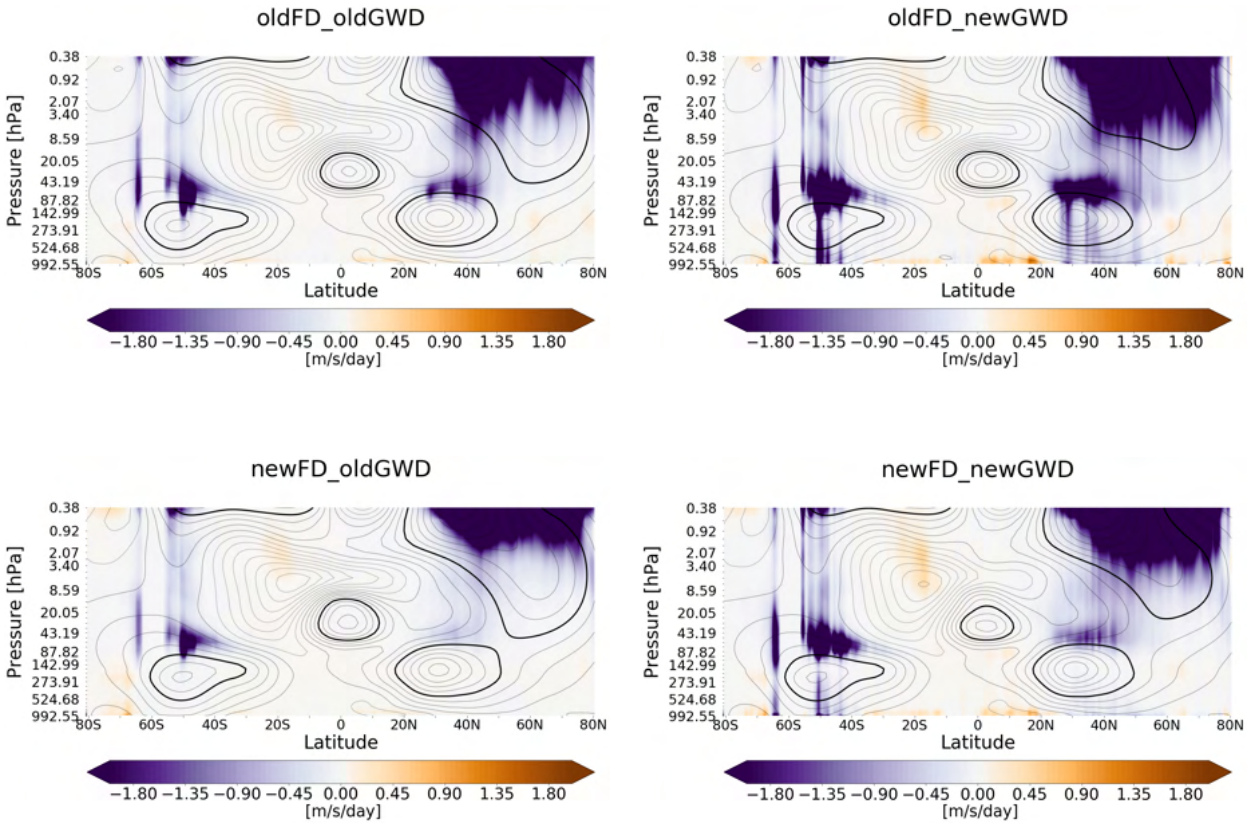

FIGURE 5.6: Cross-section of zonal mean (over land point only) zonal wind tendencies due to OGWD parameterization schemes (shading) and zonal mean zonal wind (contours, averaged over all points) for the four model experiments. In all plots, the thicker contour indicates the 20 m/s level; contours are drawn every 5 m/s.

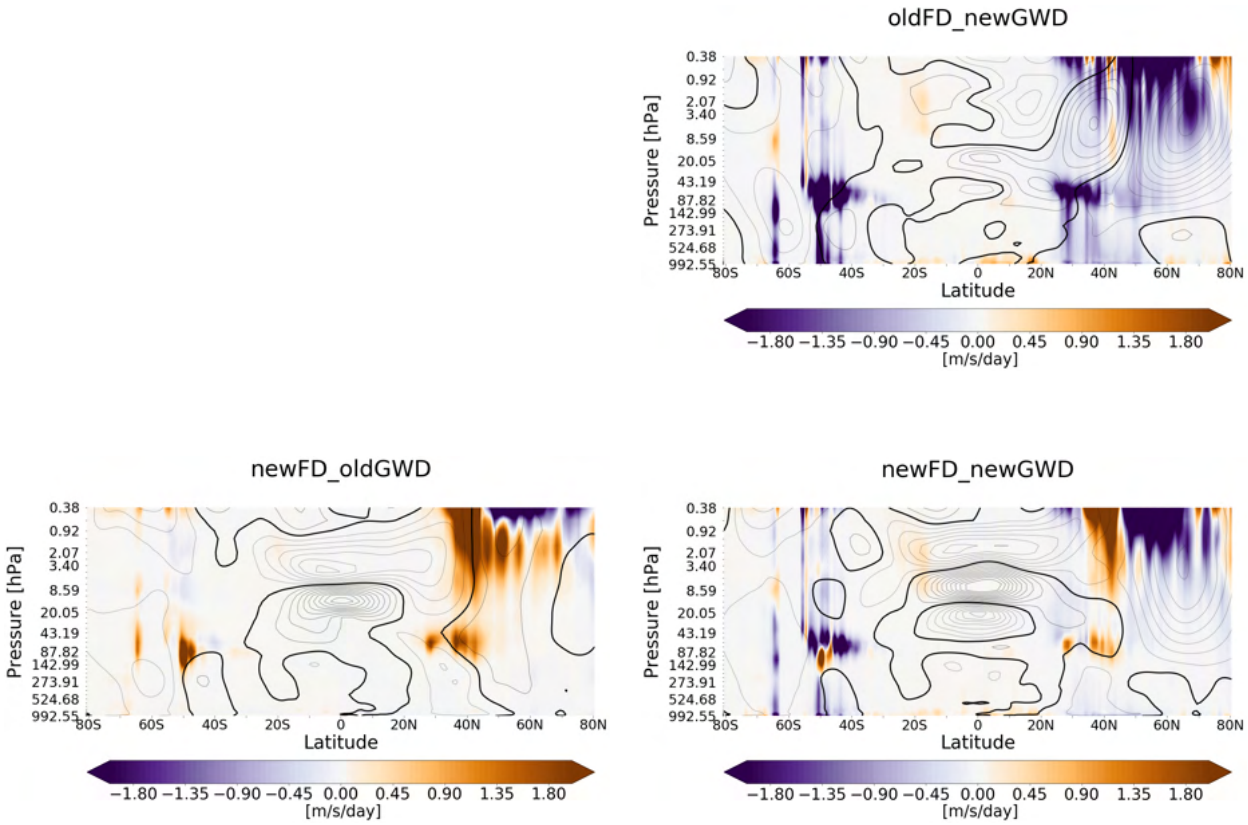

FIGURE 5.7: Difference between zonal mean (over land point only) zonal wind tendencies due to OGW parameterization schemes with respect to the oldFD_oldGWD experiment (shading) and zonal mean zonal wind response with respect to the same experiment (contours). Dotted contours represent negative values, the thicker line mark the zero level. Contours are drawn every 1 m/s.

5.1.3 Form Drag momentum flux profiles

As we said in chapter 3, the new FD scheme does not directly produce tendencies in model history files, since the scheme calculate a momentum flux profile which is then used inside the vertical diffusion parameterization. However, the physical effect of such a vertical profile of horizontal momentum flux is to decelerate the wind, at each level, proportionally to the vertical gradient of the profile. That is, we can use the vertical flux of horizontal momentum to diagnose the drag produced by the new FD scheme. This is the aim of Fig. 5.8, comparing the drag profiles generated by the new FD scheme in the simulations newFD_newGWD and newFD_oldGWD. As discussed in chapter 3, in both cases the drag profiles decreases exponentially with height; the difference between the two cases is negative, implying a larger drag produced by the new FD scheme when used with the old OGWD scheme. This is consistent with the picture we outlined before: since, with respect to the old one, the new OGWD scheme produces a low-level drag, and low-level negative wind tendencies, it inevitably decelerates the wind near orographic features. Since the magnitude of the drag profile from the new FD scheme also depends on the incoming wind, its effect would be inevitably reduced. Thus, we can say that the low-level part of the new OGWD code has a modulating effect on the drag produced by the new FD scheme.

Summarizing, we can say that there is a complicate and delicate interaction between different parameterizations, the goal of which is to simulate different phenomena (but, in the end, all related to unresolved orography and with spatio-temporal scales highly overlapping in reality) which, ultimately, depends on (input) and act on (output) the same variable (wind).

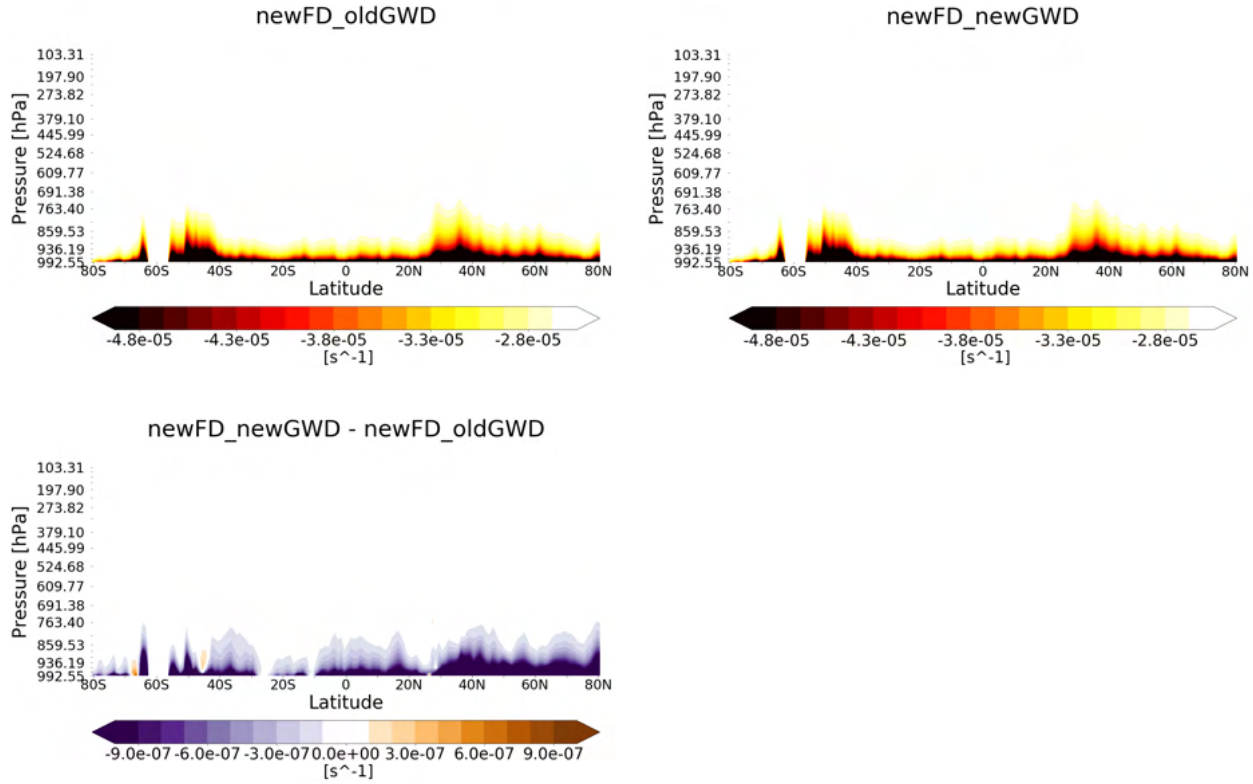

FIGURE 5.8: Top row: cross section of zonal mean (over land point only) horizontal momentum flux due to the new FD parameterization scheme in the newFD_oldGWD (left) and newFD_newGWD (right) experiment. Bottom left: difference between the two upper panels (newFD_newGWD - newFD_oldGWD).

5.1.4 Parameterized Surface Stresses and Torques

The overall physical effect of unresolved drag parameterizations can be studies looking at parameterized surface stresses (i.e. vertical flux of horizontal momentum at surface) and calculating corresponding parameterized torques. They represent the amount of torque exchange between atmosphere and sold Earth added in the model by parameterizations (that is due to unresolved orography). We will distinguish between different "types" of drag, depending on their "origin": stresses and torques due to OGWD parameterizations, due to FD parameterizations, and "PBL stresses/torques" coming from all the land surface processes taken into account by the land model (drag due to vegetation and land uses) and drag over ocean (see chapter 3).

Fig. 5.9 shows the absolute value of the zonal surface stress calculated by form drag parameterization, in the four model configurations considered. Comparing top and bottom rows, we can immediately see how the new FD scheme (bottom) produces less stress far from steep orography (look at North American Great Plains and western Russia) but higher peak values of stress in correspondence of the mountain chains. The old FD scheme produces a more uniform and less spatially-variable stress. This confirms our previous findings: the new FD scheme exerts higher drag on near surface wind in correspondence of high unresolved orography variance, causing a weaker forcing wind for OGWD parameterizations.

Looking at Fig. 5.10 we can see that the highest values of zonally averaged parameterized torque are reached when using both old parameterizations (blue); when using the new FD scheme (red and green) the zonally averaged torque is usually smaller, except in the band 25-35N; when using the new OGWD scheme (red and orange) the torque is usually lower (the new OGWD scheme decelerates near-surface wind, reducing the parameterized stress from FD parameterizations).

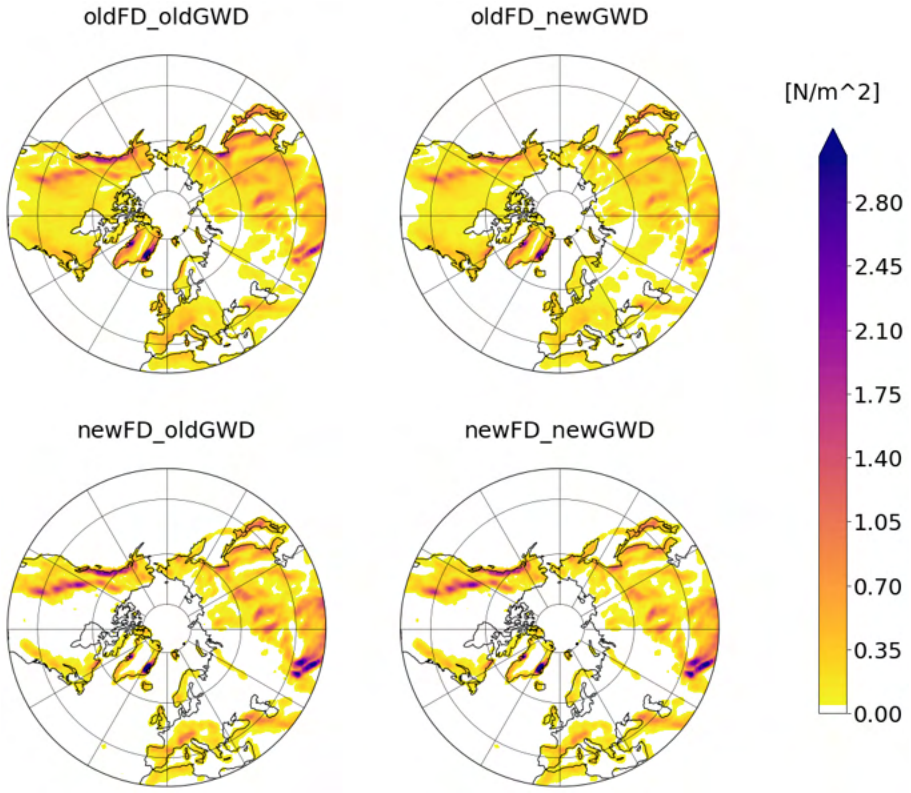

FIGURE 5.9: Absolute value of the parameterized form drag stress.

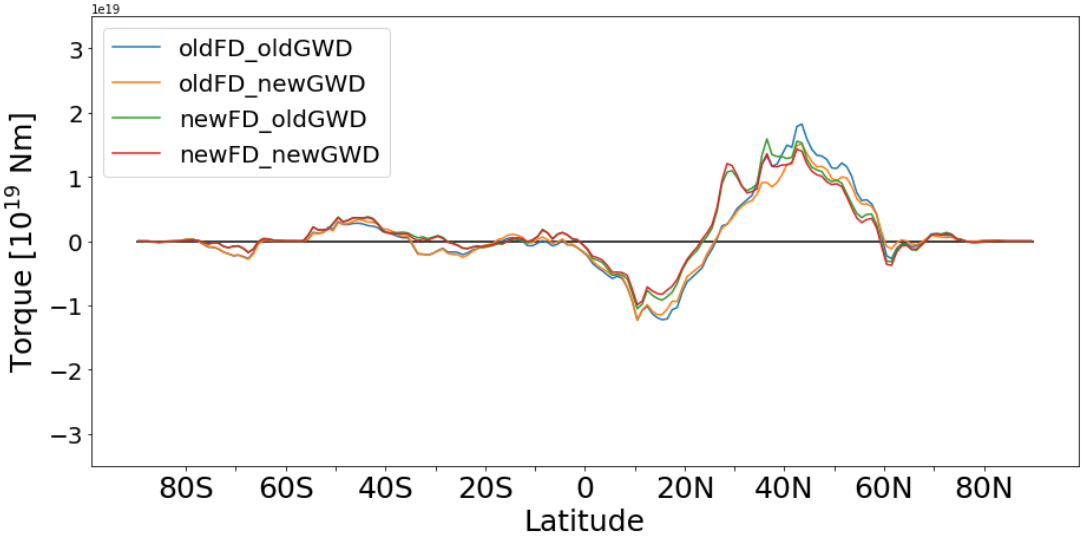

FIGURE 5.10: Parameterized torques due to form drag schemes.

Considering OGWD parameterizations (Figs. 5.11 and 5.12), we can notice that the new scheme produces clearly higher surface stresses, more diffused over continents and reaching higher peak values (left vs right panels in Fig. 5.11). The use of the new FD scheme causes a decreased surface stress due to OGWD schemes . This can be appreciated well also from Fig. 5.12, where we can see how the zonally averaged OGWD torque drastically drops whenever we use the new FD scheme.

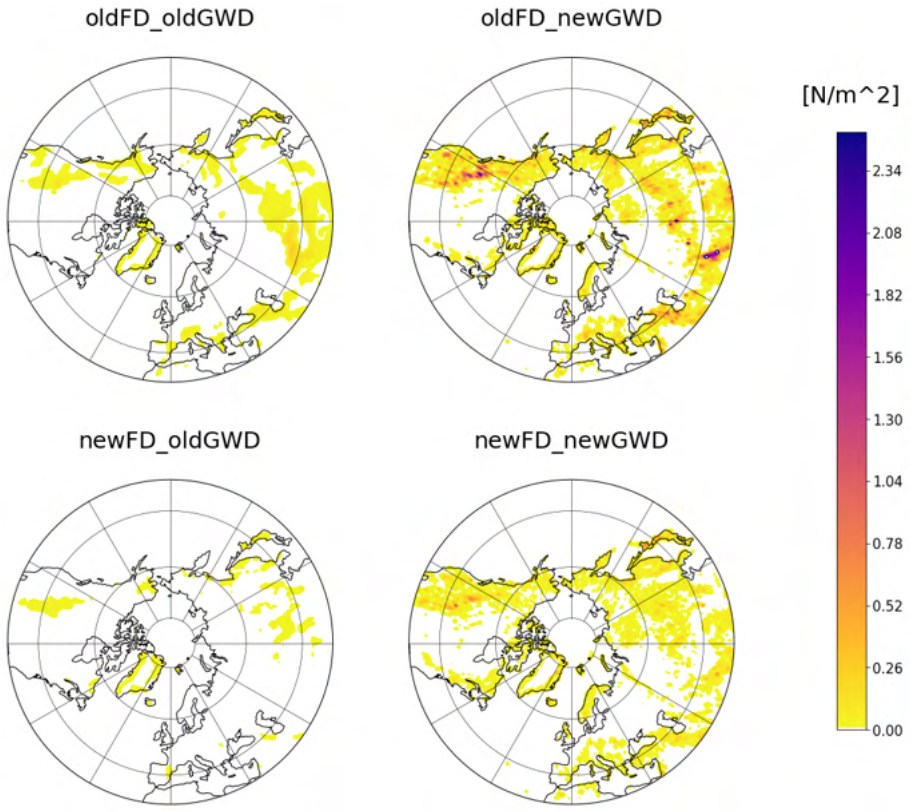

FIGURE 5.11: Absolute value of the parameterized OGWD stress.

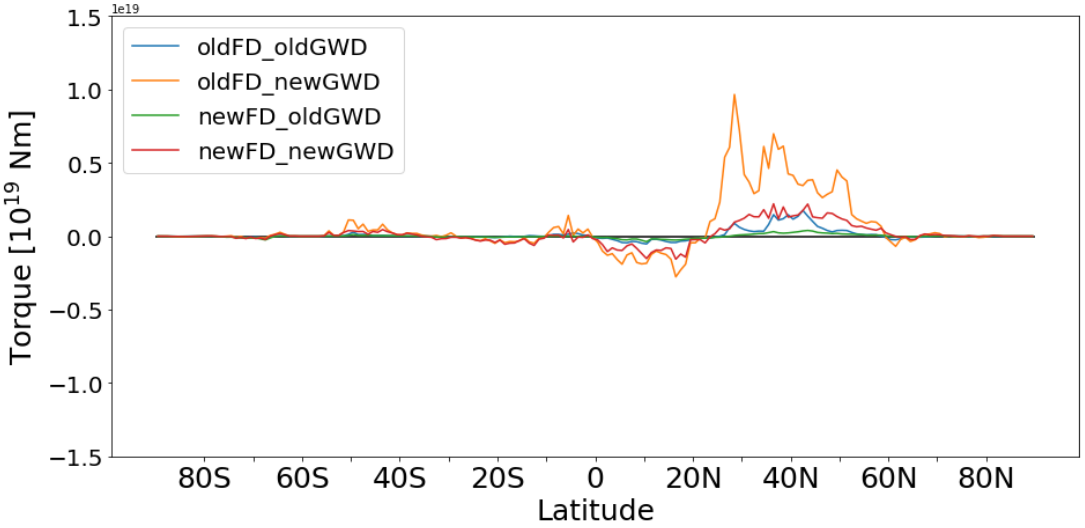

FIGURE 5.12: Parameterized torques due to OGWD schemes.

Figs. 5.13 and 5.14 show the surface stress and the zonally averaged torque from the land module and due to drag over oceans. Over land, surface stress is located mostly over plain regions. Using the new FD scheme, an higher drag is obtained over these regions, corresponding to a stronger near-surface wind there (Fig. 5.15). This is consistent with the picture we outlined above: being the new FD scheme surface stress higher near big mountain massifs but lower over the rest of the continents, wind on plain regions will be on average higher, producing an higher stress from the land module. ERA5 reanalysis may not be the best data source for 10 meter wind speed, since this parameter is derived from internal parameterizations of the reanalysis model and not directly from observations (even if it has been proven to be a valuable product: Molina, Gutiérrez, and Sánchez, 2021). In any case, more than looking at the absolute values of the biases shown in Fig. 5.15, we are interested in the relative differences between the results obtained with different model configurations.

Differences can be seen also over oceans: the highest values of stress over NA and NP are obtained when the old schemes are used simultaneously. High stresses over NA are found also when the newFD scheme is introduced. Since we have not changed the parameterization of drag over ocean, the differences we see should be directly related to the speed and location of the winds over oceanic basins. Again, this is confirmed by Fig. 5.15: the highest 10m wind speed values over NH oceanic basins are found in the simulations we mentioned.

Finally, Fig. 5.16 shows the total, zonally averaged parameterized torque. In the NH, using both the old parameterizations, the highest torque values are reached; in general, the new schemes tend to reduce the total parameterized torque in the band 35N-55N.

The values of all the parameterized torques we showed are realistic and comparable with the same quantities calculated by other GCM. In particular, the previous graphs can be compared with Zadra, 2013, finding an order-of-magnitude agreement between our result and what is found with other state-of-the-art models, remembering that quantifying the amount of the total parameterized drag and its partitioning between different schemes is one of the current open challenges in this field (see also the discussion in Chapter 1).

The effects of different combinations of schemes on parameterized stresses and torques are related to changes in the simulated wind, as clarified in the next sections.

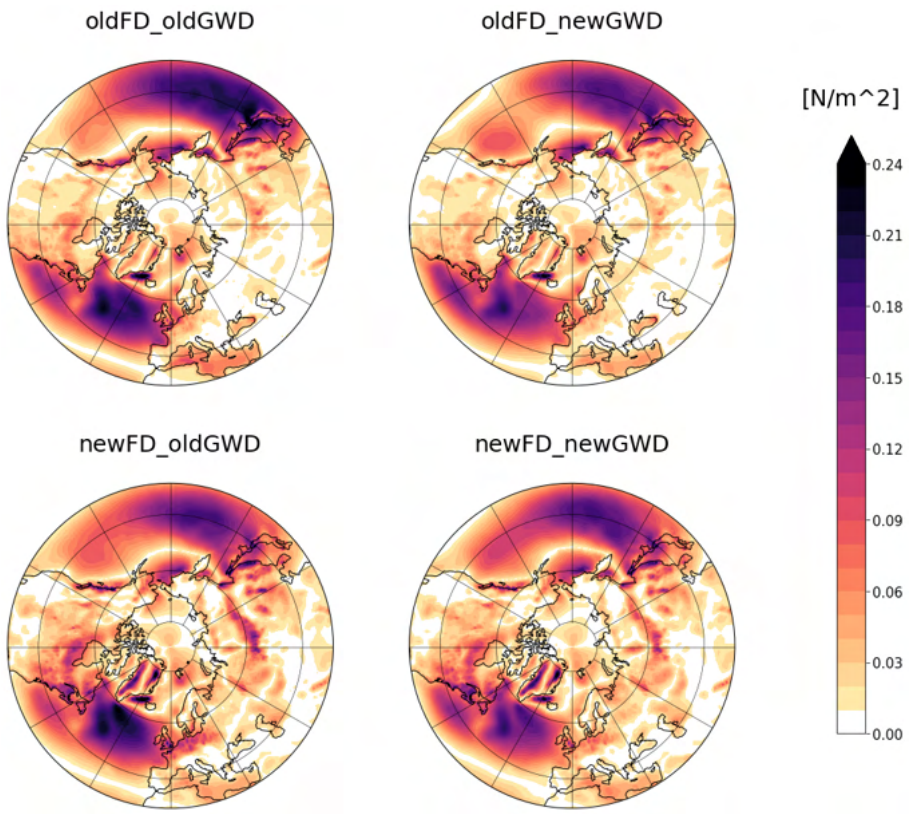

FIGURE 5.13: Absolute value of the parameterized PBL stress.

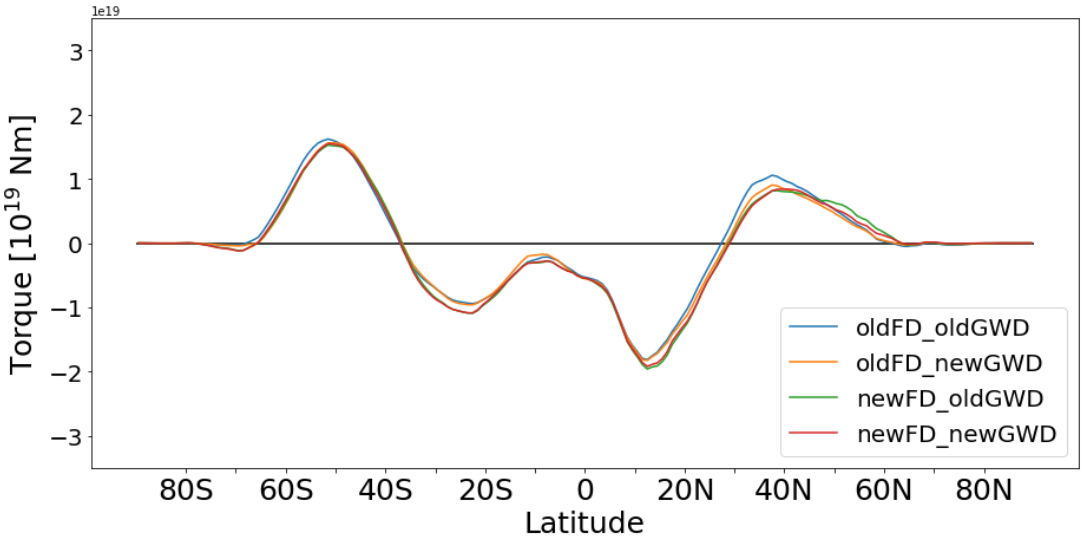

FIGURE 5.14: Parameterized torques due to drag over land and ocean.

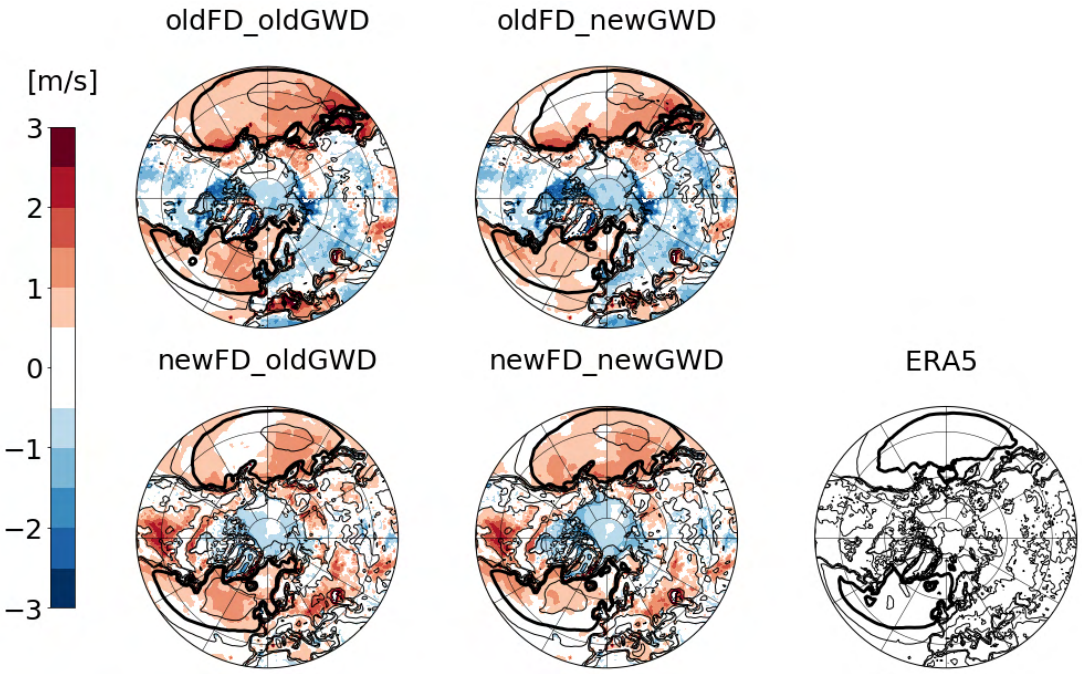

FIGURE 5.15: DJF 10 meters zonal wind. The bottom right panel displays ERA5 reanalysis data (contours) while the other panels show the result of the four experiments (contours) and the biases with respect to ERA5 (colours). The thick lines mark the 10 m/s level.

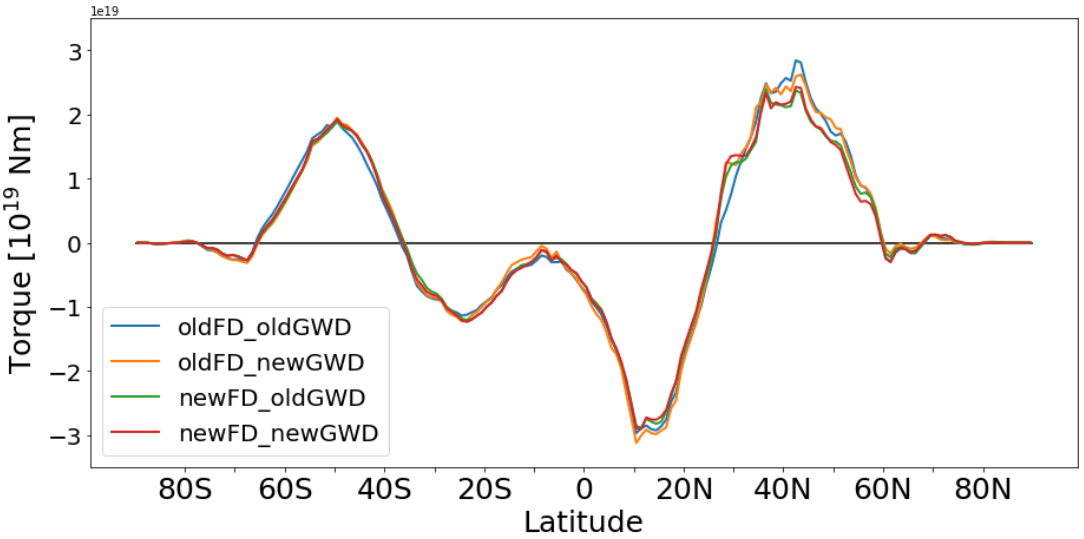

FIGURE 5.16: Total parameterized torques.

5.1.5 Effects on the circulation

We can now inspect the effects of the new parameterizations on the atmospheric circulation. Fig. 5.17 shows Mean Sea Level Pressure (MSLP) patterns and biases with respect to ERA5. The old model displays alternatively positive and negative biases located around the climatological low pressure centers over the North Pacific and North Atlantic basins (the Aleutian and Icelandic low, respectively). In fact, they are related to an incorrect representation of the structure of the MSLP stationary waves[1], as shown in Fig. 5.18. When the two new schemes are introduced, individually or at once, we can notice in general the onset of a positive MSLP error at high latitudes. The new OGWD scheme does a good job on the Atlantic and Eurasian sectors, showing the highest errors on the eastern North Pacific; on the contrary, the new FD scheme's most noticeable error is located over North Western Russia, independently on the GWD scheme used. These error patterns can be noticed also in the Stationary Wave MSLP bias maps; however, new schemes improves the overall representation of stationary waves.

We can study the effects of the parameterizations of tropospheric circulation at different levels with the aid of Fig. 5.19, showing geopotential height stationary wave pattern at 500, 200 and 100 hPa. For all the combinations of parameterizations used, we find a high similarity between geopotential height and MSLP stationary waves error patterns, indicating that the model has difficulties in reproducing the deviations from the zonal symmetry of the circulation at all levels in the troposphere. The new OGWD scheme main error is located over Pacific and North America, and its magnitude grows with altitude. At 100 hPa, the main error is co-located with the climatological Pacific stationary wave, showing that the scheme produces a too shallow stationary wave over this sector. The introduction of the new FD scheme alone produces a good result at all levels, preforming better than the old model over all sectors and at all altitudes. When the new schemes are used simultaneously, a worsening over the Euro-Atlantic sector is noticed.

We can interpret the changes in stationary waves patterns as a consequence of the changes in the mean zonal wind produced by different drag parameterizations. In fact, from the dispersion relation for barotropic Rossby waves (Holton, 2012; Vallis, 2017) it is possible to derive the equation relating the waves phase speed c, wavenumber k and the mean wind U:

$$c = U - \frac{\beta}{k^2} \tag{5.1}$$

where β is the Rossby parameter. Therefore, a modification in the zonal flow determines a change in planetary waves speed relative to the Earth surface. Moreover, modifications in the horizontal and vertical shear of the mean wind basic state can alter the waves' horizontal propagation direction (Hoskins and Karoly, 1981; Karoly, 1982) and modulate their transmission to upper atmospheric levels (Charney and Drazin, 1961).

To conclude our evaluation of the effects of the new parameterizations on the atmospheric circulation, we show in Fig. 5.20 the zonal wind at 850, 250, 100 and 10 hPa. The old model shows, at 850 and 250 hPa, an Atlantic jet which is too zonal and too intense over western and southern Europe, while it is weaker than observed over eastern Pacific. At 100 hPa the midlatitudes jet is too intense all around the Northern Hemisphere, while the structure of the stratospheric polar vortex at 10 hPa is reproduced reasonably well. Looking at the model configurations with the new schemes, we notice a common effect on the lower tropospheric jet over both the major oceanic basins: the new schemes slow down the jet on both sectors, reducing the positive bias over southwestern Europe but worsening the already negative bias over Pacific ocean. The behaviour of the different model configurations start to diverge with altitude: at

[1]Stationary waves are calculated as follows: the mean DJF MSLP has been obtained from a 10-year average, then its zonal mean has been subtracted from the same field. Thus, stationary waves represent local latitudinal deviations from the zonal mean of the climatological field.

100 hPa, the new OGWD scheme produce an unrealistically slow Atlantic jet, and at 10 hPa the structure of the stratospheric polar vortex is misrepresented, with too intense zonal winds over the North Pacific - North American sector at approximately 40°N but a slower than observed vortex at higher latitudes. On the contrary, with the new FD scheme, at 100 and 10 hPa we obtain results similar to what we obtain with the old model. This behaviour is consistent with what we said in the previous paragraphs: both schemes act on lower troposphere winds, simulating different aspects of its interaction with unresolved orography; however, only the OGWD scheme can directly influence the upper atmosphere. Moreover, when the two schemes are used together (fourth row in Fig. 5.20) the general effects on the lower troposphere are the same, while in the upper troposphere and stratosphere the strong footprint of the new OGWD scheme disappears, confirming the modulating role of the new FD scheme on the tendencies produced by the OGWD parameterizations.

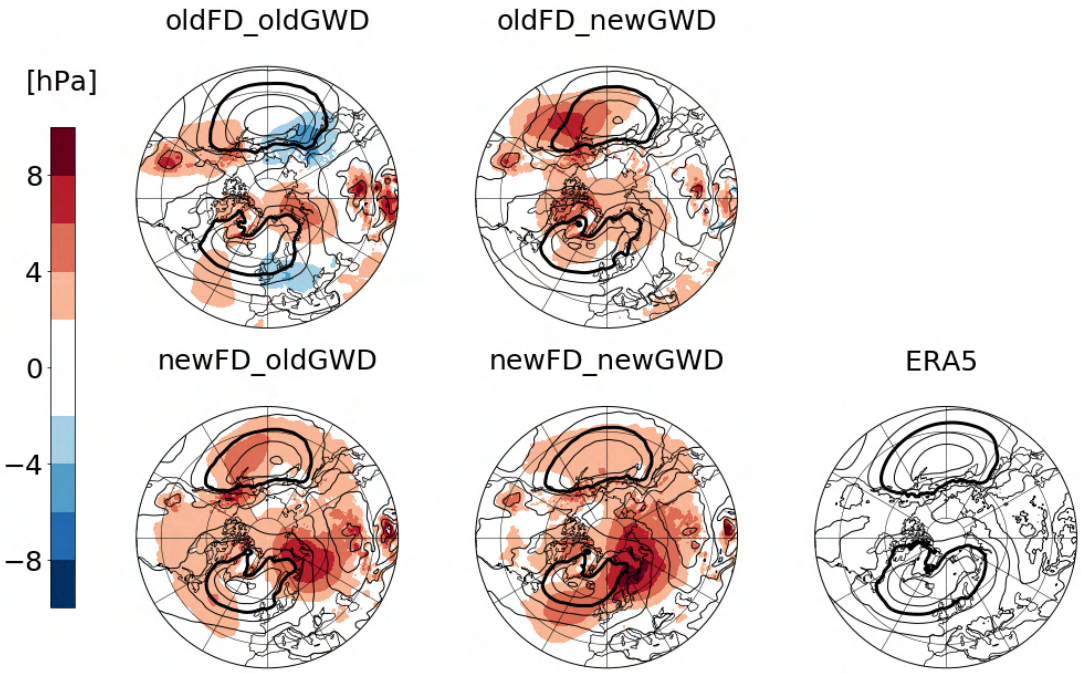

FIGURE 5.17: DJF Mean Sea Level Pressure. The bottom right panel displays ERA5 reanalysis data (contours) while the other panels show the result of the four experiments (contours) and the biases with respect to ERA5 (colours). The thick lines mark the 1010 hPa level.

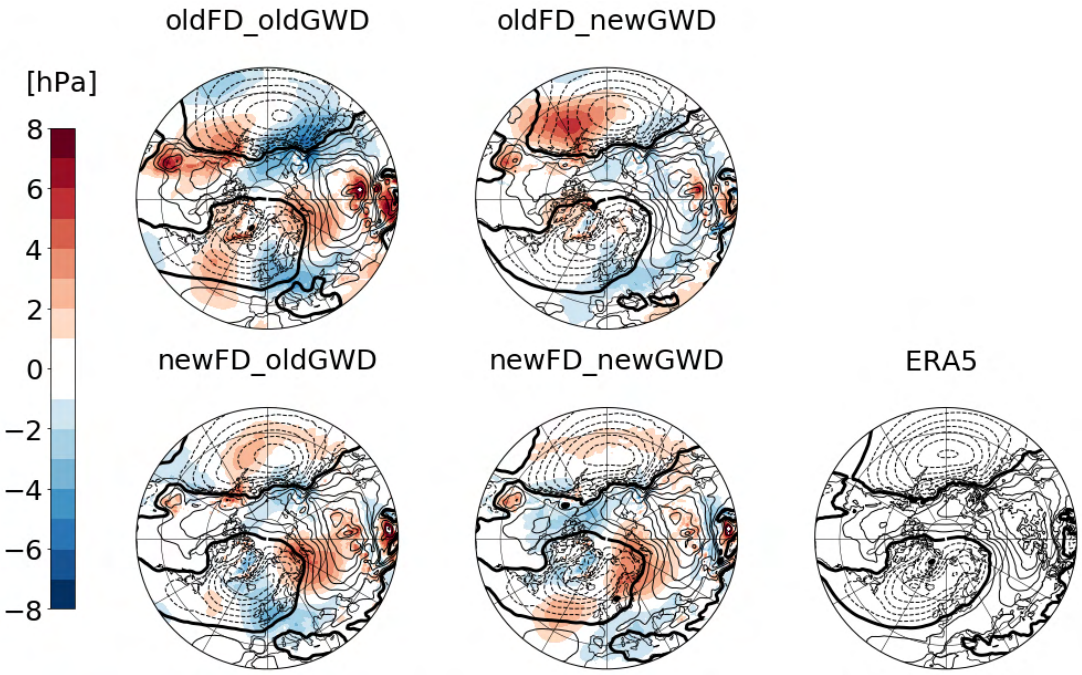

FIGURE 5.18: DJF Mean Sea Level Pressure Stationary Waves. The bottom right panel displays ERA5 reanalysis data (contours) while the other panels show the result of the four experiments (contours) and the biases with respect to ERA5 (colours). The thick lines mark the 0 hPa level.

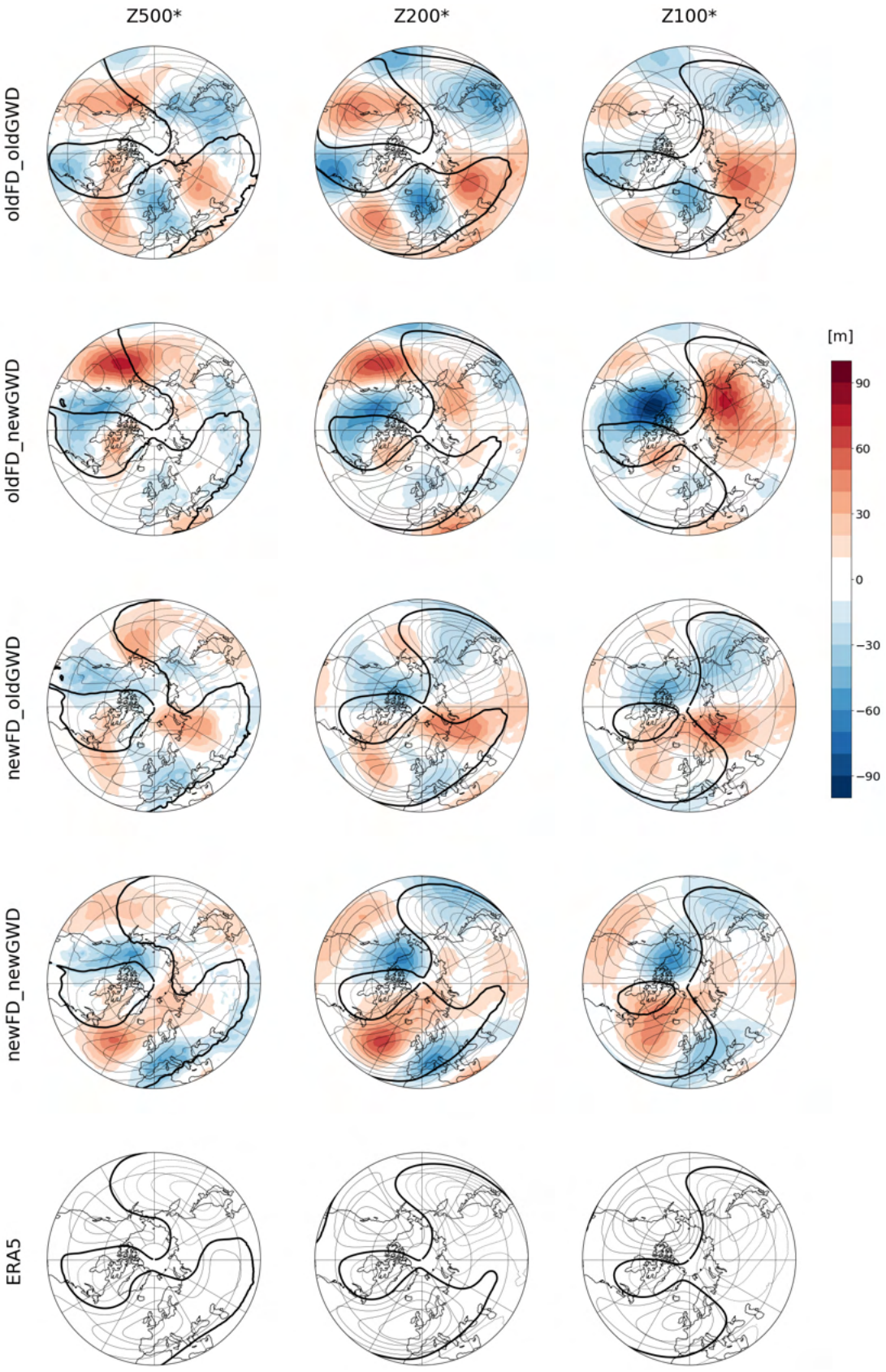

FIGURE 5.19: DJF geopotential height stationary waves at (from left to right) 500, 200, 100 hPa. The bottom row displays ERA5 reanalysis data (contours) while the other panels show the result of the four experiments (contours) and the biases with respect to ERA5 (colours). The thick lines mark the 0 m level.

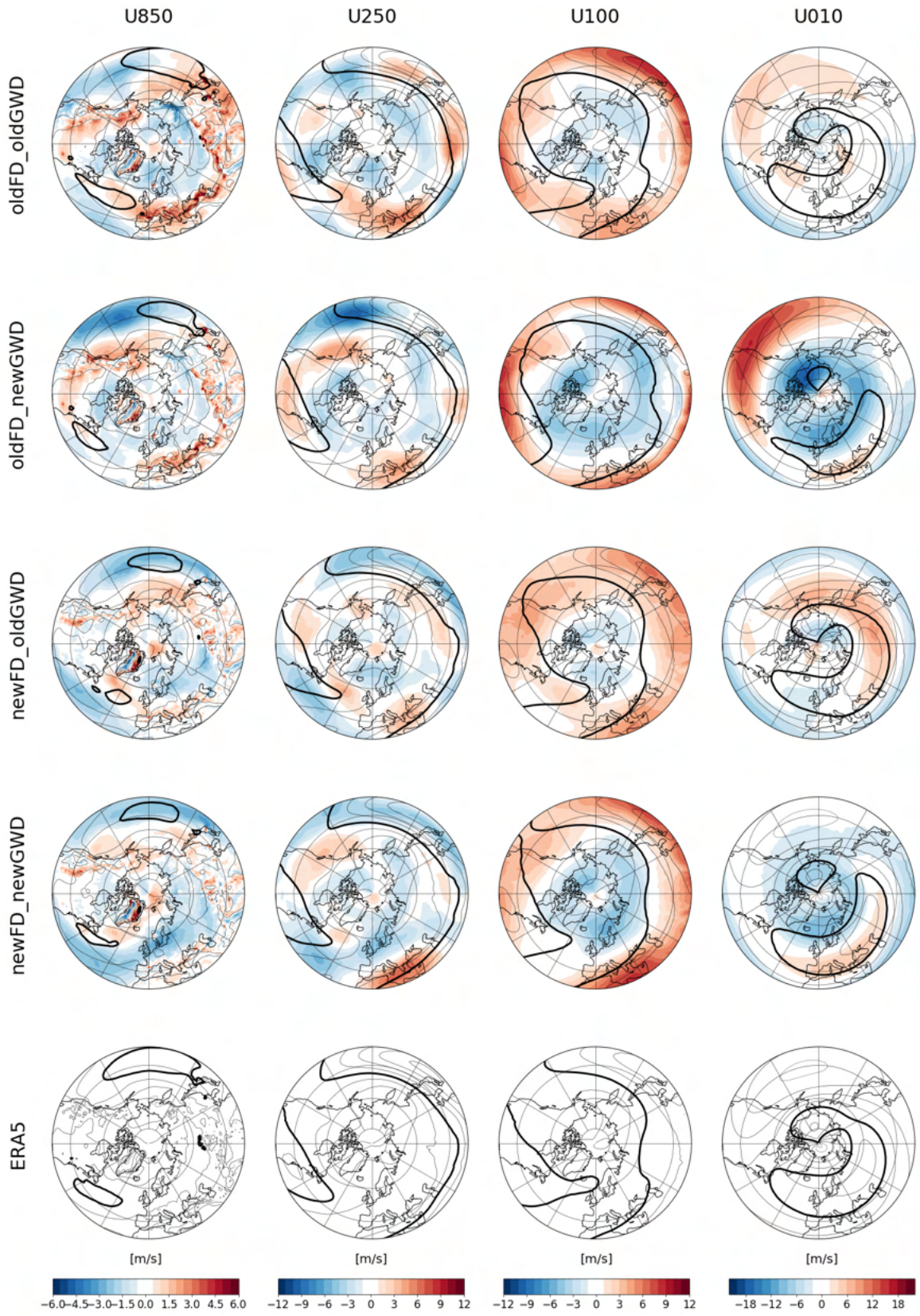

FIGURE 5.20: DJF zonal wind at (from left to right) 850, 250, 100, 10 hPa. The bottom row displays ERA5 reanalysis data (contours) while the other panels show the result of the four experiments (contours) and the biases with respect to ERA5 (colours). The thick lines mark, in each row from left to right, the 10, 30, 20, 30 m/s levels.

5.2 Perturbation of the new Form Drag scheme

We start examining the sensitivity of the model to the values of some fundamental parameters of the schemes. We begin with the new FD scheme. As explained in section 3.6.2, the formula used in the scheme to calulate the form drag profile due to subgrid orography is given by eq. 3.24. Here, the whole profile is multiplicated by four constant numerical factors (namely, $\alpha, \beta, C_{md}, C_{corr}$). Their physical interpretation and the choice of their specific values is discussed by the authors in their original paper (Beljaars, Brown, and Wood, 2004). The first two factors, α and β, are taken from a previously published analytical model (Wood and Mason, 1993) where they were considered as (weakly) dependent on the shape of the orography, while in this scheme are taken as constant. C_{md} derives from the (reasonable) assumption of a logarithmic vertical profile for the unperturbed flow, and its value is again fixed to a constant. C_{corr} is introduced to adjust the behaviour of the scheme after some simplifying assumptions, needed to make the implementation of the new scheme in a NWP/climate model computationally feasible.

Therefore, the product of these uncertain parameters results in an uncertain modulation of the whole drag profile. To explore the model sensitivity to this modulation, we decided to consider the parameter α (any of the other three parameters would be suitable for this purpose), whose standard value is 12, and to perturb it increasing and decreasing it by 50% (so $\alpha = 18$ and $\alpha = 6$, respectively). In the following, we compare the results obtained with the old model, with both the new parameterizations in the standard configuration, and with both the new schemes with the two perturbed values of the FD scheme parameters. In Table 5.2 the different parameterization settings are summarized.

When the drag produced by the FD scheme is reduced, MSLP positive bias over NH high latitudes is also reduced, while an increased form drag leads to a general increase in MSLP positive bias. Interestingly, this kind of response was observed also by other authors working on form drag and low-level flow blocking parameterizations (Zadra et al., 2003; Sandu, Bechtold, and Beljaars, 2016) and it can be understood in terms of geostrophic balance: the decreased (increased) meridional pressure gradient corresponds to a deceleration (acceleration) of surface westerly winds due to increased (decreased) surface orographic drag. Looking at the deviations from the zonal mean, all three new model configurations lead to an improvement with respect to the old model; the main differences between the three FD scheme configurations are found over the North Atlantic and Eurasian sectors.

The "low FD" configuration is the better in terms of error on the geopotential height stationary wave pattern, where it outperforms all the other model configurations over the whole NH at all levels. In the "high FD" configuration the model stationary wave bias worsen with altitude, as a consequence of the FD scheme indirect effect on the OGWD parameterized tendencies.

When the FD is decreased, throughout the whole troposphere the jet strengthens over the north Pacific and weakens over North Atlantic, while the opposite happens if FD is increased. At 10 hPa, the indirect effect of the FD scheme on OGWD tendencies produces a stronger-than-observed polar jet when FD is increased, and a vortex deceleration when FD is decreased.

Experiment name	α	Period
oldFD_oldGWD	-	1/1/1993 - 31/12/2002
newFD-alpha6_newGWD	6	1/1/1993 - 31/12/2002
newFD_newGWD	12	1/1/1993 - 31/12/2002
newFD-alpha18_newGWD	18	1/1/1993 - 31/12/2002

TABLE 5.2: Summary of the second set of experiments. The model is run for 10 years. When used with the new parameterization, the value of the parameter α, modulating the FD scheme stress profile, is systematically varied. Any other parameter is left untouched. Since α is not present in the old FD scheme, its value is not indicated for the oldFD_oldGWD experiment.

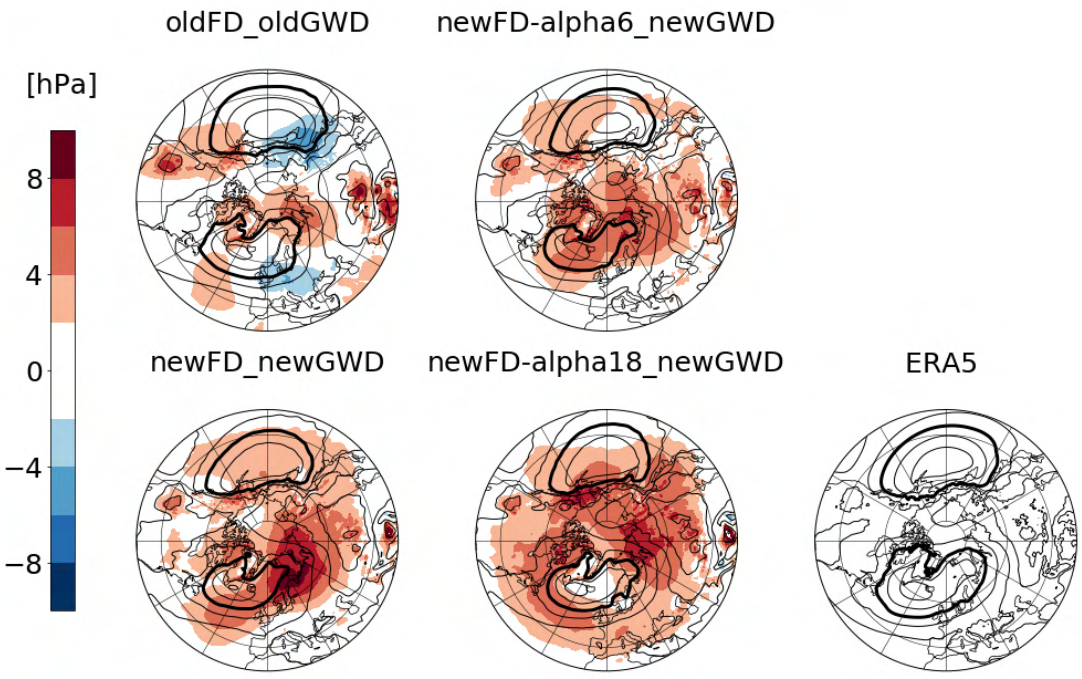

FIGURE 5.21: DJF Mean Sea Level Pressure. The bottom right panel displays ERA5 reanalysis data (contours) while the other panels show the result of the four experiments (contours) and the biases with respect to ERA5 (colours). The thick lines mark the 1010 hPa level.

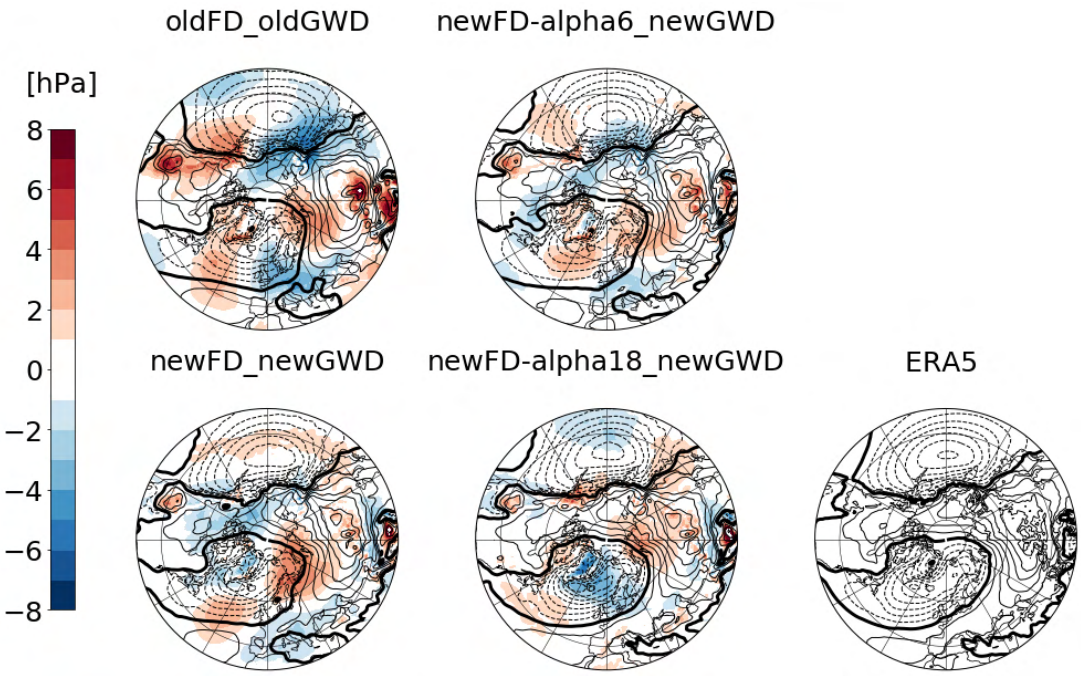

FIGURE 5.22: DJF Mean Sea Level Pressure Stationary Waves. The bottom right panel displays ERA5 reanalysis data (contours) while the other panels show the result of the four experiments (contours) and the biases with respect to ERA5 (colours). The thick lines mark the 0 hPa level.

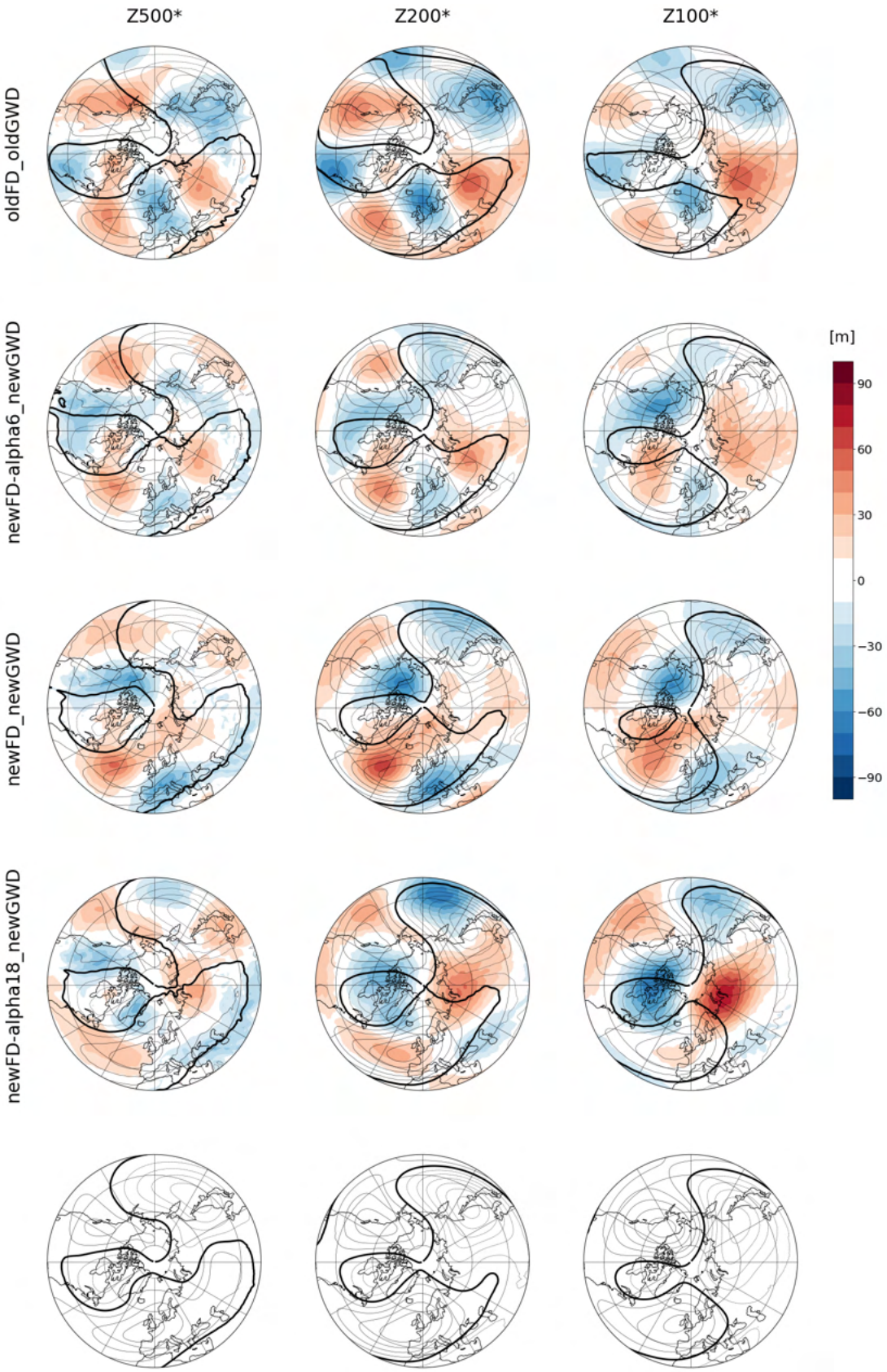

FIGURE 5.23: DJF geopotential height stationary waves at (from left to right) 500, 200, 100 hPa. The bottom row displays ERA5 reanalysis data (contours) while the other panels show the result of the four experiments (contours) and the biases with respect to ERA5 (colours). The thick lines mark the 0 m level.

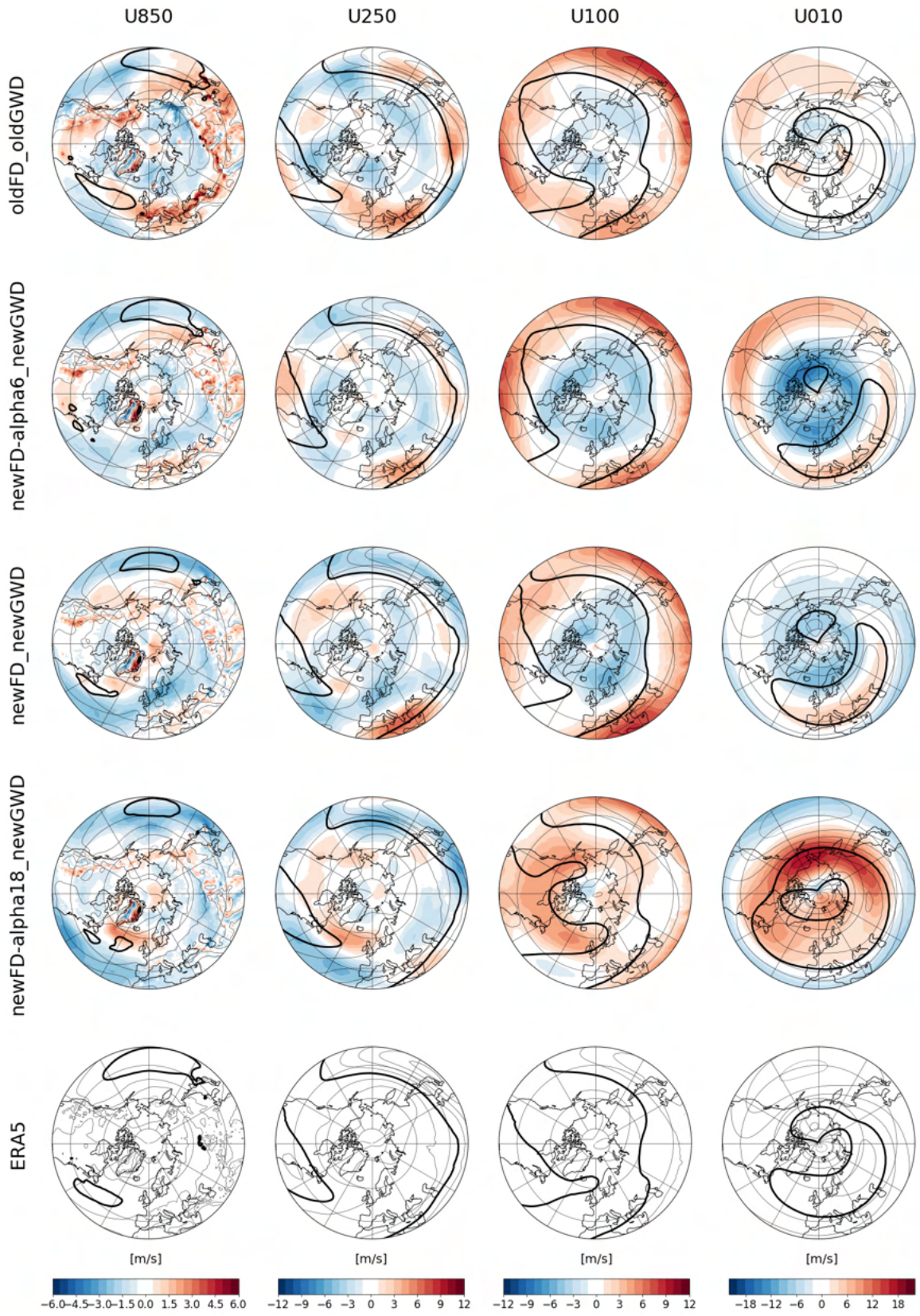

FIGURE 5.24: DJF zonal wind at (from left to right) 850, 250, 100, 10 hPa. The bottom row displays ERA5 reanalysis data (contours) while the other panels show the result of the four experiments (contours) and the biases with respect to ERA5 (colours). The thick lines mark, in each row from left to right, the 10, 30, 20, 30 m/s levels.

5.3 Perturbation of the new Orographic Gravity Wave Drag scheme

The second parameter we decided to perturb, in order to test the model sensitivity to its value, is the $effgw\_rdg$ factor in equation 3.57. This number influence the final efficiency factor for gravity waves, calculated by the scheme taking into account grid box area and unresolved ridges length and width, that is passed to the routine which calculates the wind tendency profile scanning all model levels from the surface toward model top (see section 3.6.3). $effgw\_rdg$ can be tought as crudely representing the spatial and temporal intermittency of the various orographic phenomena represented by the scheme (generation of gravity waves, low level wave breaking, flow blocking) on timescales smaller than the model physical timestep; its direct effect is to regulate the conversion from the drag profile to the tendency profile, and it can be seen as a model tuning parameter, since we can not easily deduce its value from prime principles or observations. The standard value for $effgw\_rdg$ is 1; we decided to run two additional experiments with $effgw\_rdg$ set to 0.5 and 1.5. The parameterization settings used in the different experiments are shown in Table 5.3.

An increased $effgw\_rdg$ causes increased drag force and parmeterized wind tendencies from the surface up to the stratosphere (not shown) and, similarly to an increased form drag, causes a positive MSLP bias over NH high latitudes, which tend to disappear when $effgw\_rdg$ is reduced.

The stationary waves response to the modified drag can be summarized as follows. With respect to the unperturbed condition, lowering $effgw\_rdg$ improves the climatological bias over the Euro-Atlantic sector. At the contrary, an opposite variation of $effgw\_rdg$ causes a deterioration of the structure of geopotential height stationary waves over the same sector, while some improvements can be noticed over the north Pacifc ocean.

A consistent picture emerge from the inspection of zonal wind plots: increasing the drag, the pacific jet intensity increases, throughout the whole troposphere. On the contrary, the Atlantic jet is less intense and changes orientation, becoming more zonal (that is, pointing toward southern instead of northern Europe) with increased drag. At 10 hPa, less efficiency in producing (easterly) wind tendencies causes an acceleration of the polar vortex and vice versa.

Experiment name	$effgw\_rdg$	**Period**
oldFD_oldGWD	-	1/1/1993 - 31/12/2002
newFD_newGWD-effgw0.5	0.5	1/1/1993 - 31/12/2002
newFD_newGWD	1.0	1/1/1993 - 31/12/2002
newFD_newGWD-effgw1.5	1.5	1/1/1993 - 31/12/2002

TABLE 5.3: Summary of the third set of experiments. The model is run for 10 years. When used with the new parameterization, the value of the parameter $effgw_rdg$, modulating the OGWD scheme tendency profile, is systematically varied. Any other parameter is left untouched. Since $effgw$ is not present in the old OGWD scheme, its value is not indicated for the oldFD_oldGWD experiment.

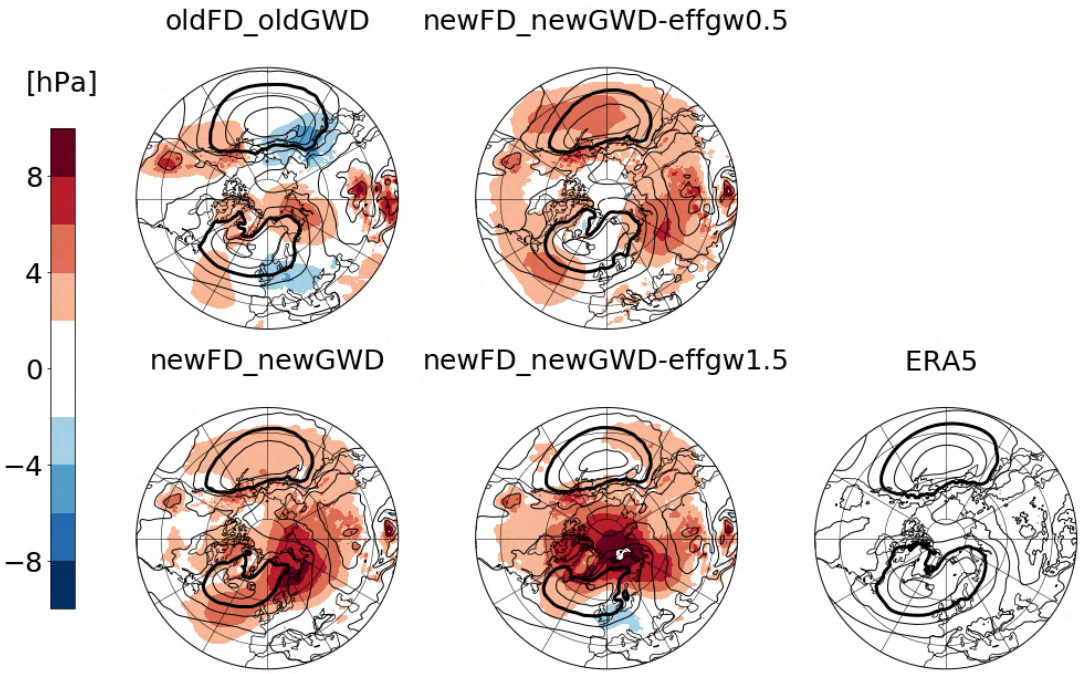

FIGURE 5.25: DJF Mean Sea Level Pressure. The bottom right panel displays ERA5 reanalysis data (contours) while the other panels show the result of the four experiments (contours) and the biases with respect to ERA5 (colours). The thick lines mark the 1010 hPa level.

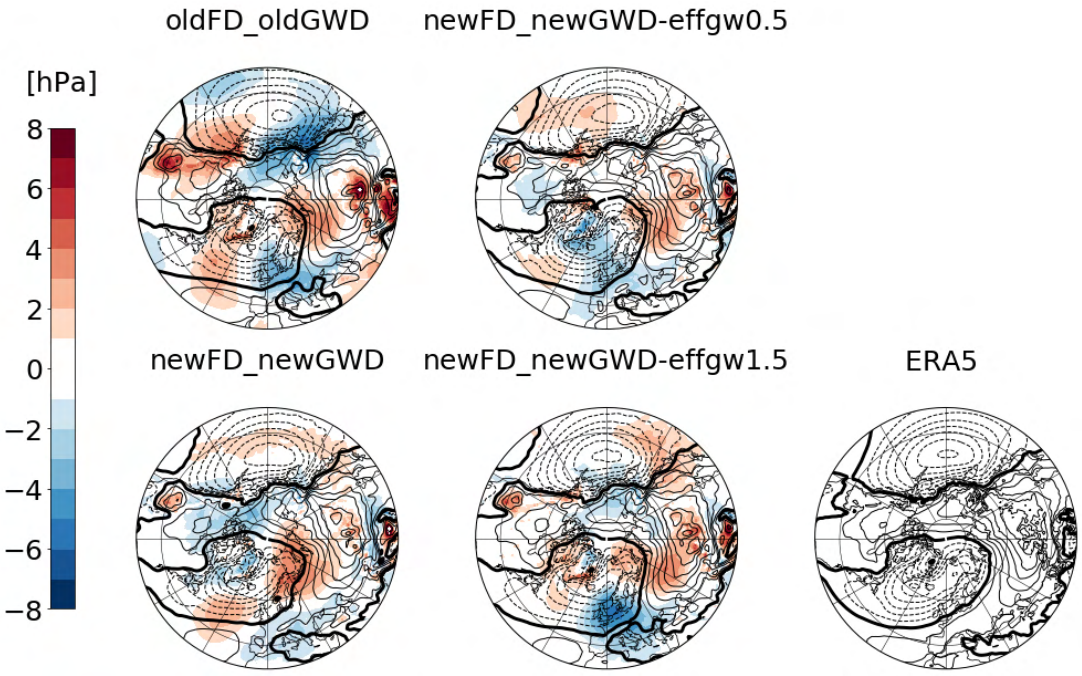

FIGURE 5.26: DJF Mean Sea Level Pressure Stationary Waves. The bottom right panel displays ERA5 reanalysis data (contours) while the other panels show the result of the four experiments (contours) and the biases with respect to ERA5 (colours). The thick lines mark the 0 hPa level.

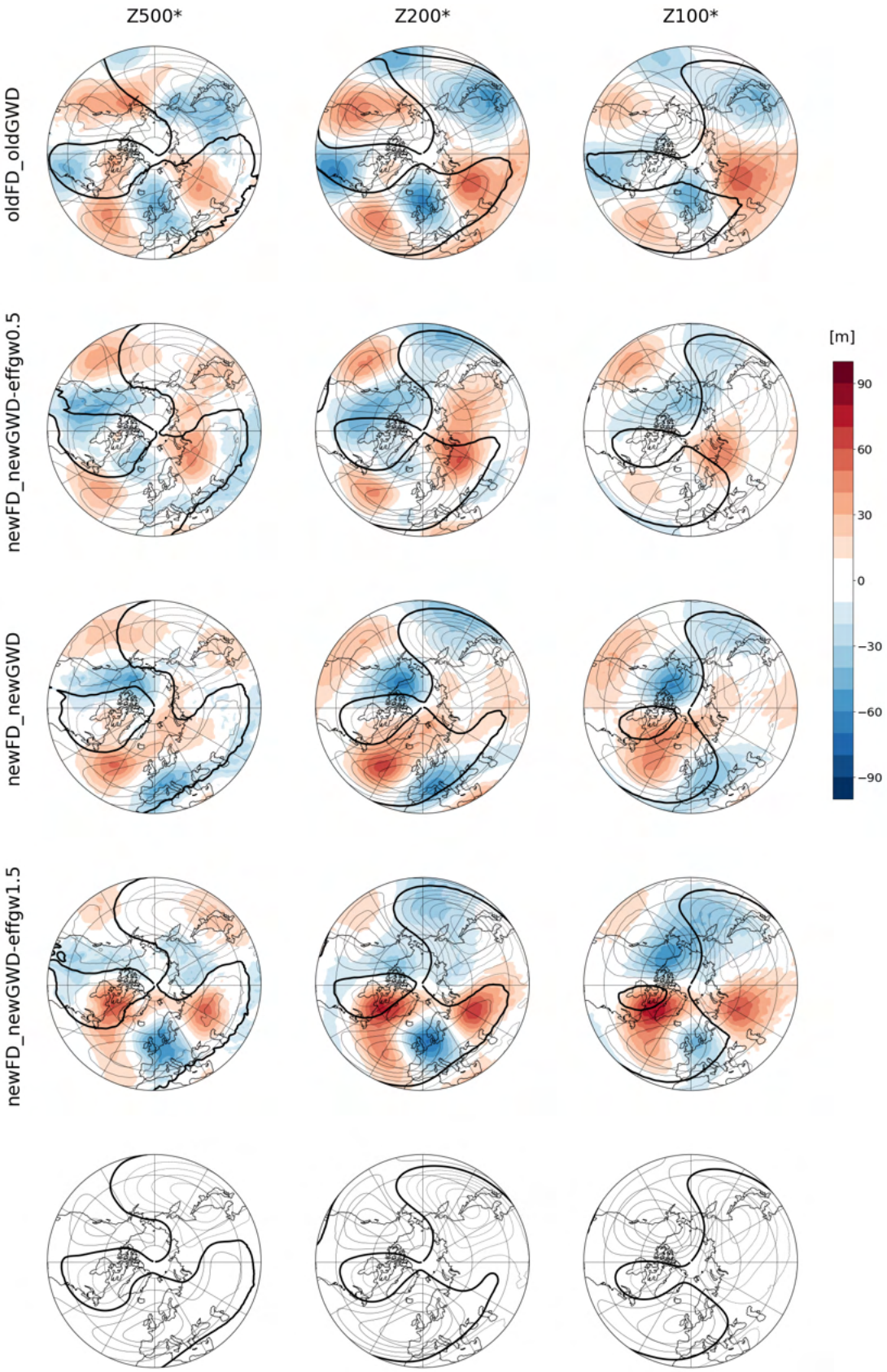

FIGURE 5.27: DJF geopotential height stationary waves at (from left to right) 500, 200, 100 hPa. The bottom row displays ERA5 reanalysis data (contours) while the other panels show the result of the four experiments (contours) and the biases with respect to ERA5 (colours). The thick lines mark the 0 m level.

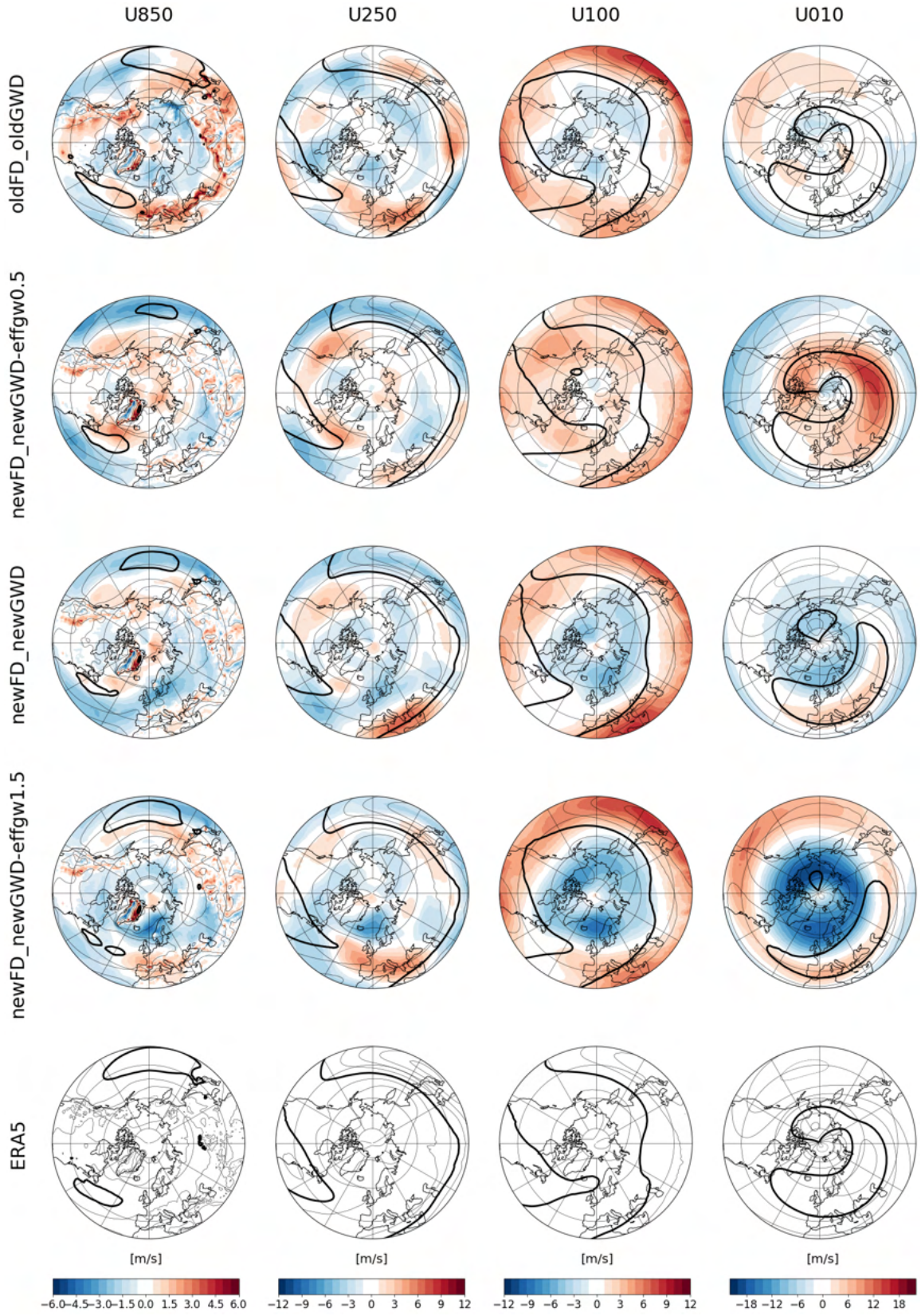

FIGURE 5.28: DJF zonal wind at (from left to right) 850, 250, 100, 10 hPa. The bottom row displays ERA5 reanalysis data (contours) while the other panels show the result of the four experiments (contours) and the biases with respect to ERA5 (colours). The thick lines mark, in each row from left to right, the 10, 30, 20, 30 m/s levels.

5.4 Perturbation of both FD and OGWD schemes

We can summarize the findings of the previous sections (general properties and perturbation of FD and OGWD schemes) as follows.

- in general, new drag schemes produce a deceleration of low-level winds which, in turn, determine the onset of a positive MSLP bias over the North Pole, due tue a geostrophic response to the decreased surface winds (Zadra et al., 2003; Sandu, Bechtold, and Beljaars, 2016). The drag produced by the schemes can be regulated by some fundamental parameters, and their values determine sistematic changes in the aforementioned effects.
- the two schemes simulate two aspects of the complicated interaction between unresolved orography and the atmospheric flow; their formulations are such that they both strongly depends on the same input variable (resolved wind), which in turn is the same variable they act on. Therefore, they are intrinsically interconnected and they can influence each other non-linearly. In particular, we showed that, for a given OGWD efficiency, the FD scheme modulate the low-level wind near unresolved orography, influencing flow blocking and the production of GWs and, in turn, easterly momentum deposition both close to the orography and at higher altitudes; secondly, the OGWD efficiency parameter modulates the wind tendency all over the atmospheric column, shaping the resolved wind vertical profile and indirectly influencing the FD scheme.
- the high latitudes positive MSLP bias can be reduced lowering the FD scheme parameterized drag; lower FD leads also to a stronger tropospheric zonal wind jet over the Pacific basin and a weaker jet over the Atlantic. The stratospheric polar jet at 10 hPa is weakened as a result of an increased production of GWs at surface which deposit easterly momentum here. Opposite effects are observed if FD is increased.
- a very similar behavior is observed changing the GW efficiency parameter, however with an opposite relation with the sign of the perturbation. The same kind of response in jet strength, both in the troposphere and in stratosphere, described in the previous point is obtained increasing the GW efficiency; additionally, we also observed a zonalization of the NA jet increasing GW efficiency.

Up to now, we analyzed the model response to the variation of two uncertain orographic parameters, modified one at a time. In the second part of this analysis, we want to assess the model sensitivity to the perturbation of the whole "unresolved orography parameterization package", since both schemes contains uncertainties and errors. To do so, we want to run simulations where we vary at the same time the values of both α and $effgw\_rdg$. In this way we can simulate a range of possible orographic settings the model could be run with (since we have no conclusive clues from theory or observations) and, in the last part of the thesis, study how this simulated spread in orographic parameters (which reflect our ignorance on their most appropriate values) affect the simulation of important atmospheric processes in Northern Hemisphere midlatitudes.

Relying on the results of the previous sections, we can build some physically interesting model configurations, with the aim of creating a small ensemble of model runs usable to investigate how uncertainty on and errors in orographic parameterizations can affect atmospheric circulation. As we shown, lowering FD has very similar effects of increasing OGWD efficiency and vice versa. Therefore, it is reasonable to think that a model run with both low FD and high OGWD efficiency would lead to an amplification of their individual effects, in particular an excessive generation of gravity waves at the surface and an excessive momentum deposition in the stratosphere, leading to an unrealistic simulation, too far from observations to be of practical utility. The same can be said for a model run with increased FD and lower OGWD efficiency,

Experiment name	α	$effgw\_rdg$	**Period**
oldFD_oldGWD	-	-	1/1/1993 - 31/12/2002
newFD_newGWD_lowdrag	6	0.5	1/1/1993 - 31/12/2002
newFD_newGWD	12	1.0	1/1/1993 - 31/12/2002
newFD_newGWD_highdrag	18	1.5	1/1/1993 - 31/12/2002

TABLE 5.4: Summary of the fourth set of experiments. The model is run for 10 years. When used with the new parameterization, the value of two fundamental parameters are systematically varied at the same time in both schemes. α modulates the FD scheme stress profile, $effgw\_rdg$ modulates the OGWD tendency profile. Since these parameters are not present in the old schemes, their values are not indicated for the oldFD_oldGWD experiment.

where we believe to observe too little momentum deposition by GW in the stratosphere. As a consequence, we believe that interesting (in terms of effects on midlatitude circulation) combinations of parameters perturbation can be obtained lowering and increasing both the FD and the OGWD efficiency at the same time. Moreover, these two configurations represent a decrease and an increase in the total parameterized orographic drag. We run a "low drag" configuration with $\alpha = 6$ and $effgw\_rdg = 0.5$ and a "high drag" configuration with $\alpha = 18$ and $effgw\_rdg = 1.5$. The standard configuration with $\alpha = 12$ and $effgw\_rdg = 1.0$ represent the unperturbed condition. Of course, the choice of dividing and multiplying by a factor of 2 the considered parameters is quite crude, and it not represent an attempt of fine-tuning our model: our goal is to explore how uncertainty on these unconstrained parameters can affect model circulation and processes simulation in midlatitudes. The experiments settings are summarized in Table 5.4.

The results obtained are shown in the following figures, relative to 10 years integrations. In the next sections, the same model configurations are run for 39 years, in order to draw more robust conclusions. Regarding MSLP (Fig. 5.30), we obtained the same behaviour observed in previous sections, that is a tendency to develop a positive bias over polar regions increasing the total orographic drag. The overall bias in MSLP and geopotential height stationary waves is improved using new parameterizations, independently on the particular values used for the parameters (Fig. 5.30 and Fig. 5.31). A strong difference between the simulations is found in lower tropospheric zonal wind over the Atlantic sector (Fig. 5.32). Lowering the drag of the new parameterizations pushes the model mean state towards what we obtained with the old schemes. The 850 hPa Atlantic jet increases its intensity, causing a westerly bias over southwestern Europe. A band of westerly error extends from east Asia, downwind of the Himalaya, to the North American Great plains, passing through the North Pacific Ocean, very similarly to what observed with the old model. A tendency to reproduce the old model error pattern can be noticed also at higher levels. On the contrary, increasing the drag the NA 850 hPa jet weakens, and negative (easterly) zonal wind biases develops also over the great majority of continents. Over the Pacific Ocean, the low level jet remains weaker than observed, however we can notice a shift to the east of its core going from lower to higher drag settings. The influence of the drag settings on the stratospheric jet is limited (Fig. 5.32); we believe that the reason is the compensating effect between FD and OGWD efficiency discussed before.

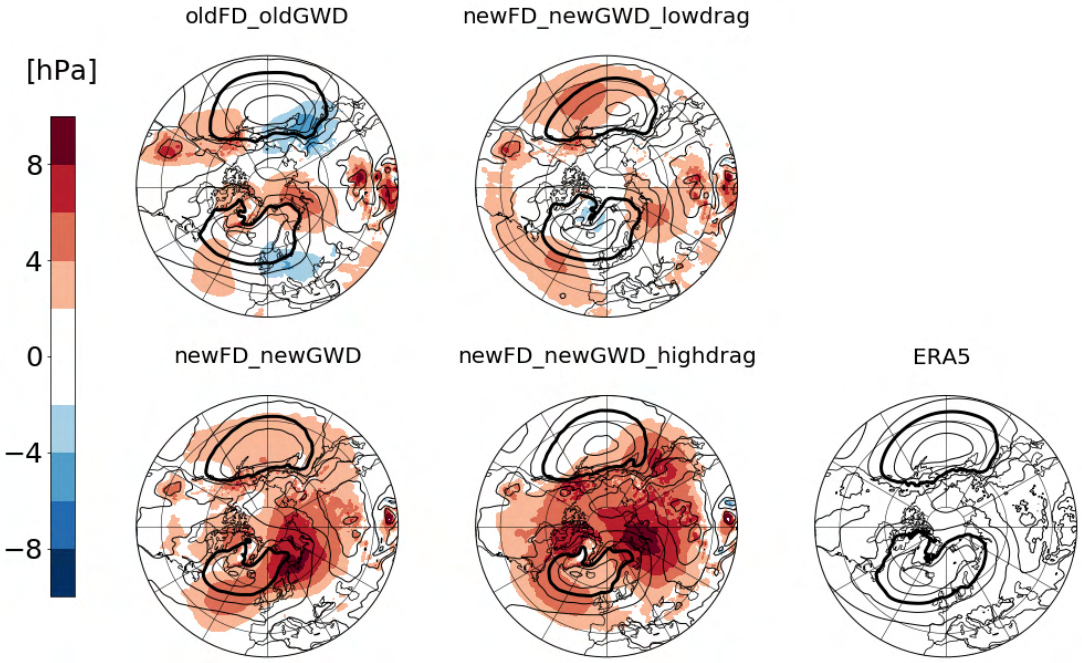

FIGURE 5.29: DJF Mean Sea Level Pressure. The bottom right panel displays ERA5 reanalysis data (contours) while the other panels show the result of the four experiments (contours) and the biases with respect to ERA5 (colours). The thick lines mark the 1010 hPa level.

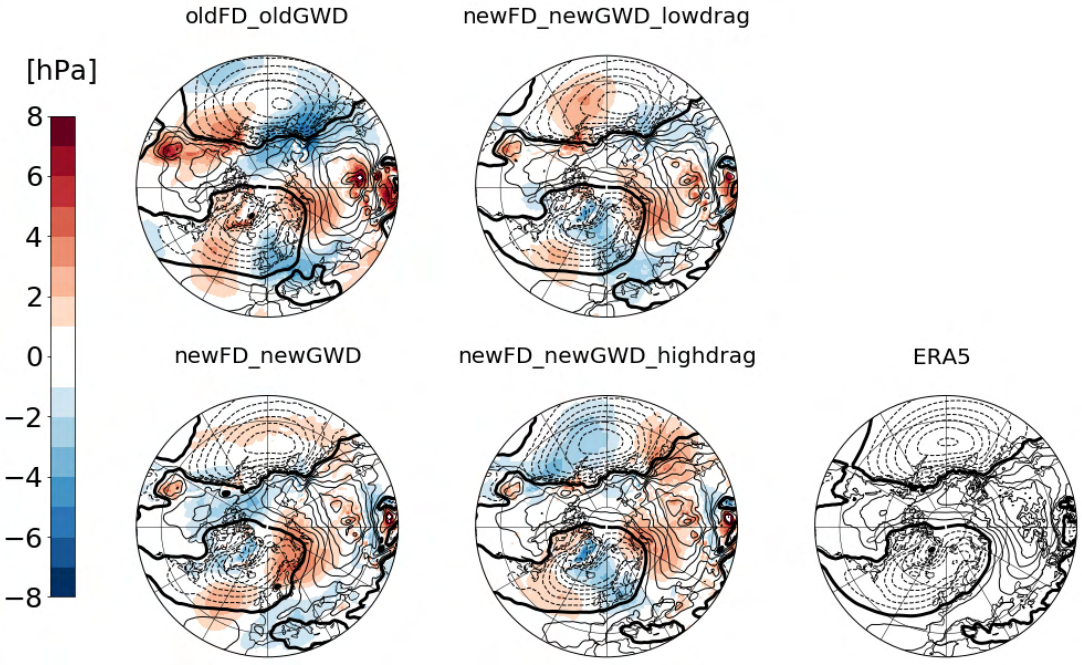

FIGURE 5.30: DJF Mean Sea Level Pressure Stationary Waves. The bottom right panel displays ERA5 reanalysis data (contours) while the other panels show the result of the four experiments (contours) and the biases with respect to ERA5 (colours). The thick lines mark the 0 hPa level.

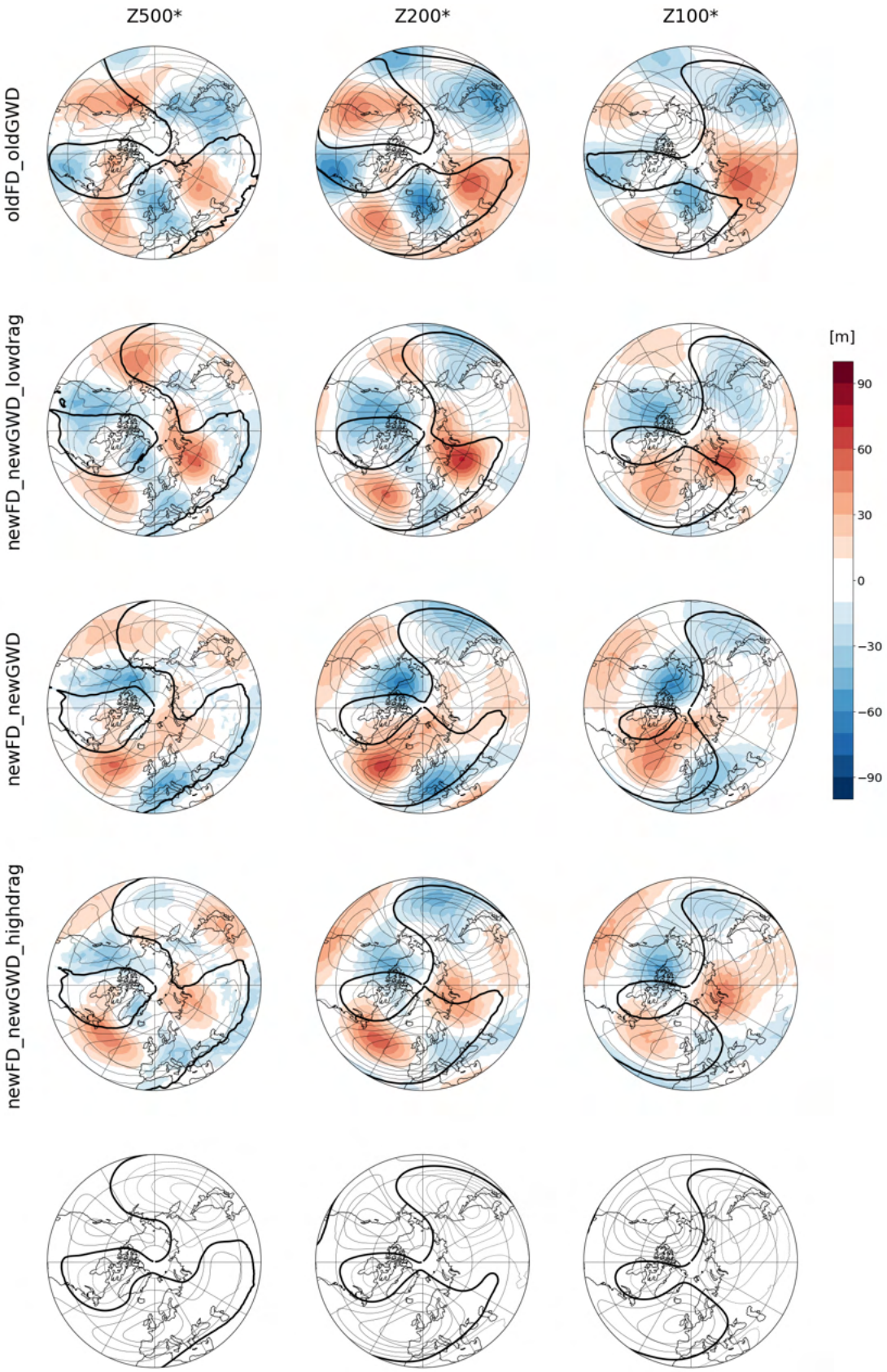

FIGURE 5.31: DJF geopotential height stationary waves at (from left to right) 500, 200, 100 hPa. The bottom row displays ERA5 reanalysis data (contours) while the other panels show the result of the four experiments (contours) and the biases with respect to ERA5 (colours). The thick lines mark the 0 m level.

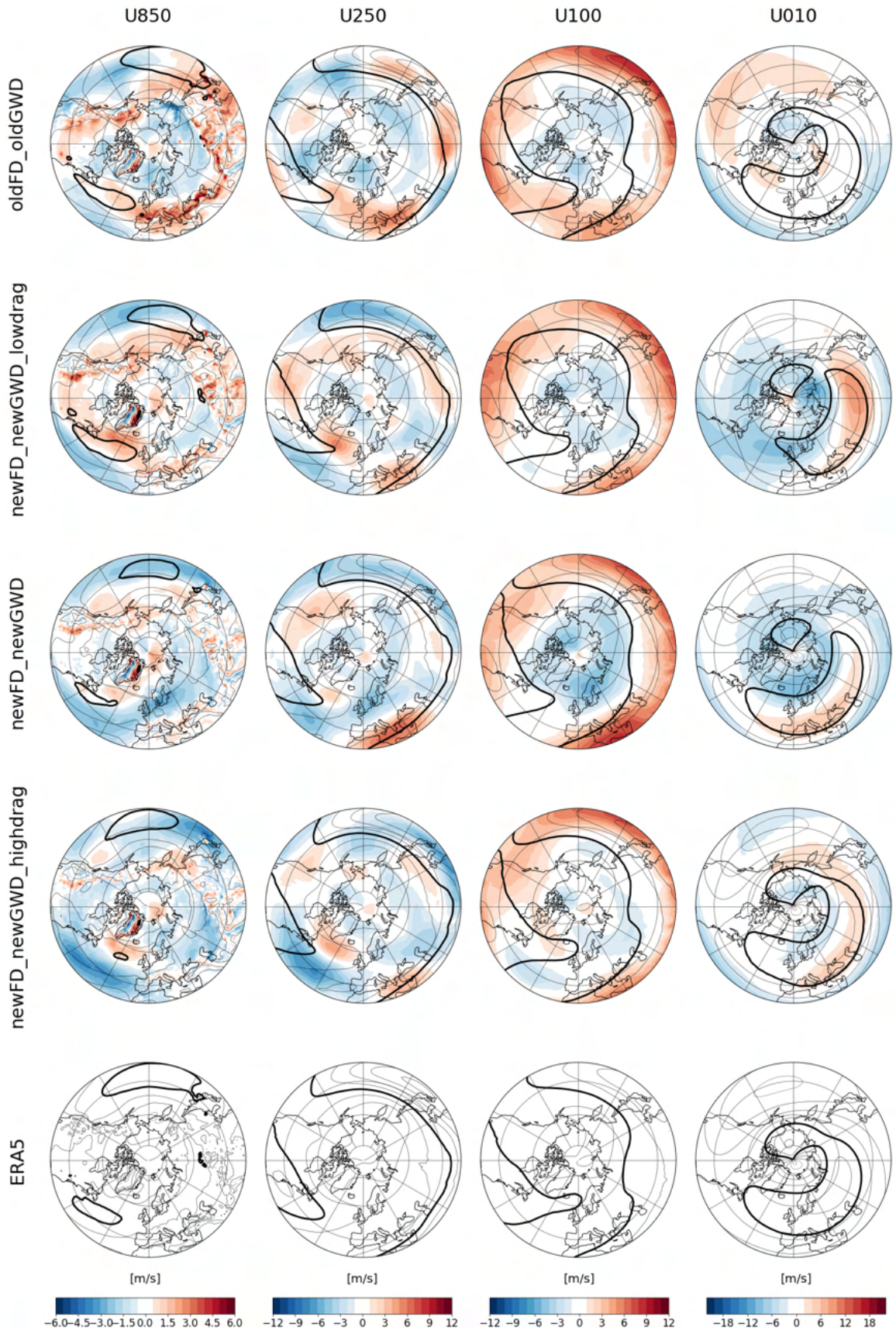

FIGURE 5.32: DJF zonal wind at (from left to right) 850, 250, 100, 10 hPa. The bottom row displays ERA5 reanalysis data (contours) while the other panels show the result of the four experiments (contours) and the biases with respect to ERA5 (colours). The thick lines mark, in each row from left to right, the 10, 30, 20, 30 m/s levels.

5.5 The impact of the new schemes on the modeling of atmospheric processes

In the last set of experiments we run the model with the settings presented in the previous section (that is both old schemes, and both new schemes with standard, "low drag" and "high drag" settings) for a period of 39 years, from 1/1/1979 to 31/12/2017. As before, the model is forced with observed SSTs. In this way we can compare our simulations with ERA5 renalysis and study how orographic parameters affect the modeling of specific atmospheric processes. The details on this last set of experiments are shown in Table 5.5.

Experiment name	α	$effgw\_rdg$	**Period**
oldFD_oldGWD	-	-	1/1/1979 - 31/12/2017
newFD_newGWD_lowdrag	6	0.5	1/1/1979 - 31/12/2017
newFD_newGWD	12	1.0	1/1/1979 - 31/12/2017
newFD_newGWD_highdrag	18	1.5	1/1/1979 - 31/12/2017

TABLE 5.5: Summary of the final set of experiments. The model is run for 39 years. When used with the new parameterization, the value of two fundamental parameters are systematically varied at the same time in both schemes. α modulates the FD scheme stress profile, $effgw\_rdg$ modulates the OGWD tendency profile. Since these parameters are not present in the old schemes, their values are not indicated for the oldFD_oldGWD experiment.

5.5.1 Storm Tracks

Storm tracks are diagnosed filtering daily 500 hPa geopotential height data, retaining variability under 6 days. The standard deviation of the high-pass filtered geopotential height is taken as a measure of storm track activity (see chapter 4). The old model shows two different kind of biases over the two main oceanic basins. Over the Pacific Ocean the storm track core has the right intensity and orientation, however an excess of activity is found on its northern flank and over the North American west coast. On the other hand, the North Atlantic storm track shows less activity than observed over the ocean, but its excessively zonal orientation causes an excess of activity over Southwestern Europe. The introduction of the new schemes, and the modification of their fundamental parameters, have significant impacts on the storm tracks structure. The North Pacific storm track is well represented in all model configuration with the new schemes; however, we can notice some systematic effects changing the drag. In particular, the storm track activity becomes systematically less intense over its western flank (eastern Asia, Japan, western Pacific Ocean) increasing the orographic drag, and the whole storm track is shifted longitudinally towards North-Eastern Pacific, where it develops a positive bias. A stronger response can be seen over the Euro-Atlantic sector. In the low drag configuration, the error pattern resemble the old model one, in particular over Southwestern Europe; increasing the drag, the storm track activity over eastern Atlantic and Europe decreases, and negative activity biases develops over continents (Eastern North America and Asia).

5.5.2 North Atlantic Jet Latitude and Speed

Due to the large sensitivity of the North Atlantic storm track structure to the value of the orographic parameters, and because of the large response of lower troposphere North Atlantic zonal wind to the same parameters (see section 5.4), we decided to study the structure

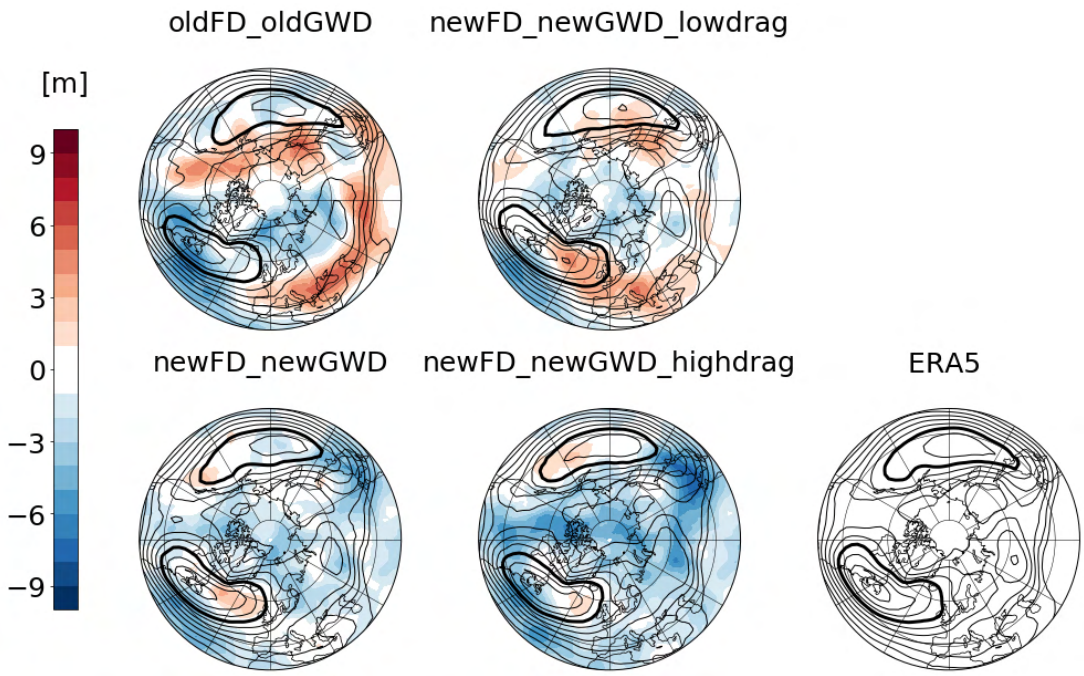

FIGURE 5.33: DJF storm tracks activity quantified calculating the 500 hPa geopotential height high frequency (<6 days) standard deviation. The bottom right panel displays ERA5 reanalysis data (contours) while the other panels show the result of the four experiments (contours) and the biases with respect to ERA5 (colours). The thick line marks the 50 m geopotential height standard deviation.

of the eddy-driven North Atlantic jet stream, using the zonal wind at 850 hPa as input for three different diagnostics. The latitudinal variability of the North Atlantic low-level jet has been studied by Woollings, Hannachi, and Hoskins, 2010, who highlighted the threemodality of the frequency distribution of the jet latitude. They proposed to use the Jet Latitude Index (JLI, see chapter 4) as a diagnostic to capture and describe this variability. A subsequent study (Madonna et al., 2017) clarified the connection between the three preferred jet locations found using the JLI framework and the four North Atlantic-European weather regimes usually found using clustering methods. The three jet positions (southern, central, northern) are connected with the o called Greenland Anticyclone, Zonal and Atlantic Ridge regimes, while the European-Scandinavian blocking regime is not well captured by the JLI, since it is associated with a strongly tilted or splitted jet.

A comparison of the North Atlantic JLI between ERA5 reanalysis and the model in the various configurations is shown in Fig. 5.34. The model always underestimates the frequency of occurrence of the southern regime. This is coherent with the underestimation, irrespective of the orographic parameterizations and settings used, of blocking frequency over Greenland as shown by a two-dimensional blocking index (see next section). All model configurations overestimate the frequency of the central jet, however the new parameterizations alleviate the problem. Moreover, using the newFD_newGWD_highdrag configuration, the model overestimate the occurrency of the norther jet location.

A more complete view of the eddy-driven North Atlantic jet can be obtained looking at two additional diagnostics. The mean two-dimensional structure of the jet can be studied plotting, at each longitude, the average position of the maximum 850 hPa zonal wind speed (Fig. 5.35, left panel), while the longitudinal dependence of the jet speed can be displayed plotting, at each longitude, the average maximum 850 hPa zonal wind speed (same figure, right panel).

The old parameterizations produce a jet in the right location west of 20W while, approaching western Europe, the jet core deviates southward instead of going toward northern Europe. While the observed jet speed decreases almost monotonically from 50W to 0W, the maximum speed of the modeled jet is found at approximately 25W. The jet is too slow westward of 25W and too strong eastward.

Perturbing the new schemes' parameters, we can obtain a broad range of jet tilt and speed. Increasing the drag the jet is, on average, displaced northward, and over the eastern part of the North Atlantic basin it nicely follows the path of the observed jet, approaching 58N at 0W. On the contrary, lowering the drag the jet path over North Atlantic is more and more similar to what is obtained with old parameterizations. A clear systematic effect can be noticed also for jet speed, with higher drag determining a slower jet and vice versa. However, the new parameterizations can not change how the jet speed change with longitude, an aspect which remains quite unrealistic in all model configurations.

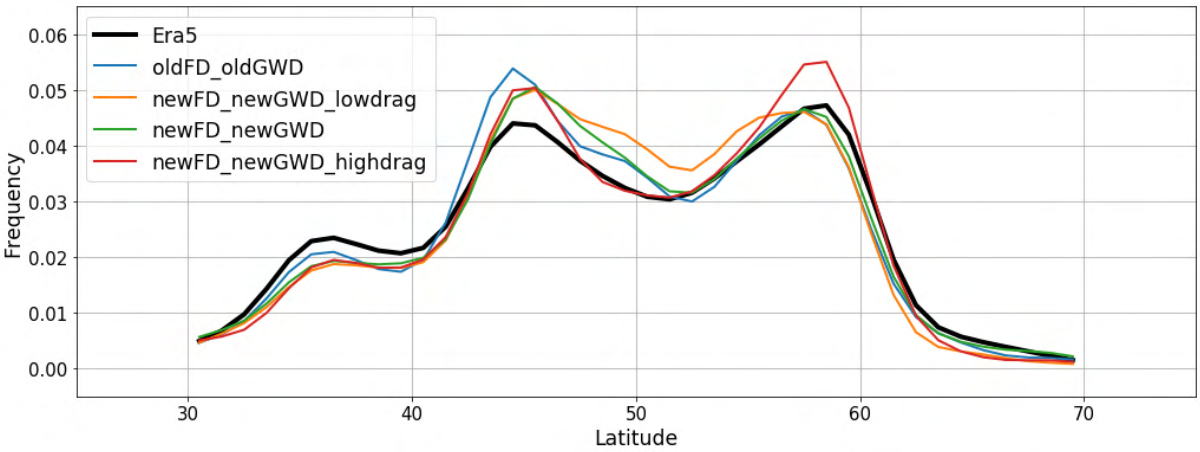

FIGURE 5.34: Jet Latitude Index (Woollings, Hannachi, and Hoskins, 2010) over the North Atlantic sector [0W-60W; 30N-70N] from ERA5 reanalysis data and from the four model experiments (upper panel) and bias of the experiments with respect to ERA5 (bottom panel).

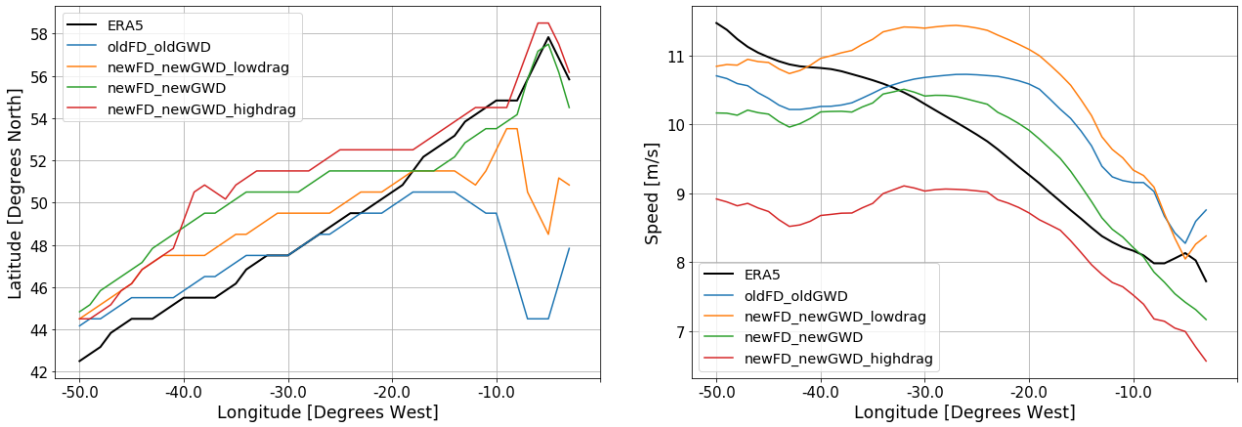

FIGURE 5.35: Left: latitude of the maximum zonal wind speed, at each longitude (North Atlantic sector, DJF season). Right: maximum zonal wind speed, at each longitude (North Atlantic sector, DJF season).

5.5.3 Blocking Frequency

New parameterizations also greatly influence the simulated atmospheric blocking frequency. While over the Pacific Sector there is no a clear trend in simulated frequency changing schemes' parameters, nor there is a marked difference between old and new parameterizations, we find that over the Atlantic sector the new schemes' parameters significally modulate simulated blocking frequency.

Looking at the 1D index (Fig. 5.36), the old model shows a 50% underestimation of blocking frequency around longitude 0. The simple introduction of new schemes reduced the underestimation to a more tolerable 15%, but the perturbation of the schemes' parameters greatly influences the model ability in reproduced the observed blocking frequency. Decreasing the drag, the modeled blocking frequency drops to values close to what we obtain with the old model, while an increased drag leads to blocking frequencies nearly identical to reanalysis around the Greenwich meridian.

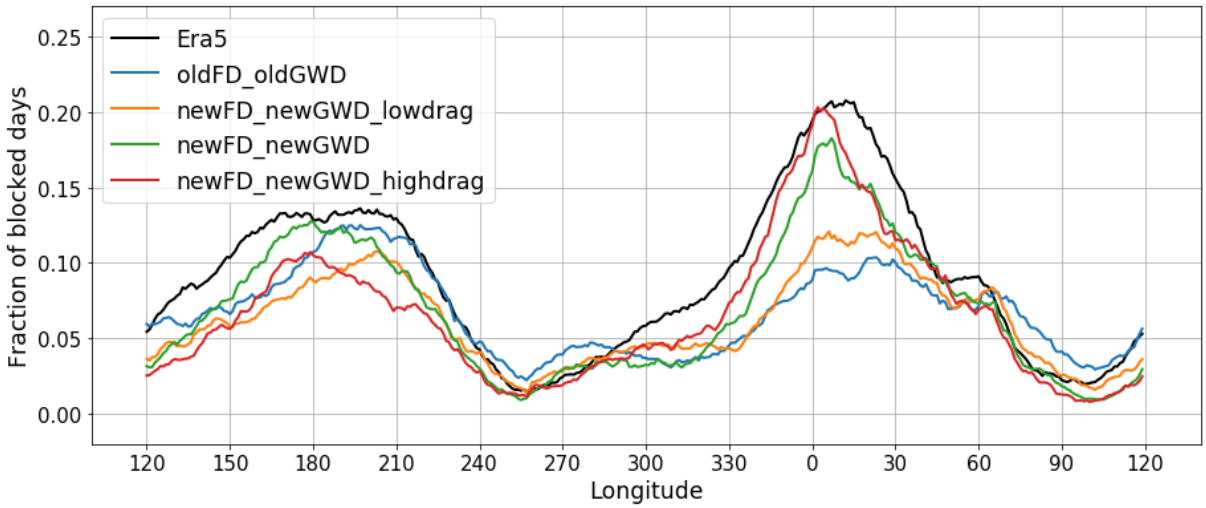

FIGURE 5.36: Instantaneous blocking frequency (Tibaldi and Molteni, 1990 index) from ERA5 reanalysis data and from the four model experiments, DJF season.

Looking at the two-dimensional index (Fig. 5.37) we can have a better idea of the geographical location of blocking with the different model configurations. Pacific blocking occurs mainly at high latitudes, at the northern flank of the Pacific jet stream. The frequency of these events is always slightly underestimated, but there are no marked differences between the four examined model configurations. The two main blocking frequency peaks over the NA-European sector are over Greenland and between eastern Atlantic and Scandinavia. The highest model sensitivity to the schemes and the parameters value used is found over Northern Europe, where the shape and the intensity of the frequency maximum is much better simulated with new parameterizations and higher values for the parameters. The simulated Greenland blocking frequency is slightly improved with new schemes, but it does not show a systematic behavior changing the drag parameters.

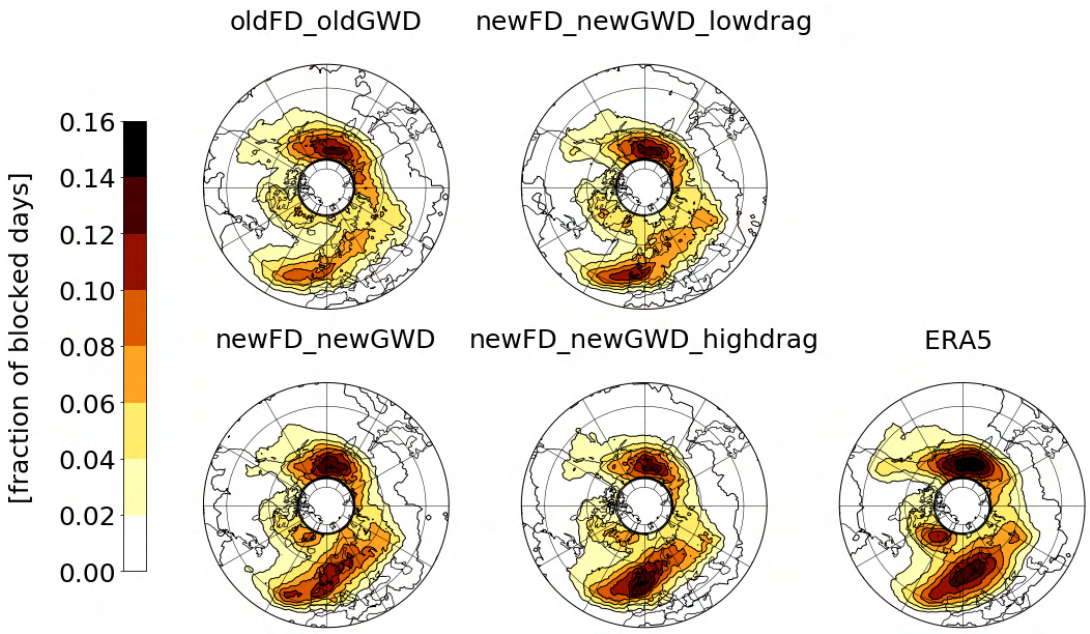

FIGURE 5.37: DJF instantaneous blocking frequency (Woollings, Barriopedro, and Methven, 2018 index) as calculated for ERA5 reanalysis data (bottom right) and for the four model experiments.

5.5.4 Cold and Heat Waves associated with Blocking, Euro-Atlantic Sector, DJF

The aim of this section is to study the connection between atmospheric blocking and extreme temperatures events over Europe, and the possible influence of orographic parameterizations on this link. To do so, we decided to combine the Tibaldi and Molteni, 1990 1D blocking index and the HCWI index for cold and heat waves (Lavaysse, Cammalleri, and Dosio, 2018, see chapter 4). In order to have a common and consistent framework to detect both extreme temperature and blocking events, we decided to impose a common minimum duration threshold for both events, set to 3 days.

The frequency of Blocking Events with a minimum duration of 3 days is shown in Fig. 5.38. The variation of frequency with longitude is almost identical to the istantaneous blocking one; the difference is in the magnitude, since short blocking events are discarded. Since we are interested in the link between blocking and extreme temperatures over Europe, we selected the dates corresponding to blocking events over the sector [30W, 60E].

At the same time, we computed for all dates and gridpoints the HCWI index, determining the locations and the dates of all heat and cold waves events with a duration of at least 3 days. To quantify the link between blocking and heat/cold waves, we decided to calculate, at each gridpoint, the fraction of the total number of heat/cold wave days happening when a blocking event is simultaneously detected over the aforementioned sector. As can be seen from Figs. 5.39 and 5.40, ERA5 data show that, during winter, blocking events are associated with the great majority (>75%) of cold days over the mediterranean region and of hot days over the Northeastern Atlantic - Scandinavian region. This kind of pattern is consistent with the anticyclonic structure of blocks and the associated air advection (Kautz, Martius, and Pfahl, 2021). Higher fractions could be obtained with more sophisticated algorithms, considering different duration limits or taking into account a lag between the block and the temperature anomalies, however we preferred to not complicate our method in order to keep the interpretation as simple as possible.

The same figures show that the observed relation between blocking and cold/heat waves

was not reproduced by the old model. Introducing new parameterizations the observed signal is better simulated, but the specific values of the orographic parameters are crucial in order to achieve realistic results. A lower orographic drag causes, for both heat and cold waves, a deterioration of the modeled association between blocking and extreme temperatures, obtaining results similar to the old parameterizations. On the contrary, and increased drag allow to obtain results more and more similar to the reanalysis.

To check the physical consistency of our results, we examined the mean temperature anomalies associated with blocking events over the European sector, in ERA5 and in all the model configurations considered (Fig. 5.41). Again, better results are obtained with the new parameterizations with "high drag" settings. In particular, old parameterizations, and new parameterizations with low drag settings, simulate stronger than observed mean temperature anomalies, with the cold temperature minimum located eastward (around 60E) with respect to observations. We believe that this behaviour is due to the fact that in the sector [30W-30E] the old schemes and the new schemes with low drag settings severely underestimates blocking frequency, while they reproduce the observed frequency reasonably well between 30E and 60E. Therefore, since western European blocks are underrepresented, the average temperature anomaly pattern during blocking events is mainly determined by eastern European blocks. The better modeling of atmospheric blocking around longitude 0, obtained with new parameterizations and a higher drag, leads to an improved simulation of extreme temperatures events climatology.

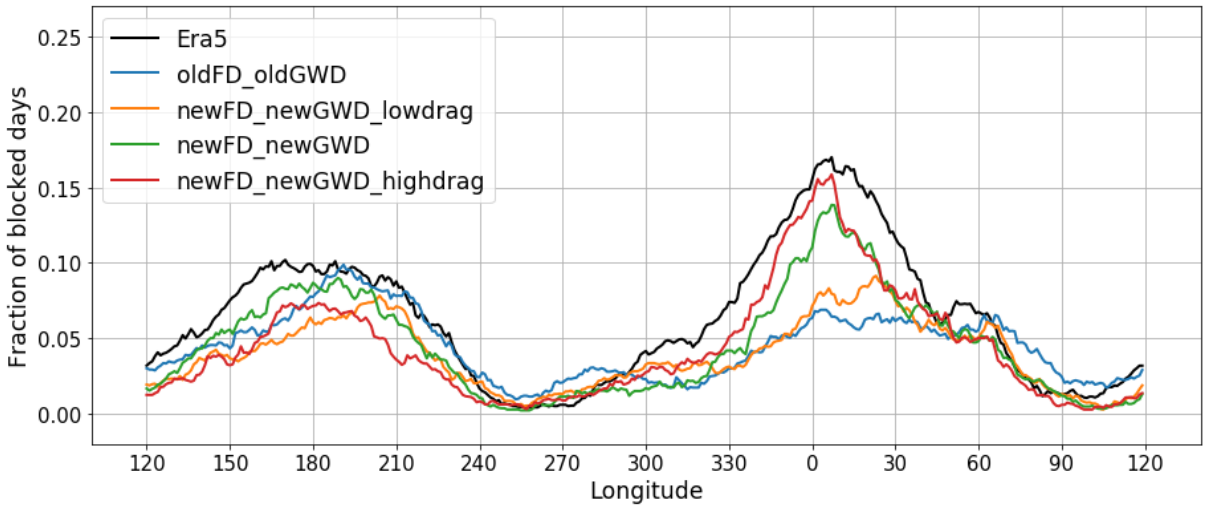

FIGURE 5.38: Blocking events frequency (Tibaldi and Molteni, 1990 index) from ERA5 reanalysis data and from the four model experiments, DJF season. Blocking events have a minimum duration of 3 days.

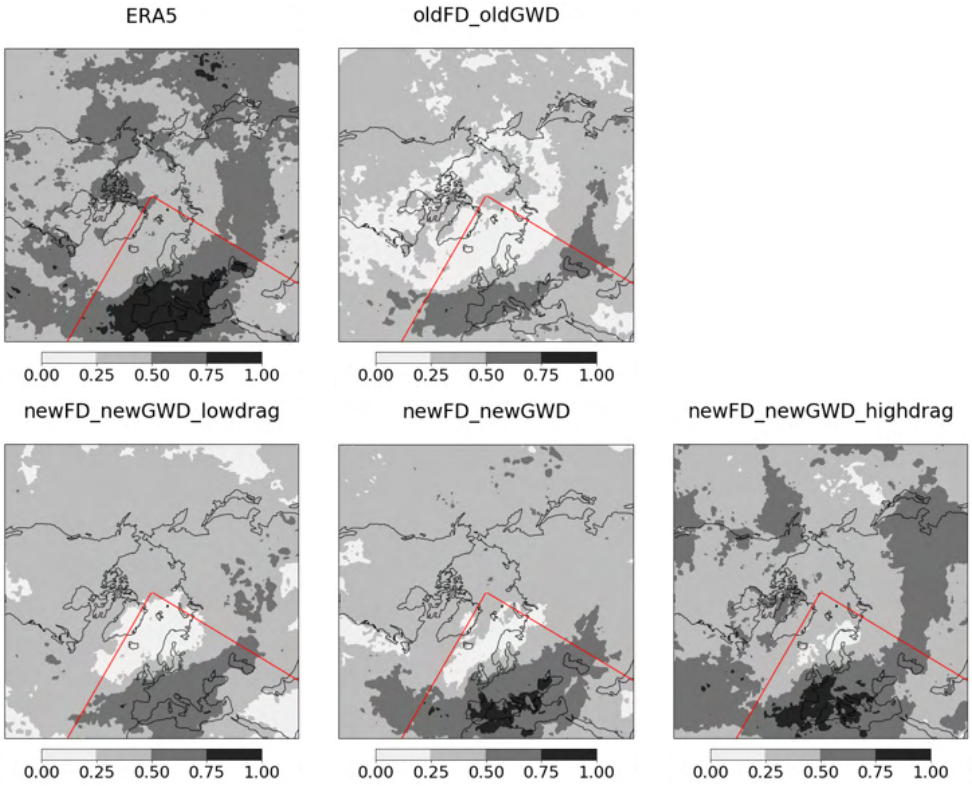

FIGURE 5.39: Fraction of the total number of cold wave days happening when a blocking event is simultaneously detected (using the Tibaldi and Molteni, 1990 index, see text) in the sector [30W-60E] (indicated with red lines), DJF season.

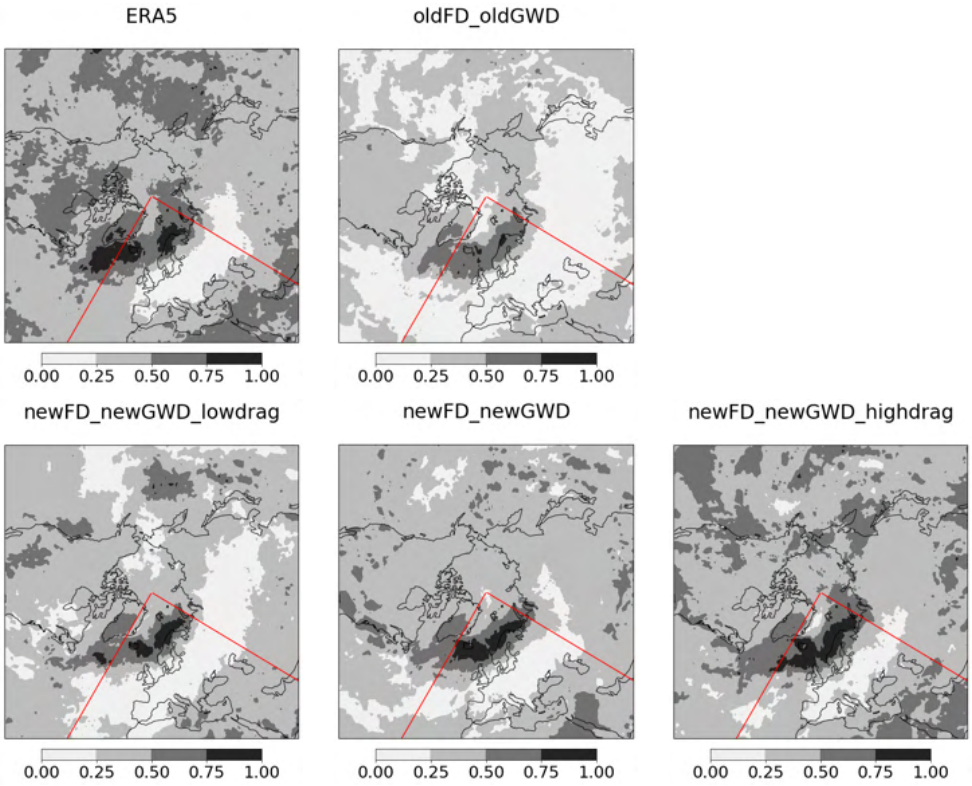

FIGURE 5.40: Fraction of the total number of heat wave days happening when a blocking event is simultaneously detected (using the Tibaldi and Molteni, 1990 index, see text) in the sector [30W-60E] (indicated with red lines), DJF season.

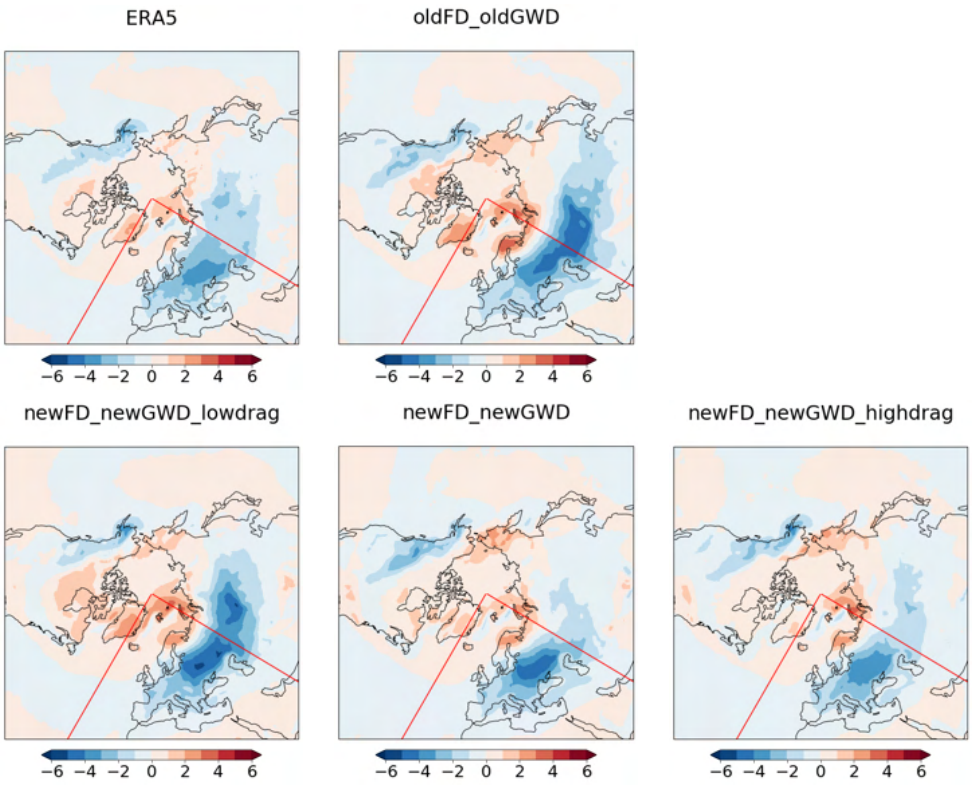

FIGURE 5.41: Average daily mean 2-meters temperature anomaly during blocking events, DJF season.

5.5.5 Stratosphere and Sudden Stratospheric Warmings

Finally, we studied how the new orographic schemes and their parameters perturbation affects stratospheric wind and Sudden Stratospheric Warmings (SSWs). The key variable used is the zonal mean zonal wind at 60° N and 10 hPa ($U_{60N-10hPa}$). This quantity is often used in the literature to characterize the stratospheric polar vortex.

Fig. 5.42 displays the climatology of $U_{60N-10hPa}$ from November 1st to April 30th, obtained averaging, at each calendar day, the value of $U_{60N-10hPa}$ over all years from 1979 to 2017. ERA5 reanalysis data show a climatological peak in $U_{60N-10hPa}$ at the end of December, a sudden deceleration of the polar vortex in the second half of January and then a progressive deceleration during spring, reaching a negative (easterly) velocity by the end of April . However, the oldFD_oldGWD experiment shows quite different properties. At the beginning of November the polar vortex climatological speed is lower than observed, and the peak speed is reached around December 1st. During the whole winter, the average polar vortex speed remains rather constant. So, around the end of January, the oldFD_oldGWD model polar vortex becomes stronger than observed and, oppositely to observations, $U_{60N-10hPa}$ slightly increases until the beginning of March, when the maximum mean speed is found, and then suddenly drops to values similar to reanalysis by the end of April. It is interesting to note that this wrong seasonality would be masked by a DJF mean of the zonal mean wind at 10 hPa, so the apparently good results obtained in winter by the oldFD_oldGWD model in the stratosphere (Figures 5.3 and 5.32) actually hide this opposite bias found in early and late winter.

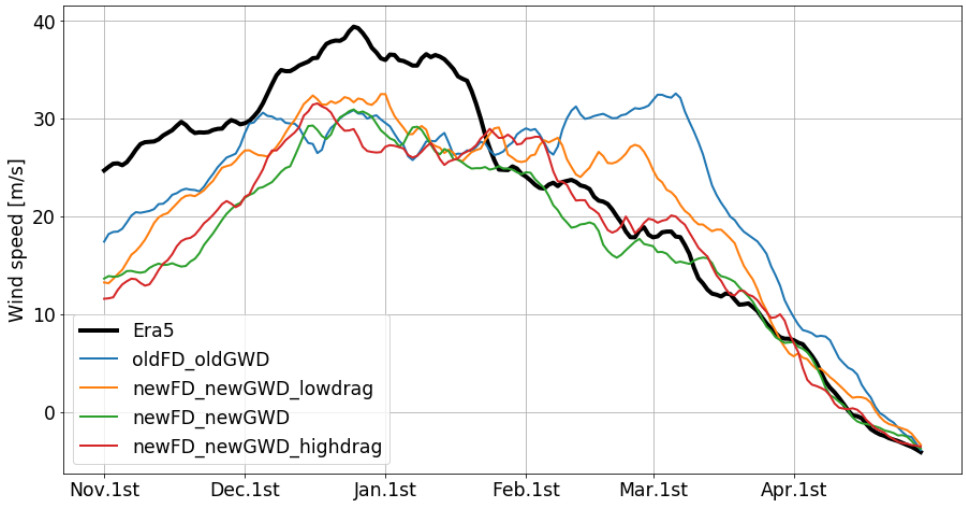

FIGURE 5.42: Climatological zonal mean zonal wind at 60N and 10 hPa, from November 1st to April 30th, for ERA5 reanalysis and the four model experiments.

The dynamical evolution of the winter Stratosphere can be greatly influenced by Sudden Stratospheric Warming (SSW) events. In this work, SSWs are detected applying the method of Charlton and Polvani, 2007 discussed in chapter 4. When applied to ERA5 data, it finds SSW dates in agreement with what is found in other reanalysis by other authors (Charlton and Polvani, 2007; Butler et al., 2017; Cao et al., 2019). The total number of events is limited to 24 events in 39 years, so it is difficult to isolate the effects of internal variability and to build a robust statistics. However, it is still interesting to compare observed and modeled SSWs frequency. In fact, the oldFD_oldGWD experiment shows a consistency between the seasonality of $U_{60N-10hPa}$ and of the frequency of SSW events. Using the oldFD_oldGWD configuration, the model produced some SSW in November, oppositely to observations. Since a SSW correspond

to a reversal of $U_{60N-10hPa}$ from westerly to easterly, this fact is consistent with a lower-than-observed $U_{60N-10hPa}$ in November. The frequency of SSW is well simulated in December but is excessive in January when, in fact, the modeled polar vortex speed continues to be lower than observed. On the contrary, a lack of simulated events in February is consistent with a polar vortex with constant speed until the beginning of March. The modeled SSW frequency in April and March coincides whit the polar vortex sudden deceleration.

When the new parameterization schemes are used, a better agreement between simulated and observed $U_{60N-10hPa}$ is found from the end of January onward. In fact, the model better reproduce the polar vortex deceleration, and this is consistent with a more realistic SSW frequency in January and February (less than oldFD_oldGWD in January, more than oldFD_oldGWD in February). However, the polar vortex is still slower than observed in the first part of the winter season. Unlike what we found looking at tropospheric processes, systematic effects of the modified orographic drag are not evident in the stratosphere. This is noticeable also looking at Fig. 5.32, where only small differences between the different experiments in the zonal wind at 10 hPa are noticeable. We believe that this is due to the compensating effect between the two perturbed schemes already discussed. The only noticeable effect is that, similarly to what we found in the previous sections, the newFD_newGWD_lowdrag experiment tends to show similarities with the oldFD_oldGWD configuration, in particular looking at $U_{60N-10hPa}$ in November and in February-March.

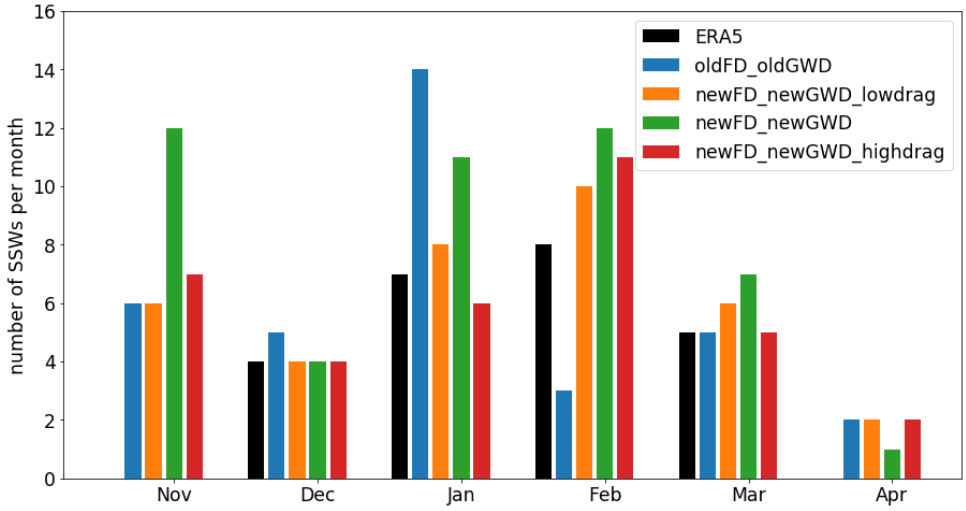

FIGURE 5.43: Number of detected SSWs in each month, for ERA5 reanalysis and the four model experiments.

Chapter 6

Summary and conclusions

The improvement of models' ability in reproducing the observed features of atmospheric general circulation is crucial in order to have more reliable future climate prediction, and identifying meliorative modeling strategies is essential to guide model development. In this work, we examined the capability of a General Circulation Model to simulate the winter Northern Hemisphere mid-latitudes atmospheric circulation, and in particular the effects that the representation of unresolved orographic drag processes might have on it. The model considered is the Community Atmosphere Model (CAM, in its version 5.3), the atmospheric component of the Community Earth System Model (CESM) developed at the National Center for Atmospheric Reseach (NCAR). The default physical parameterization package include the McFarlane, 1987 scheme to simulate vertically propagating orographic gravity waves and the Richter, Sassi, and Garcia, 2010 Turbulent Mountain Stress (TMS) scheme to take into account the turbulent form drag exerted on the atmospheric flow by small scale orography. The update of the CAM model to its version 6 has made available two new parameterizations of orographic drag. First, a new gravity wave code, inspired by the work of Scinocca and McFarlane, 2000, which takes into account not only the vertical propagation of small amplitude gravity waves, but also the effects of orographic flow-blocking and of low-level wave breaking. These last two features, and the fact that the orientation of the unresolved topographic ridges are considered, represent an important conceptual step forward with respect to the physics taken into account by the McFarlane, 1987 scheme. Second, the Beljaars, Brown, and Wood, 2004 form drag scheme. Older schemes, and also the TMS, typically take into account the turbulent orographic form drag by enhancing the surface stress via an increased roughness length. This means that the scheme directly influence the vertical flux of horizontal momentum only at the surface. Instead, this new scheme calculates a vertical profile of stress which depends of the local properties of the unresolved orography.

The innovations introduced by these new schemes has the potential to reduce the mid-latitudes circulation biases affecting CAM, which are shared with many climate and NWP models and which limit their ability of providing accurate predictions of the future climate. However, the inherent uncertainties present also in these new, state-of-the-art parameterizations constitute a source of potential errors (see the Introduction for a discussion on this point). Therefore, there is the need to evaluate these schemes in different models, and to study how the uncertainties on some fundamental parameters affect the realism of simulations. These are the main reasons which motivated this thesis.

To conduct our analysis, we designed and performed different sets of simulations, integrating the atmospheric model in and AMIP-like mode, that is forced with observed SSTs and sea ice conditions. In a first set of experiment, we introduced the new form drag (FD) and gravity wave drag (GWD) schemes in the model, in place of the older. We ran the model in all the four possible configuration switching alternatively on and off the new and the old schemes (oldFD_oldGWD; oldFD_newGWD; newFD_oldGWD; newFD_newGWD). The individual effect of the new schemes and their mutual interaction are studied comparing model output to reanalysis data (ERA5) during winter (DJF). In general, the introduction of the new schemes

reduces the mid-latitudes zonal-mean zonal wind westerly bias, in the whole troposphere and particularly in the Northern Hemisphere (NH). The improvements are due to a reduction of the speed of the tropospheric jet in the NH and in an equatorward shift of the jet in the Southern Hemisphere. Examining the parameterized surface stresses, it has been possible to highlight the main differences between the old and the new codes. With respect to the old, the new FD scheme produces a surface stress which is more concentrated around the real mountain massifs, with higher maximum values. On the contrary, less stress is produced over plain regions. Similarly, the new GWD code, which takes into account also the low-level drag caused by flow blocking and wave breaking, produced an higher stress over mountanious regions. The two schemes depend and act at the same time on the same variable, that is the resolved wind, in particular over regions of large unresolved orography. Therefore, they strongly influence each other. In particular, the new FD scheme can strongly damp the effects of both the old and the new gravity waves parameterizations. This is evident looking at the tendecies calulated by the GWD schemes used in combination with the different FD schemes. In any case, the additional tendencies calculated by the new schemes are well co-located with the observed zonal-mean zonal wind differences with respect to the old model.

In general, the introduction of the new schemes improves the overall representation of NH stationary waves, of mean sea level pressure (MSLP) and of geopotential height at different levels in the winter troposphere. The new GWD scheme gives good results in particular over the Euro-Atlantic sector, while the new FD scheme improves the stationary waves at all levels and over the whole NH. Up to 250 hPa, both schemes reduce the jet strength over the Pacific and the Atlantic sectors, reducing the positive zonal wind bias over south-western Europe but deteriorating the bias over the Pacific Ocean. In the stratosphere, the new FD scheme has marginal effects, while the new GWD scheme produces a deceleration of the zonal wind, consistently with the increased negative wind tendencies produced there. When the new schemes are used at the same time, their cumulative effects in the troposphere remains quite unchanged, while the negative stratospheric footprint of the new GWD scheme disappears, confirming the modulating effect of the new FD scheme. A negative effect of the introduction of the new parameterizations is the developement of an high pressure bias over the North Pole, which is consistent with a geostrophic response to reduced surface westerlies.

After this general characterization of the two parameterization, we studied how the values of two fundamental but uncertain parameters of the schemes influence their effects. This was done running the model with both the new schemes active, and perturbing the default value of the parameters, one at a time (the default numerical values were halved and doubled). For the new FD scheme, the considered parameter is responsible for the modulation of the whole stress profile, while for the new GWD scheme we perturbed the efficiency factor controlling the conversion of the calculated momentum flux profile into wind tendencies. Therefore, they both control the final parameterized drag force exerted on the atmospheric flow. Interestingly, we found a strong correspondence between the effects of decreasing the FD parameter and increasing the orographic OGWD efficiency parameter, and vice versa; moreover, in both cases, opposite impacts on the zonal wind are observed over the Atlantic and Pacific sectors. Specifically, a decreased FD or an increased GWD reinforces the tropospheric jet over the Pacific ocean but weakens it over the Atlantic sector, and weakens the stratospheric polar vortex. The opposite is true changing the sign of the perturbations. The positive MSLP bias over the North Pole is reduced whenever the drag parameters are decreased.

So, both the two unconstrained numerical factors controlling the physical impact of the two parameterizations have the potential to greatly influence the simulation of the tropospheric winter mid-latitudes circulation and of the polar vortex, and there is a high degree of overlapping between the impacts obtained changing their distinct values.

Therefore, we wanted to assess more precisely how the simulation of specific atmospheric

processes can be affected by uncertainties on the whole orographic drag parameterization package. That is, we perturbed both schemes at the same time checking the results of the simulations using a set of objective diagnostics. Given the outcomes of the previous set of experiments, we decided to run the model with both the orographic parameters simultaneously decreased or increased. Additionally, the model is run with unperturbed parameters and with both the old parameterizations.

For the great majority of the processes we examined, we found a qualitatively linear relationship between parameters values and model response. That is, simultaneously changing the values of α and $effgw\_rdg$ it is possible to modulate the simulated properties of some key features of the mid-latitudes atmospheric circulation. Increasing the parameters values, we found that:

- the North Atlantic storm track became less intense and more northerly tilted over eastern Atlantic and western Europe;
- the North Atlantic eddy-driven jet is displaced northward, decelerated and deflected toward northwestern Europe;
- Euro-Atlantic blocking frequency is considerably increased, while Greenland blocking and North Pacific blocking frequency are not significantly altered.

In other words, increasing parameters values determines a general decrease of the biases affecting the standard CAM5 model, while decreased parameters push the simulated climate toward what is found with old parameterizations. The frequency distribution of Sudden Stratospheric Warmings (SSWs) during winter months in not significantly affected, however a general improvement in how new parameterizations reproduce the seasonal cycle of zonal mean zonal wind at 60° N, 10 hPa is found. Finally, we combined a blocking and a heat/cold wave index to create a system to study the association between atmospheric blocking and extreme temperature events over the Euro-Atlantic domain. Again, we found that orographic parameters modulates the representation of cold and heat waves connected to blocking events during winter.

Summarizing, we showed that the introduction of two new orographic drag parameterization schemes can reduce some important biases of the CAM5 model, in particular at mid-latitudes during winter. The reduction of these climatological biases improves the model mean state, its variability and its capability to simulate extreme events statistics, increasing its ability in reproducing the observed climate of highly populated regions of our planet. The same kind of biases are present, and have been for a long time, in many other climate models, so these results confirm the great importance of orographic drag parameterizations for the future developement of more and more reliable climate models. Furthermore, this work provides additional evidence of the link between Euro-Atlantic blocking and North Atlantic storm track and jet biases, identifying the representation of missing orographic processes as a key factor for improving models. However, the potential beneficial effects of the considered parameterizations can be obscured by the intrinsic uncertainty they are afflicted by. In this work we examined the range of impacts on the atmospheric circulation which can be caused by our ignorance on some fundamental physical parameters, providing a guidance for the implementation of these schemes in other models also. Our work, however, it is not an attempt to fine-tune our model: the analysis showed how an increase of the orographic drag parameters generally corresponds to the development of a high pressure bias over the North Pole. A reduction of this type of bias in the U. K. Met Office model has been achieved by Williams et al., 2020, who adjusted not only the unresolved orographic drag parameters, but also the land surface stress scheme and the resolved orography filtering. Moreover, the safe and successful re-distribution of model surface drag, minimizing the risk of introducing new compensating errors, has been possible

only exploiting the "seamlessness" of the model, that is checking that reduced climatological biases correspond to an increased, or at least not reduced, short-term forecast accuracy. Studying the redistribution of the drag across all the mechanisms responsible for it in CAM would be a promising future developement of this work.

Finally, we showed that an additional source of uncertainty is given by the fact that different schemes, representing different types of orographic processes acting on different scales, strongly interact amplifying or damping the effects of each other (which is one of the reason why it is difficult to understand how to distribute drag across different schemes). The future developement of models should aim to a "great unification" of all orographic parameterizations, in order to obtain a coherent representation of all relevant processes across the whole range of unresolved scales. This will only be possible by increasing our theoretical and observational knowledge of the processes themselves.

Bibliography

Ambaum, M. H. P., B. J. Hoskins, and G. Stephenson (2001). "Arctic Oscillation or North Atlantic Oscillation?" In: *Journal of Climate* 14, 3495– 3507.

Anstey, J. A. et al. (2013). "Multi-model analysis of Northern Hemisphere winter blocking: Model biases and the role of resolution". In: *J. Geophys. Res. Atmos.* 118, pp. 3965–3971.

Bacmeister, J. T. and R. T. Pierrehumbert (1988). "On High-Drag States of Nonlinear Stratified Flow over an Obstacle". In: *J. Atmos. Sci.* 45, pp. 63–80.

Baldwin, M. P. and T. J. Dunkerton (2001). "Stratospheric Harbingers of Anomalous Weather Regimes". In: *Science* 294, 581– 584.

Batchelor, G. K. (1967). *An Introduction to Fluid Dynamics*. Ed. by Cambridge University Press.

Belcher, S. E., T. M. J. Newley, and J. C. R. Hunt (1993). "The drag on an undulating surface induced by the flow of a turbulent boundary layer". In: *J. Fluid Mech.* 249, pp. 557–596.

Belcher, S.E. and N. Wood (1996). "Form and wave drag due to stably stratified turbulent flow over low ridges". In: *Q. J. R. M . S.* 122, pp. 863–902.

Beljaars, A. C. M., A. R. Brown, and N. Wood (2004). "A new parametrization of turbulent orographic form drag". In: *Quarterly Journal of the Royal Meteorological Society* 130, pp. 1327–1347.

Berckmans, J. et al. (2013). "Atmospheric blocking in a high resolution climate model: influences of mean state, orography and eddy forcing". In: *Atmos. Sci. Let.* 14, pp. 34–40.

Beres, J. H., M. J. Alexander, and J. R. Holton (2004). "A method of specifying the gravity wave spectrum above convection based on latent heating properties and background wind". In: *J. Atmos. Sci.* 61, pp. 324–337.

Beres, J. H. et al. (2005). "Implementation of a gravity wave source spectrum parameterization dependent on the properties of convection in the Whole Atmosphere Community Climate Model (WACCM)". In: *J. Geophys. Res.* 110.

Boer, G. J. et al. (1984). "The Canadian Climate Centre spectral atmospheric general circulation model". In: *Atmosphere-Ocean* 22:4, pp. 397–429.

Bretherton, C. S. and S. Park (2009). "A New Moist Turbulence Parameterization in the Community Atmosphere Model". In: *Journal of Climate* 22, pp. 3422–3448.

Brown, A. R. (2004). "Resolution dependence of orographic torques". In: *Q. J. R. M. S.* 130, pp. 3029–3046.

Butler, A. H. et al. (2017). "A sudden stratospheric warming compendium". In: *Earth Syst. Sci. Data* 9, pp. 63–76.

Cagnazzo, C. and E. Manzini (2009). "Impact of the Stratosphere on the Winter Tropospheric Teleconnections between ENSO and the North Atlantic and European Region". In: *Journal of Climate* 22, pp. 1223–1238.

Cao, C. et al. (2019). "Statistical Characteristics of Major Sudden Stratospheric Warming Events in CESM1-WACCM: A Comparison with the JRA55 and NCEP/NCAR Reanalyses". In: *Atmosphere* 10, p. 519.

Castanheira, J. M. and D. Barriopedro (2010). "Dynamical connection between tropospheric blockings and stratospheric polar vortex". In: *Geophysical Research Letters* 37, p. L13809.

Chang, E. K. M., S. Lee, and K. L. Swanson (2002). "Storm Track Dynamics". In: *Journal of Climate* 15, pp. 2163–2183.

Charlton, A. J. and L. M. Polvani (2007). "A New Look at Stratospheric Sudden Warmings. Part I: Climatology and Modeling Benchmarks". In: *Journal of Climate* 20, pp. 449–469.

Charlton, A. J et al. (2007). "A New Look at Stratospheric Sudden Warmings. Part II: Evaluation of Numerical Model Simulations". In: *Journal of Climate* 20, pp. 470–488.

Charlton-Perez, A. J. et al. (2013). "On the lack of stratospheric dynamical variability in low-top versions of the CMIP5 models". In: *Journal of Geophysical Research: Atmospheres* 118, pp. 2494–2505.

Charney, J. G. and P. G. Drazin (1961). "Propagation of planetary-scale disturbances from the lower into the upper atmosphere". In: *J. Geophys. Res.* 66, pp. 83–109.

Colle, B. A. et al. (2013). "Historical Evaluation and Future Prediction of Eastern North American and Western Atlantic Extratropical Cyclones in the CMIP5 Models during the Cool Season". In: *Journal of Climate* 26, 6882– 6903.

D'Andrea, F. T. et al. (1998). "Northern Hemisphere atmospheric blocking as simulated by 15 atmospheric general circulation models in the period 1979–1988". In: *Climate Dynamics* 14, pp. 385–407.

Davies, L. A. and A. R. Brown (2001). "Assessment of which scales of orography can be credibly resolved in a numerical model". In: *Q. J. R. Meteorol. Soc.* 127, pp. 1225–1237.

Davini, P. and C. Cagnazzo (2014). "On the misinterpretation of the North Atlantic Oscillation in CMIP5 models". In: *Climate Dynamics* 43, 1497–1511.

Davini, P. and F. D'Andrea (2016). "Northern Hemisphere Atmospheric Blocking Representation in Global Climate Models: Twenty Years of Improvements?" In: *Journal of climate* 29, pp. 8823–8840.

— (2020). "From CMIP3 to CMIP6: Northern Hemisphere Atmospheric Blocking Simulation in Present and Future Climate". In: *Journal of climate* 33, pp. 10021–10038.

Davini, P. et al. (2012). "Bidimensional Diagnostics, Variability, and Trends of Northern Hemisphere Blocking". In: *Journal of Climate* 25, pp. 6496–6509.

Dawson, A., T. N. Palmer, and S. Corti (2012). "Simulating regime structures in weather and climate prediction models". In: *Geophysical Research Letters* 39, p. L21805.

Delcambre, S. C. et al. (2013). "Diagnosing Northern Hemisphere Jet Portrayal in 17 CMIP3 Global Climate Models: Twentieth-Century Intermodel Variability". In: *Journal of Climate* 26, pp. 4910–4929.

Dennis, J.M. et al. (2012). "CAM-SE: A scalable spectral element dynamical core for the Community Atmosphere Model". In: *The International Journal of High Performance Computing Applications* 26, pp. 74–89.

Duchon, C. E. (1979). "Lanczos Filtering in One and Two Dimensions". In: *Journal of Applied Meteorology* 18, pp. 1016–1022.

Dunn-Sigouin, E. and S. Son (2013). "Northern Hemisphere blocking frequency and duration in the CMIP5 models". In: *J. Geophys. Res. Atmos.* 118, pp. 1179–1188.

Durran, D. R. (1990). "Mountain Waves and Downslope Winds". In: *Atmospheric Processes Over Complex Terrain*. Ed. by American Meteorological Society.

— (2003). "Lee waves and Mountain Waves". In: *Encyclopedia of Atmospheric Sciences*, pp. 1161–1169.

Eichler, T. P., N. Gaggini, and Z. Pan (2013). "Impacts of global warming on Northern Hemisphere winter storm tracks in the CMIP5 model suite". In: *J. Geophys. Res. Atmos.* 118, 3919–3932.

Eliassen, A. and E. Palm (1961). "On the Transfer of Energy in Stationary Mountain Waves". In: *Geophysica Norvegica* XXII, no. 3.

Elvidge, A. D. et al. (2019). "Uncertainty in the representation of orography in weather and climate models and implications for parameterized drag". In: *Journal of Advances in Modeling Earth Systems* 11, pp. 2567–2585. URL: https://doi.org/10.1029/2019MS001661.

Eyring, V. et al. (2016). "Overview of the Coupled Model Intercomparison Project Phase 6 (CMIP6) experimental design and organization". In: *Geosci. Model Dev.* 9, 1937– 1958.

Fiedler, F. and H.A. Panofsky (1972). "The geostrophic drag coefficient and the 'effective' roughness length". In: *Quarterly Journalof the Royal Meteorological Society* 415, pp. 213–220.

Franzke, C., T. Woollings, and O. Martius (2011). "Persistent Circulation Regimes and Preferred Regime Transitions in the North Atlantic". In: *Journal of the Atmospheric Sciences* 68, pp. 2809–2825.

Gill, A. E. (1982). *Atmosphere-Ocean Dynamics*. Ed. by Academic Press. International geophysics series.

Grant, L.M. and P. J. Mason (1990). "Observations of boundary-layer structure over complex terrain". In: *Q. J. R. M . S.* 116, pp. 159–186.

Gregory, D., G. J. Shutts, and J. R. Mitchell (1998). "A new gravity-wave-drag scheme incorporating anisotropic orography and low-level wave breaking: Impact upon the climate of the UK Meteorological Office Unified Model". In: *Q. J. R. M. S.* 124, pp. 463–493.

Hall, R. J. et al. (2021). "Persistent model biases in the CMIP6 representation of stratospheric polar vortex variability". In: *Journal of Geophysical Research: Atmospheres* 126, e2021JD034759.

Hannachi, A., E. A. Barnes, and T. Woollings (2013). "Behaviour of the winter North Atlantic eddy-driven jet stream in the CMIP3 integrations". In: *Climate Dynamics* 41, pp. 995–1007.

Hannachi, A. et al. (2017). "Low-frequency nonlinearity and regime behavior in the Northern Hemisphere extratropical atmosphere". In: *Reviews of Geophysics* 55, pp. 199–234.

Harvey, B. J. et al. (2020). "The response of the northern hemisphere storm tracks and jet streams to climate change in the CMIP3, CMIP5, and CMIP6 climate models". In: *Journal of Geophysical Research: Atmospheres* 125, e2020JD032701.

Herrington, A.M. et al. (2019). "Physics–Dynamics Coupling with Element-Based High-Order Galerkin Methods: Quasi-Equal-Area Physics Grid". In: *Monthly Weather Review* 147, pp. 69–84.

Holton, J. R. (2012). *An Introduction to Dynamic Meteorology*. Ed. by Academic Press.

Hoskins, B. J. and D. Karoly (1981). "The Steady Linear Response of a Spherical Atmosphere to Thermal and Orographic Forcing". In: *Journal of the Atmospheric Sciences* 38, 1179–1196.

Hurrel, J. W. et al. (2008). "A New Sea Surface Temperature and Sea Ice Boundary Dataset for the Community Atmosphere Model". In: *Journal of Climate* 21, pp. 5145–5153.

Hurrell, J. W. et al. (2003). "An Overview of the North Atlantic Oscillation". In: *In The North Atlantic Oscillation: Climatic Significance and Environmental Impact*.

Iqbal, W., W. Leung, and A. Hannachi (2018). "Analysis of the variability of the North Atlantic eddy-driven jet stream in CMIP5". In: *Climate Dynamics* 51, pp. 235–247.

Jung, T. et al. (2010). "The ECMWF model climate: recent progress through improved physical parametrizations". In: *Q.J.R. Meteorol. Soc.* 136, pp. 1145–1160.

Jung, T. et al. (2012). "High-Resolution Global Climate Simulations with the ECMWF Model in Project Athena: Experimental Design, Model Climate, and Seasonal Forecast Skill". In: *Journal of Climate* 25, pp. 3155–3172.

Karoly, D. (1982). "Rossby wave propagation in a barotropic atmosphere". In: *Dynamics of Atmospheres and Oceans* 7, pp. 111–125.

Kautz, L., O. Martius, S. Pfahl, et al. (2021). "Atmospheric Blocking and Weather Extremes over the Euro-Atlantic Sector – A Review". In: *preprint submitted to Weather and Climate Dynamics*.

Kealy, J. C. (2019). "Probing the 'grey zone' of NWP – is higher resolution always better?" In: *Weather* 74, pp. 246–249.

Kidston, J. et al. (2015). "Stratospheric influence on tropospheric jet streams, storm tracks and surface weather". In: *Nature Geoscience* 8, 433– 440.

Kim, Y. (1996). "Representation of Subgrid-Scale Orographic Effects in a General Circulation Model. Part I: Impact on the Dynamics of Simulated January Climate". In: *Jornal of Climate* 9, pp. 2698–2717.

Kim, Y. and A. Arakawa (1995). "Improvement of Orographic Gravity Wave Parameterization Using a Mesoscale Gravity Wave Model". In: *J. Atmos. Sci.* 52, pp. 1875–1902.

Kim, Y., S. D. Eckermann, and H. Chun (2003). "An overview of the past, present and future of gravity-wave drag parametrization for numerical climate and weather prediction models". In: *Atmosphere-Ocean* 41. URL: https://doi.org/10.3137/ao.410105.

Kruse, C. G. et al. (2022). "Observed and Modeled Mountain Waves from the Surface to the Mesosphere Near the Drake Passage". In: *Journal of the Atmospheric Sciences* published online ahead of print 2022. URL: https://journals.ametsoc.org/view/journals/atsc/aop/JAS-D-21-0252.1/JAS-D-21-0252.1.xml.

Lauritzen, P. H. and D. L. Williamson (2019). "A total energy error analysis of dynamical cores and physics-dynamics coupling in the Community Atmosphere Model (CAM)". In: *Journal of Advances in Modeling Earth Systems* 11, pp. 1309–1328. DOI: https://doi.org/10.1029/2018MS001549.

Lauritzen, P. H. et al. (2018). "NCAR release of CAM-SE in CESM2.0: A reformulation of the spectral element dynamical core in dry-mass vertical coordinates with comprehensive treatment of condensates and energy". In: *Journal of Advances in Modeling Earth Systems* 10, pp. 1537–1570. DOI: https://doi.org/10.1029/2017MS001257.

Lauritzen, P.H. et al. (2015). "NCAR_Topo (v1.0): NCAR global model topography generation software for unstructured grids". In: *Geosci. Model Dev.* 8, 3975–3986. URL: https://doi.org/10.5194/gmd-8-3975-2015.

Lavaysse, C., C. Cammalleri, A. Dosio, et al. (2018). "owards a monitoring system of temperature extremes in Europe". In: *Nat. Hazards Earth Syst. Sci.* 18, pp. 91–104.

Lejenas, H. and H. Okland (1983). "Characteristics of northern hemisphere blocking as determined from a long time series of observational data". In: *Tellus* 35A, pp. 350–362.

Lilly, D. K. and E. J. Zipser (1972). "The Front Range Windstorm of 11 January 1972 a Meteorological Narrative". In: *Wheatherwise* 25, pp. 56–63.

Lindzen, R. S. (1981). "Turbulence and stress owing to gravity wave and tidal breakdown". In: *Journal of the Geophysical Research* 86, pp. 9707–9714.

Lott, F. and M. J. Miller (1997). "A new subgrid-scale orographic drag parametrization: Its formulation and testing". In: *Q. J. R. M. S.* 123, pp. 101–127.

Madonna, E. et al. (2017). "The link between eddy-driven jet variability and weather regimes in the North Atlantic-European sector". In: *Q. J. R. Meteorol. Soc.* 143, pp. 2960–2972.

Martius, O., L. M. Polvani, and H. C. Davies (2009). "Blocking precursors to stratospheric sudden warming events". In: *Geophysical Research Letters* 36, p. L14806.

Masato, G., B. J. Hoskins, and T. Woollings (2013). "Winter and Summer Northern Hemisphere Blocking in CMIP5 Models". In: *Journal of climate* 26, pp. 7044–7059.

Mason, P. J. (1985). "On the Parametrization of Orographic Drag". In: *ECMWF Seminar on Physical Parametrization for Numerical Models of the Atmosphere*, pp. 139–165.

McFarlane, N. A. (1987). "The effect of orographically excited gravity wave drag on the general circulation of the lower stratosphere and troposphere". In: *Journal of the Atmospheric Sciences* 44, pp. 1775–1800.

Mesinger, F. and Z. I. Janjic (1986). "Numerical techniques for the representation of mountains". In: *Proc. Seminar/Workshop on observation, theory and modeling of orographic effects. ECMWF, Shinfield Park, Reading, U. K.* 2, pp. 29–80.

Miller, M. J., T. N. Palmer, and R. Swinbank (1989). "Parametrization and Influence of Subgridscale Orography in General Circulation and Numerical Weather Prediction Models". In: *Meteorol. Atmos. Phys* 40, pp. 84–109.

Milton, S.F. and C.A. Wilson (1996). "The impact of parametrized subgrid-scale orographic forcing on systematic errors in a global NWP model". In: *Mon. Weather Rev.* 124, pp. 2023–2045.

Miranda, P. M. A. and I. N. James (1992). "Non-linear three-dimensional effects on gravity-wave drag: Splitting flow and breaking waves." In: *Mon. Weather Rev.* 120, pp. 2962–2976.

Mitchell, D. M. et al. (2013). "The Influence of Stratospheric Vortex Displacements and Splits on Surface Climate". In: *Journal of Climate* 826, 2668– 2682.

Molina, M. O., C Gutiérrez, and E. Sánchez (2021). "Comparison of ERA5 surface wind speed climatologies over Europe with observations from the HadISD dataset". In: *Int J Climatol.* 41, 4864– 4878.

Neale, R. B. et al. (2012). *Description of the NCAR Community Atmosphere Model (CAM 5.0)*. NCAR technical note NCAR/TN-4861STR. URL: http://www.cesm.ucar.edu/models/cesm1.0/cam/docs/description/cam5_desc.pdf.

Nishii, K., H. Nakamura, and Y. J. Orsolini (2011). "Geographical Dependence Observed in Blocking High Influence on the Stratospheric Variability through Enhancement and Suppression of Upward Planetary-Wave Propagation". In: *Journal of Climate* 24, pp. 6408–6423.

Olafsson, H. and P. Bougeault (1996). "Nonlinear flow past an elliptic mountain ridge." In: *J. Atmos. Sci.* 53, pp. 193–210.

Oleson, K. W. et al. (2010). *Technical Description of version 4.0 of the Community Land Model (CLM)*. NCAR technical note NCAR/TN-478+STR. URL: https://www.cesm.ucar.edu/models/cesm2/land/CLM4_Tech_Note.pdf.

O'Reilly, C. H., S. Minobe, and A. Kuwano-Yoshida (2016). "The influence of the Gulf Stream on wintertime European blocking". In: *Climate Dynamics* 47, pp. 1545–1567.

Oudar, T., J. Cattiaux, and H. Douville (2020). "Drivers of the Northern Extratropical Eddy-Driven Jet Change in CMIP5 and CMIP6 Models". In: *Geophysical Research Letters* 47, e2019GL086695.

Palmer, T. N., G. J. Shutts, and R. Swinbank (1986). "Alleviation of a systematic westerly bias in general circulation and numerical weather prediction models through an orographic gravity wave drag parametrization". In: *Q. J. R. M. S.* 112, pp. 1001–1039.

Peixoto, J. P. and A. H. Oort (1992). *Physics of Climate*. Ed. by American Institute of Physics.

Pithan, F. et al. (2016). "Climate model biases in jet streams, blocking and storm tracks resulting from missing orographic drag". In: *Geophysical Research Letters* 43, 7231–7240.

Priestley, M. D. K. et al. (2020). "An Overview of the Extratropical Storm Tracks in CMIP6 Historical Simulations". In: *Journal of Climate* 33, 6315– 6343.

Rančić, M., R. J. Purser, and F. Mesinger (1996). "A global shallow-water model using an expanded spherical cube: Gnomonic versus conformal coordinates". In: *Quarterly Journal of the Royal Meteorological Society* 122.532, pp. 959–982. DOI: 10.1002/qj.49712253209. URL: https://rmets.onlinelibrary.wiley.com/doi/abs/10.1002/qj.49712253209.

Richter, J. H., F. Sassi, and R. R. Garcia (2010). "Toward a Physically Based Gravity Wave Source Parameterization in a General Circulation Model". In: *J.A.S.* 67, pp. 136–157.

Richter, J. H., A. Solomon, and J. T. Bacmeister (2014a). "Effects of vertical resolution and nonorographic gravity wave drag on the simulated climate in the Community Atmosphere Model, version 5". In: *J. Adv. Model. Earth Syst* 6, pp. 357–383.

— (2014b). "On the simulation of the quasi-biennial oscillation in the Community Atmosphere Model". In: *J. Geophys. Res. Atmos* 119, pp. 3045–3062.

Sadourny, R. (1972). "Conservative finite-difference approximations of the primitive equations on quasi-uniform spherical grids". In: *Monthly Weather Review* 100, pp. 136–144.

Sandu, I., P. Bechtold, A. Beljaars, et al. (2016). "Impacts of parameterized orographic drag on the Northern Hemisphere winter circulation". In: *J. Adv. Model. Earth Syst* 8, pp. 196–211.

Sandu, I. et al. (2019). "Impacts of orography on large-scale atmospheric circulation". In: *npj Climate and Atmospheric Science* 10.

Scaife, A. A. et al. (2010). "Atmospheric Blocking and Mean Biases in Climate Models". In: *Journal of Climate* 23, pp. 6143–6152.

Scaife, A. A. et al. (2011). "Improved Atlantic winter blocking in a climate model". In: *Geophysical Research Letters* 38, p. L23703.

Schiemann, R. et al. (2020). "Northern Hemisphere blocking simulation in current climate models: evaluating progress from the Climate Model Intercomparison Project Phase 5 to 6 and sensitivity to resolution". In: *Weather Clim. Dynam.* 1, pp. 277–292.

Scinocca, J. F. and N. A. McFarlane (2000). "The parametrization of drag induced by stratified flow over anisotropic orography". In: *Q. J. R. M. S.* 126, pp. 2353–2393.

Scinocca, J. F. and B. R. Sutherland (2010). "Self-Acceleration in the Parameterization of Orographic Gravity Wave Drag". In: *Journal of the Atmospheric Sciences* 67, pp. 2537–2546.

Simmons, A. J. and R. Strüfing (1981). *An energy and angular-momentum conserving finite-difference scheme, hybrid coordinates and medium-range weather prediction*. Technical Report ECMWF Report No. 28. European Centre for Medium–Range Weather Forecasts, Reading, U.K.

Smith, R.B. (1979). "The Influence of Mountains on the Atmosphere". In: *Advances in Geophysics* 21, pp. 87–230.

Stein, J. (1992). "Investigation of the regime diagram of hydrostatic flow over a mountain with a primitive equation model. Part I: Two-dimensional flows". In: *Q. J. R. Meteorol. Soc* 118, pp. 1057–1081.

Strommen, K. et al. (2012). "The Sensitivity of Euro-Atlantic Regimes to Model Horizontal Resolution". In: *Geophysical Research Letters* 46, 7810– 7818.

Swinbank, R. (1985). "The global atmospheric angular momentum balance inferred from analyses made during the FGGE". In: *Q. J. R. M. S.* 111, pp. 977–992.

Tibaldi, S. (1986). "Envelope orography and maintenance of the quasi stationary circulation in the ECMWF global models". In: *Advances in Geophysics* 29, pp. 339–374.

Tibaldi, S. and F. Molteni (1990). "On the operational predictability of blocking". In: *Tellus* 42A, pp. 343–365.

Ulbrich, U., G. C. Leckebusch, and J. G. Pinto (2009). "Extra-tropical cyclones in the present and future climate: a review". In: *Theoretical and Applied Climatology* 96, pp. 117–131.

Vallis, G. K. (2017). *Atmospheric and Oceanic Fluid Dynamics*. Ed. by Cambridge University Press.

Van Niekerk, A., I. Sandu, and S. B. Vosper (2018). "The Circulation Response to Resolved Versus Parametrized Orographic Drag Over Complex Mountain Terrains". In: *Journal of Advances in Modeling Earth Systems* 10, pp. 2527–2547.

Van Niekerk, A., J. F. Scinocca, and T. G. Shepherd (2017). "The Modulation of Stationary Waves, and Their Response to Climate Change, by Parameterized Orographic Drag". In: *J. Atmos. Sci.* 74, pp. 2557–2574.

Van Niekerk, A. and S. Vosper (2021). "Towards a more "scale-aware" orographic gravity wave drag parametrization: Description and initial testing". In: *Q. J. R. Meteorol. Soc.* 147, pp. 3243–3262.

Van Niekerk, A. et al. (2020). "COnstraining ORographic Drag Effects (COORDE): A Model Comparison of Resolved and Parametrized Orographic Drag". In: *Journal of Advances in Modeling Earth Systems* 12, e2020MS002160.

Vial, J. and T. J. Osborn (2012). "Assessment of atmosphere-ocean general circulation model simulations of winter northern hemisphere atmospheric blocking". In: *Climate Dynamics* 39, pp. 95–112.

Vosper, S. B., A. R. Brown, and S. Webster (2016). "Orographic drag on islands in the NWP mountain grey zone". In: *Q.J.R. Meteorol. Soc.* 142, pp. 3128–3137.

Vosper, S. B. et al. (2020). "What can we learn about orographic drag parametrisation from high-resolution models? A case study over the Rocky Mountains". In: *Q. J. R. Meteorol. Soc.* 146, pp. 979–995.

Wallace, J. M., G. H. Lim, and M. L. Blackmon (1988). "Relationship between Cyclone Tracks, Anticyclone Tracks and Baroclinic Waveguides". In: *Journal of the Atmospheric Sciences* 45, pp. 439–462.

Wallace, J. M., S. Tibaldi, and A. J. Simmons (1983). "Reduction of systematic forecast errors in the ECMWF model through the introduction of an envelope orography". In: *Q. J. R. M. S* 109, pp. 683–717.

Williams, K. D. et al. (2020). "Addressing the causes of large-scale circulation error in the Met Office Unified Model". In: *Q. J. R. M. S.* 146, pp. 2597–2613.

Wood, N., A. R. Brown, and F. E. Hewer (2001). "Parametrizing the effects of orography on the boundary layer, an alternative to effective roughness lengths". In: *Q. J. R. Meteorol. Soc.* 127, pp. 759–778.

Wood, N. and P. J. Mason (1993). "The pressure force induced by neutral, turbulent flow over low hills". In: *Q. J. R. Meteorol. Soc* 119, pp. 1233–1267.

Woollings, T., D. Barriopedro, J. Methven, et al. (2018). "Blocking and its response to climate change". In: *Current Climate Change Reports* 4, pp. 287–300.

Woollings, T., A. Hannachi, and B. Hoskins (2010). "Variability of the North Atlantic eddy-driven jet stream". In: *Q. J. R. M. S.* 136, pp. 856–868.

Woollings, T. et al. (2009). "Storm track sensitivity to sea surface temperature resolution in a regional atmosphere model". In: *Climate Dynamics* 35, 341–353.

Woollings, T. et al. (2010). "Associations between stratospheric variability and tropospheric blocking". In: *J. Geophys. Res.* 115, p. D06108.

Wu, Z. and T. Reichler (2020). "Variations in the Frequency of Stratospheric Sudden Warmings in CMIP5 and CMIP6 and Possible Causes". In: *Journal of Climate* 33, pp. 10305–10320.

Xu, D. and P. A. Taylor (1995). "Boundary-layer parametrization of drag over small-scale topography". In: *Q. J. R. M . S.* 121, pp. 433–443.

Zadra, A. (2013). *WGNE Drag Project – An inter-model comparison of surface stresses – Report no. 1*. URL: https://collaboration.cmc.ec.gc.ca/science/rpn/drag_project/documents/wgne_drag_project_report01.pdf.

Zadra, A. et al. (2003). "The subgrid-scale orographic blocking parametrization of the GEM Model". In: *Atmosphere-Ocean* 41:2, pp. 155–170.

Zappa, G., L. C. Shaffrey, and K.I. Hodges (2013). "The Ability of CMIP5 Models to Simulate North Atlantic Extratropical Cyclones". In: *Journal of Climate* 26, pp. 5379–5396.

Zappa, G. et al. (2013). "Linking Northern Hemisphere blocking and storm track biases in the CMIP5 climate models". In: *Geophysical Research Letters* 41, pp. 135–139.

Zhang, G. J. and N. A. McFarlane (1995). "Role of convective scale momentum transport in climate simulation". In: *J. Geophys. Res.* 100, pp. 1417–1426.

Università
Ca'Foscari
Venezia

DEPOSITO ELETTRONICO DELLA TESI DI DOTTORATO

DICHIARAZIONE SOSTITUTIVA DELL'ATTO DI NOTORIETA'

(Art. 47 D.P.R. 445 del 28/12/2000 e relative modifiche)

Io sottoscritto ..... GUIDO DAVOLI .....

nat.. a ..... REGGIO EMILIA ..... (prov. RE) il ..... 05/10/1992 .....

residente a MONTECCHIO EMILIA in ..... VIA GARIBALDI ..... n. 10.

Matricola (se posseduta) ... 956386 ..... Autore della tesi di dottorato dal titolo:

..... IMPACTS OF THE REPRESENTATION OF OROGRAPHIC DRAG .....

..... ON THE CLIMATE OF AN ATMOSPHERIC MODEL .....

.....

Dottorato di ricerca in ..... SCIENZA E GESTIONE DEI CAMBIAMENTI CLIMATICI

(in cotutela con ..... / .....)

Ciclo ..... XXXIII .....

Anno di conseguimento del titolo ..... 2022 .....

DICHIARO

di essere a conoscenza:

1) del fatto che in caso di dichiarazioni mendaci, oltre alle sanzioni previste dal codice penale e dalle Leggi speciali per l'ipotesi di falsità in atti ed uso di atti falsi, decado fin dall'inizio e senza necessità di nessuna formalità dai benefici conseguenti al provvedimento emanato sulla base di tali dichiarazioni;

2) dell'obbligo per l'Università di provvedere, per via telematica, al deposito di legge delle tesi di dottorato presso le Biblioteche Nazionali Centrali di Roma e di Firenze al fine di assicurarne la conservazione e la consultabilità da parte di terzi;

3) che l'Università si riserva i diritti di riproduzione per scopi didattici, con citazione della fonte;

4) del fatto che il testo integrale della tesi di dottorato di cui alla presente dichiarazione viene archiviato e reso consultabile via internet attraverso l'Archivio Istituzionale ad Accesso Aperto dell'Università Ca' Foscari, oltre che attraverso i cataloghi delle Biblioteche Nazionali Centrali di Roma e Firenze;

5) del fatto che, ai sensi e per gli effetti di cui al D.Lgs. n. 196/2003, i dati personali raccolti saranno trattati, anche con strumenti informatici, esclusivamente nell'ambito del procedimento per il quale la presentazione viene resa;

6) del fatto che la copia della tesi in formato elettronico depositato nell'Archivio Istituzionale ad Accesso Aperto è del tutto corrispondente alla tesi in formato cartaceo, controfirmata dal tutor, consegnata presso la segreteria didattica del dipartimento di riferimento del corso di dottorato ai fini del deposito presso l'Archivio di Ateneo, e che di conseguenza va esclusa qualsiasi responsabilità dell'Ateneo stesso per quanto riguarda eventuali errori, imprecisioni o omissioni nei contenuti della tesi;

7) del fatto che la copia consegnata in formato cartaceo, controfirmata dal tutor, depositata nell'Archivio di Ateneo, è l'unica alla quale farà riferimento l'Università per rilasciare, a richiesta, la dichiarazione di conformità di eventuali copie.

Data 13/12/2021 **Firma** Guido Davoli

Estratto per riassunto della tesi di dottorato

L'estratto (max. 1000 battute) deve essere redatto sia in lingua italiana che in lingua inglese e nella lingua straniera eventualmente indicata dal Collegio dei docenti.

L'estratto va firmato e rilegato come ultimo foglio della tesi.

Studente: Guido Davoli matricola: 956386

Dottorato: Scienza e Gestione dei Cambiamenti Climatici

Ciclo: XXXIII

Titolo della tesi[1] : Impacts of the representation of orographic drag on the climate of an atmospheric model

Abstract:

Molti moderni modelli climatici mostrano errori sistematici, ben noti e persistenti, nel rappresentare la circolazione atmosferica alle medie latitudini dell'emisfero nord. In particolare, i modelli tipicamente sottostimano la frequenza di blocco, hanno problemi nel rappresentare le proprietà osservate delle storm tracks e simulano una circolazione atmosferica eccessivamente zonale, in particolare sui settori Europeo e Nord Atlantico. Fin dalla loro introduzione nei modelli climatici, è noto che le parametrizzazioni del drag orografico hanno un ruolo fondamentale nel migliorare la simulazione della circolazione alle medie latitudini. Tuttavia, esse sono tutt'ora considerate una potenziale sorgente di errore, a causa della incertezza che affligge alcuni parametri fisici.

In questo lavoro sono stati studiati gli effetti di una nuova versione delle parametrizzazioni del form drag e del gravity-wave drag orografici nel modello Community Atmosphere Model. Sono state realizzate una serie di simulazioni per studiarne gli impatti, la loro interazione e per testare la risposta del modello alla variazione di due parametri fisici fondamentali, i cui valori sono soggetti ad incertezza. I risultati evidenziano che le due nuove parametrizzazioni migliorano la simulazione della frequenza di blocco, della struttura delle storm tracks e degli eventi estremi di temperatura sull'Europa, e che i loro effetti benefici sono modulati dai valori precisi dei parametri. Questi risultati evidenziano il ruolo chiave delle parametrizzazioni orografiche nel migliorare l'accuratezza dei modelli climatici, ma anche la necessità di una migliore caratterizzazione e di una rappresentazione unificata dei processi orografici nei modelli climatici futuri.

Many current state-of-the-art climate models show well-known and long-standing biases in representing the atmospheric circulation of Northern Hemisphere midlatitudes. In particular, models typically underestimate atmospheric blocking frequency, have problems in representing the observed properties of the storm tracks and simulate an excessively zonal atmospheric circulation, in particular over the European and North Atlantic sectors. Since their introduction in numerical models, it is known that orographic drag parameterizations play a key role in improving midlatitude circulation. However, they are still considered a potential source of errors, due to the uncertainties which affect some poorly constrained physical parameters.

In this work, I studied the effects of a new version of the parameterizations of both orographic form drag and gravity-wave drag in the NCAR Community Atmosphere Model. I designed a set of experiments to study their impacts, their interactions, and to test the model response to adjustments of two fundamentals, but unconstrained, parameters of the schemes. I have found that the two parameterizations improve the representation of blocking frequency, storm tracks structure, cold and heat waves over Europe, and their beneficial effects are modulated by the precise values of the parameters. These findings underline the importance of orographic parameterizations to improve climate models adequacy to represent reality, but also the need for a better characterization and for a unified representation of drag processes in future climate models.

Firma dello studente

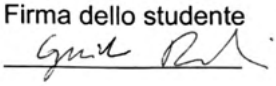

1 Il titolo deve essere quello definitivo, uguale a quello che risulta stampato sulla copertina dell'elaborato consegnato.